NRA8-21 Cycle 2
RBCC Turbopump Risk Reduction

Final Report

Contract No. NAS8-01040

Approved

Thomas V. Ferguson
Morgan Williams
Bogdan Marcu

Task 3a: Validation of impeller analysis procedure for throttled and non-throttled conditions

This section of the final report covers Task 3a of the NRA8-21 cycle 2 RBCC Turbopump Risk Reduction contract.

The primary objective of Task 3a was to use the CFD code INS3D from NASA-Ames to generate both on- and off-design predictions for the consortium optimized impeller flowfield. In addition, a second candidate pump stage was to have been chosen and the same code applied to calculate its flowfield.

Geometry configuration for the CFD Analysis

The geometry agreed upon for the CFD analysis consists of an impeller diffuser configuration, specifically, the CFD Consortium Optimized Impeller (COI) and the 13 island-vanes radial diffuser (13IVD). The tested configuration included also the ADP inducer installed upstream of the COI, however, the inducer has not been included in the analysis. Instead, flow conditions downstream of the inducer at the COI inlet have been provided for boundary condition formulation.

Computational grids have been generated for the specified configuration. The grids, in plot3d format, have been ported to Rocketdyne and inspected for geometric accuracy. A 2.1° angle correction was identified and corrected in the arrangement of the island-vanes. The grid geometry cut a mid-span plane as shown in figure 1.

The grid is comprised of 35 zones with a total of 23 million grid points modeling the full circumference geometry of 6 long and 6 short impeller blades and 13 diffuser vanes.

Flow regime

The available test database with detailed flow measurements includes three flow regimes:

1) Design Flow,   100% Q/N, at 1210 GPM flow rate and 6322 RPM
2) Off-design Flow   88% Q/N, at 1065 GPM flow rate and 6322 RPM
3) Off-design Flow   120% Q/N, at 1452 GPM flow rate and 6322 RPM

Inlet boundary conditions have been provided for each flow at the cross-sectional plane located at 1.167 inch upstream of the impeller leading edge, as shown in figure 2.

Numerical Procedure

Numerical method

The present computations are performed utilizing the INS3D computer code, which solves the incompressible Navier-Stokes equations for both steady-state and unsteady flows. The numerical solution of the incompressible Navier-Stokes equations requires special attention in order to satisfy the divergence-free constraint on the velocity field because the incompressible formulation does not yield the pressure field explicitly from the equation of state or through the continuity equation.

One way to avoid the numerical difficulty originated by the elliptic nature of the problem is to use an artificial compressibility method. The artificial compressibility algorithm, which introduces a time-derivative of the pressure term into the continuity equation, transforms the elliptic-parabolic type partial differential equations into the hyperbolic-parabolic type. An incompressible flow solver, INS3D, has been developed based on this algorithm. Since the convective terms of the resulting equations are hyperbolic, upwind differencing can be applied to these terms. The current version uses Roe's flux-difference splitting. The third and fifth-order upwind differencing used here are implementations of a class of high-accuracy flux-differencing schemes for the compressible flow equations.

To obtain time-accurate solutions, the equations are iterated to convergence in pseudo-time for each physical time step until the divergence of the velocity field has been reduced below a specified tolerance value. The total number of sub-iterations required varies depending on the problem, time step size and the artificial compressibility parameter used, and typically ranges from 10 to 30 sub-iterations. The matrix equation is solved iteratively by using a non-factored Gauss-Seidel type line-relaxation scheme, which maintains stability and allows a large pseudo-time step to be taken. The GMRES scheme has also been utilized for the solution of the resulting matrix equation.

Computer memory requirement for the flow solver INS3D with line-relaxation is 35 times the number of grid points in words, and with GMRES-ILU(0) scheme is 220 times the number of grid points in words. When a fast converging scheme, such as a GMRES-ILU(0) solver, was implemented into the artificial compressibility method, reasonable agreement was obtained between computed results and experimental data.

Turbopump scripts

For each component of a turbopump (inlet guide vanes, impeller and diffuser), a script was developed to accelerate the simulation process prior to the flow solver call. The starting point is the geometry definition of a component which consists of the hub and shroud profile curves and the surface panels of each

distinct blade. Functions provided by the script include overset surface and volume grid generation, creation of object X-ray maps for hole-cutting, and creation of overset domain connectivity inputs. After running the domain connectivity program OVERFLOW-D/DCF with the script-created input file, the resulting grids and iblank connectivity information are used as input for the INS3D flow solver. Figure 3 illustrates the procedures automatically handled by the scripts.

Important attributes of each component are parameterized in the scripts. For example, parameterized geometric attributes include the number of blades for the inlet guide vanes and the diffuser; and the number of distinct blades per section and the number of sections for the impeller. Parameterized grid attributes include hub and shroud surface grid spacings, leading and trailing edge spacings, viscous wall spacing for the volume grids, stretching ratios and marching distances for the hyperbolic surface and volume grids. All parameters are controlled via an input file and the script can be rapidly re-run to generate different configurations. For example, the user can input different geometry definitions for the hub, shroud and blades, and try different number of blades and grid resolutions.

A high level scripting language Tcl is utilized which provides modularity as well as floating point arithmetic capability (unlike basic shell languages such as C-shell). Although extra time and expertise are needed to construct the scripts, the pay-off is well worth the effort. The advantages include the ability to rapidly re-run the entire process in just a few minutes versus one or more days of manual effort. Tedious repetitive error-prone inputs are avoided with the scripts while they also provide a documentation of the entire grid generation procedure. Grid refinement and parameter studies can also be easily and efficiently performed.

Table 1 shows a comparison of the process time from geometry definition to domain connectivity inputs for the various turbopump components. Significant time savings is accomplished for generating a large number of different parameter studies as is frequently practiced in a design environment.

Parallel computations

Parallel computing strategies vary depending on computer architecture such as memory arrangement relative to processing units. Two approaches have been implemented in the present study: the first approach is hybrid MPI/OpenMP and the second one is Multi-Level Parallelism (MLP) developed at NASA-Ames Research Center.

The first approach is obtained by using message-passing interface (MPI) for inter-zone parallelism, and by using OpenMP directives for intra-zone parallelism. INS3D-MPI is based on the explicit message-passing interface across MPI

3

groups and is designed for coarse grain parallelism. The primary strategy is to distribute the zones across a set of processors. During the iteration, all the processors would exchange boundary condition data between processors whose zones shared interfaces with zones on other processors. A simple master-worker architecture was selected because it is relatively simple to implement and it is a common architecture for parallel CFD applications. All I/O was performed by the master MPI process and data was distributed to the workers. After the initialization phase is complete, the program begins its main iteration loop. Figure 4 shows the MPI/OpenMP scalability for the impeller computations using 19.2 Million grid points.

The second approach in Multi-Level Parallelism (MLP) is obtained by using NAS-MLP routines. The shared memory MLP technique developed at NASA Ames Research Center has been incorporated into the INS3D code. This approach differs from the MPI/OpenMP approach in a fundamental way in that it does not use messaging at all. All data communication at the coarsest and finest level is accomplished via direct memory referencing instructions. This approach also provides a simpler mechanism for converting legacy code, such as INS3D, than MPI.

For shared memory MLP, the coarsest level parallelism is supplied by spawning off independent processes via the standard UNIX fork. The advantage of the UNIX fork over MPI procedure is that the user does not have to change the initialization section of the large production code. A library of routines is used to initiate forks, to establish shared memory arenas, and to provide synchronization primitives.

The shared memory organization for INS3D is shown in Figure 5. The boundary data for the overset grid system is archived in the shared memory arena by each process. Other processes access the data from the arena as needed. Figure 6 shows the MLP scalability for the impeller computations using 19.2 Million grid points.

Using the INS3D-MLP parallel implementation, time-accurate computations for the wide-range configuration have been carried out on SGI Origin platforms.

Results

The calculations for the three flow regimes have been started in sequence in order to minimize computational time. The 100% Q/N case has been started first, then, after advancing the solution for about three impeller full rotations, the flow field achieved numerically has been used as initial condition for the 88% Q/N case, and 120% Q/N case.

The simulations are run using 96 CPU's on an Origin 3000 platform at NASA Ames Research Supercomputer Center.
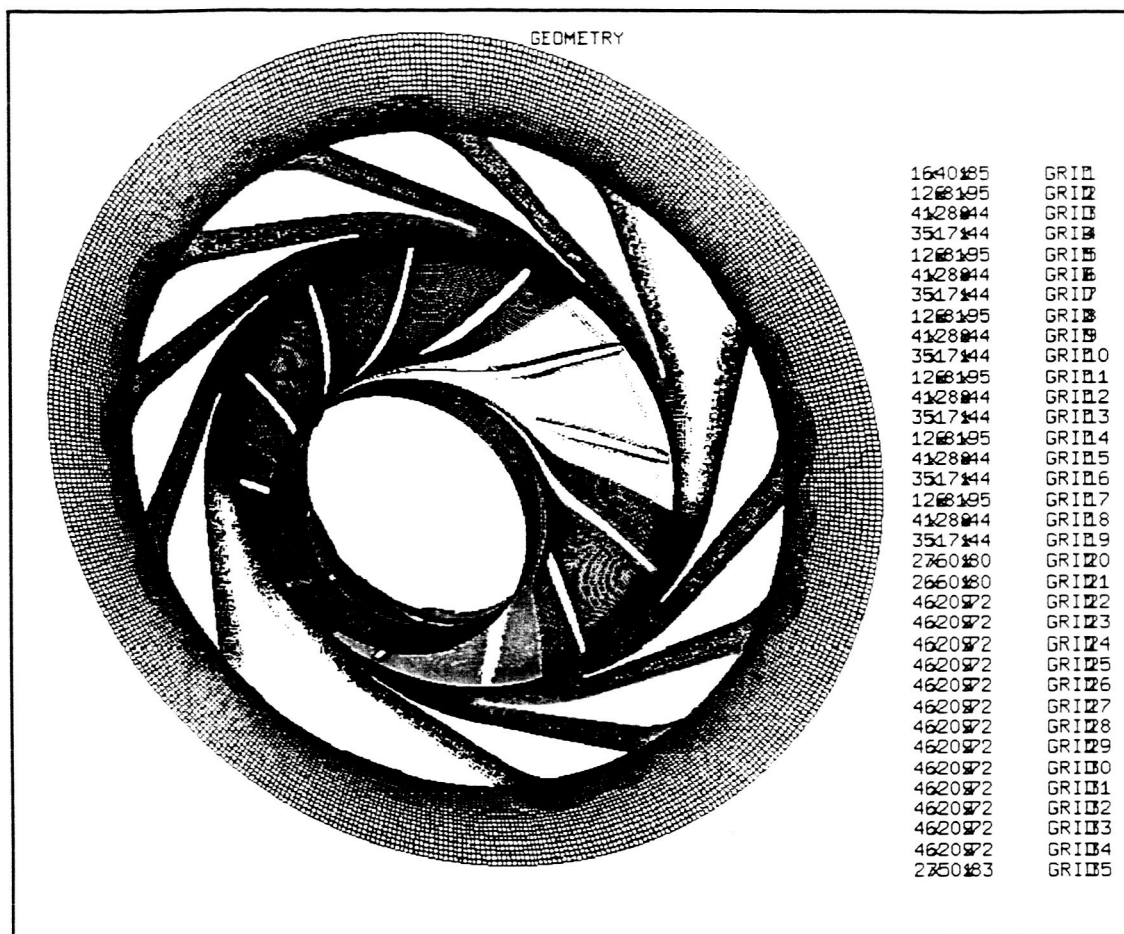
The 100% Q/N flow regime has been finalized after 6 full impeller rotations. At the time of writing this report, the 88% Q/N and 120% Q/N cases are in the process of finalization.

Special attention has been given to the post-processing effort. During the work performed on this task, optimal ways to retrieve relevant results from the large amount of data produced have been searched.

As a direct comparison with water test data, and excellent match of the radial and tangential velocity profiles has been obtained at the impeller exit, as displayed in figure 7 and 8.

The qualitative aspects of the flow field have been addressed in five flow visualization movies made for the 100% Q/N flow regime. Four of these visualizations address the impeller inlet and the energetic qualitative nature of the back flow phenomenon. The visualizations show that the vorticity at impeller inlet and the amount of fluid circulation has a significant unsteady nature, at time scales that are faster than the impeller through flow: the unsteady vortex formation at the inlet due to back flow has a turnaround period shorter than the impeller through-flow time. The fifth visualization addresses the region at the impeller exit and diffuser inlet.

The flow displays a separation region at the vane leading edge associated with a slower flow in the channel downstream behind it. The simulation also shows that the secondary flows such as the backflow from the diffuser back into the impeller at the hub and shroud walls are associated with flow velocities significantly larger than the main flow, and frequencies that are shorter. The effect of these phenomena on the structure of the pump require further detailed investigation. Similar visualizations will be made for the off design cases.
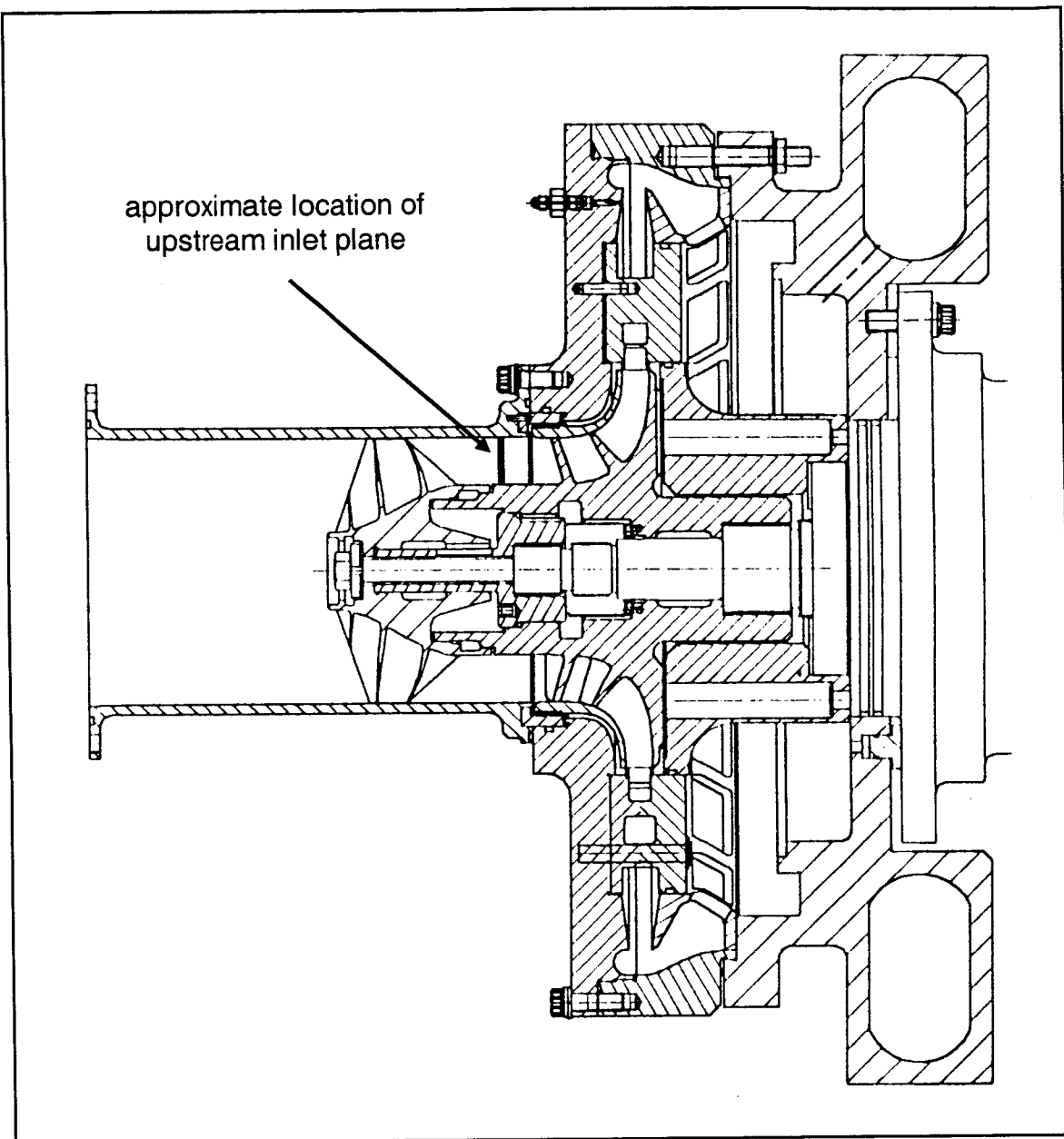
GEOMETRY

1640185	GRID 1
128195	GRID 2
41288444	GRID 3
3517144	GRID 4
1288195	GRID 5
41288444	GRID 6
3517144	GRID 7
1288195	GRID 8
41288444	GRID 9
3517144	GRID 10
1288195	GRID 11
41288444	GRID 12
3517144	GRID 13
1288195	GRID 14
41288444	GRID 15
3517144	GRID 16
1288195	GRID 17
41288444	GRID 18
3517144	GRID 19
2760180	GRID 20
2660180	GRID 21
4620972	GRID 22
4620972	GRID 23
4620972	GRID 24
4620972	GRID 25
4620972	GRID 26
4620972	GRID 27
4620972	GRID 28
4620972	GRID 29
4620972	GRID 30
4620972	GRID 31
4620972	GRID 32
4620972	GRID 33
4620972	GRID 34
2750183	GRID 35

Figure 1. The impeller plus diffuser grid geometry.

approximate location of
upstream inlet plane

Figure 2. Test configuration used for the CFD analysis and the inlet plane for the flow boundary conditions.

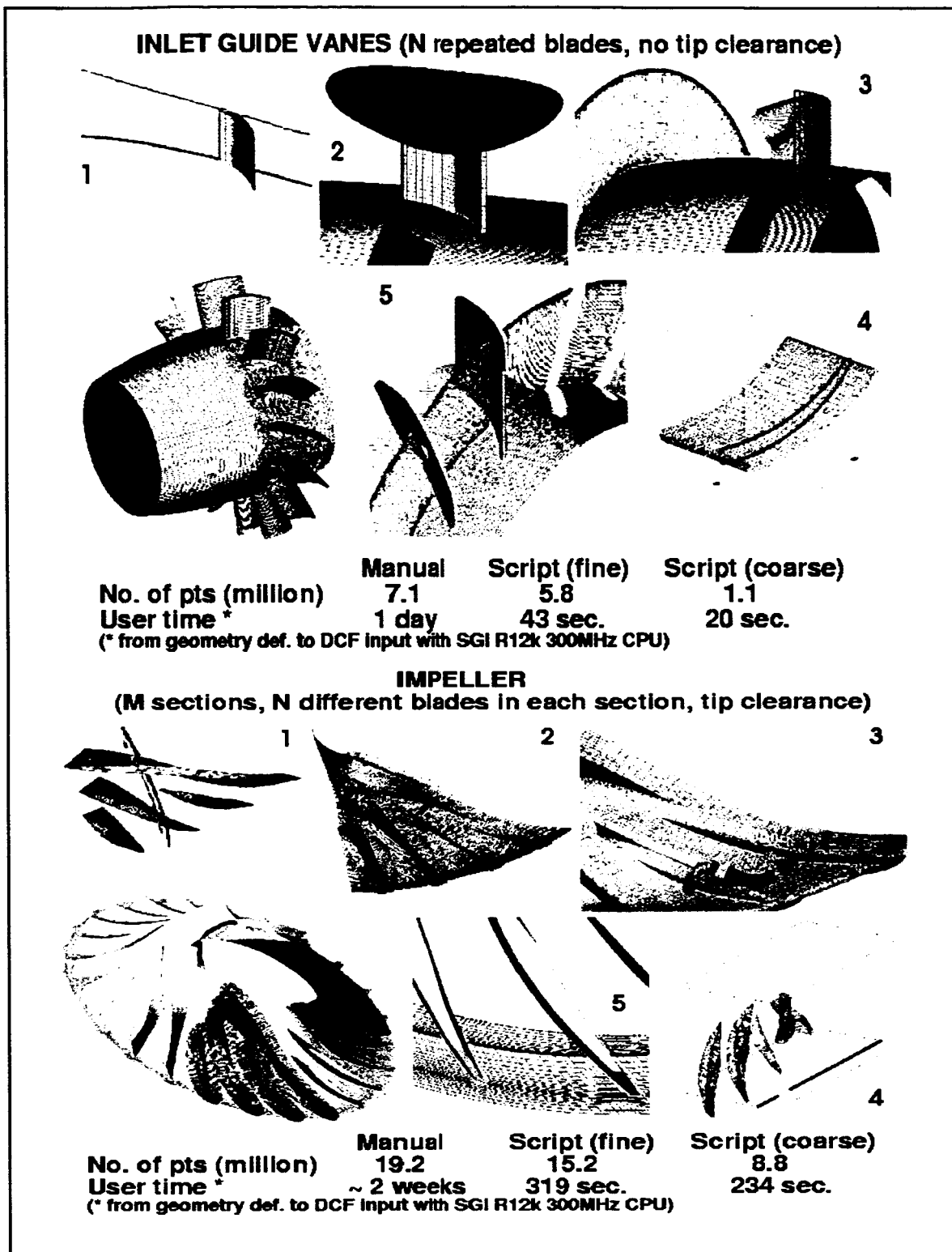**INLET GUIDE VANES (N repeated blades, no tip clearance)**

	Manual	Script (fine)	Script (coarse)
No. of pts (million)	7.1	5.8	1.1
User time *	1 day	43 sec.	20 sec.

(* from geometry def. to DCF input with SGI R12k 300MHz CPU)

IMPELLER
(M sections, N different blades in each section, tip clearance)

	Manual	Script (fine)	Script (coarse)
No. of pts (million)	19.2	15.2	8.8
User time *	~ 2 weeks	319 sec.	234 sec.

(* from geometry def. to DCF input with SGI R12k 300MHz CPU)

Figure 3. Illustration of turbopump scripts for inlet guide vanes and impeller sections.

Inlet Guide Vanes (fine) Script (coarse)	Manual	Script
No. of points (millions) 1.1	7.1	5.8
User time sec. 20 sec.	1 day	43

Impeller (fine) Script (coarse)	Manual	Script
No. of points (millions) 8.8	19.2	15.2
User time sec. 234 sec.	2 weeks	319

Diffuser (fine) Script (coarse)	Manual	Script
No. of points (millions) 1.6	8.0	6.4
User time sec. 22 sec.	1 day	37

Table 1. Comparison of process time from geometry definition to domain connectivity inputs. User time for the manual process is the total wall clock time for working through the different parts of the process. User time for the scripts is the wall clock time to run the scripts on an R12000 300MHz Silicon Graphics workstation.
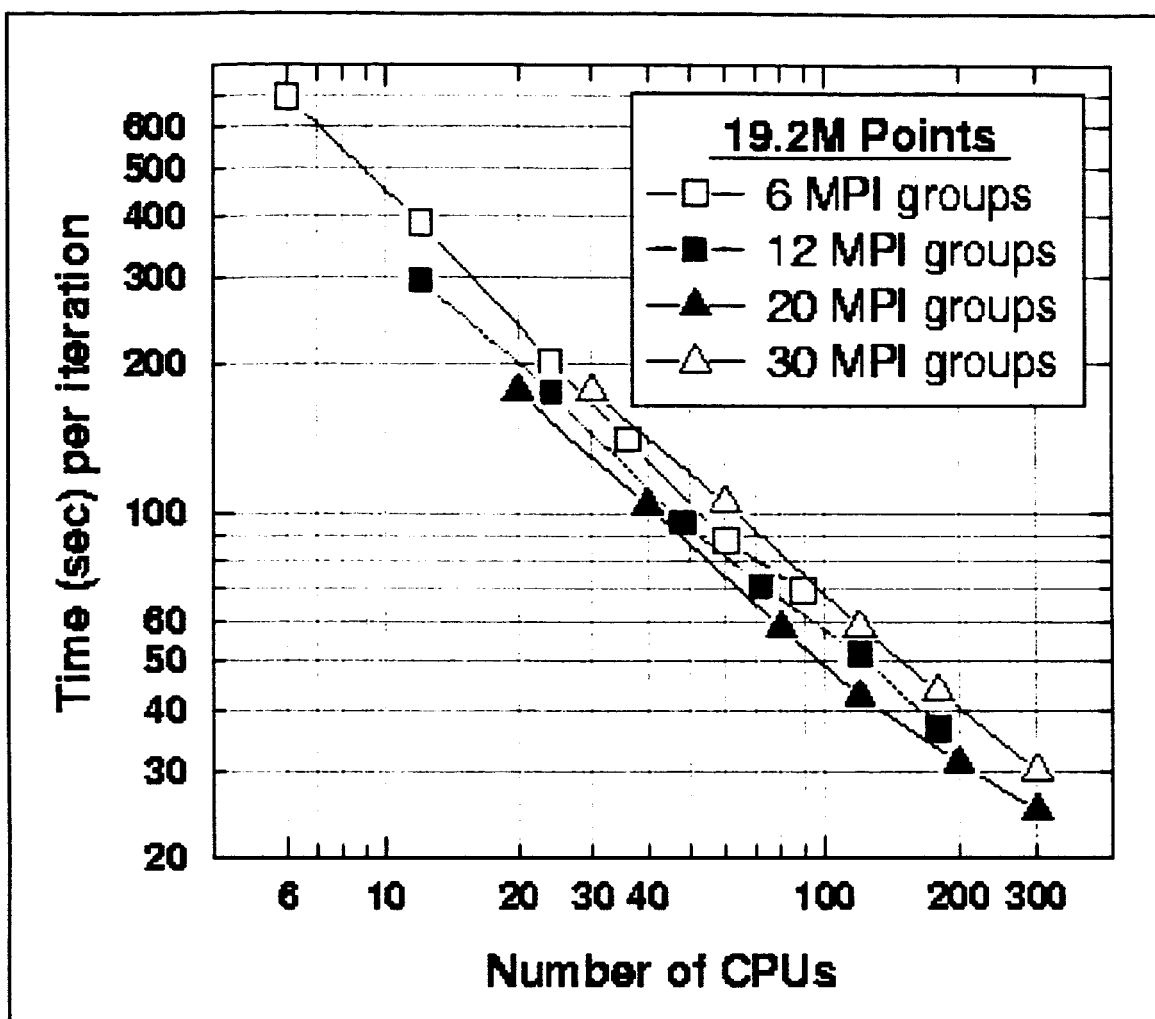
Figure 4. INS3D-MPI/OpenMP performance versus CPU counts on SGI Origin platform.
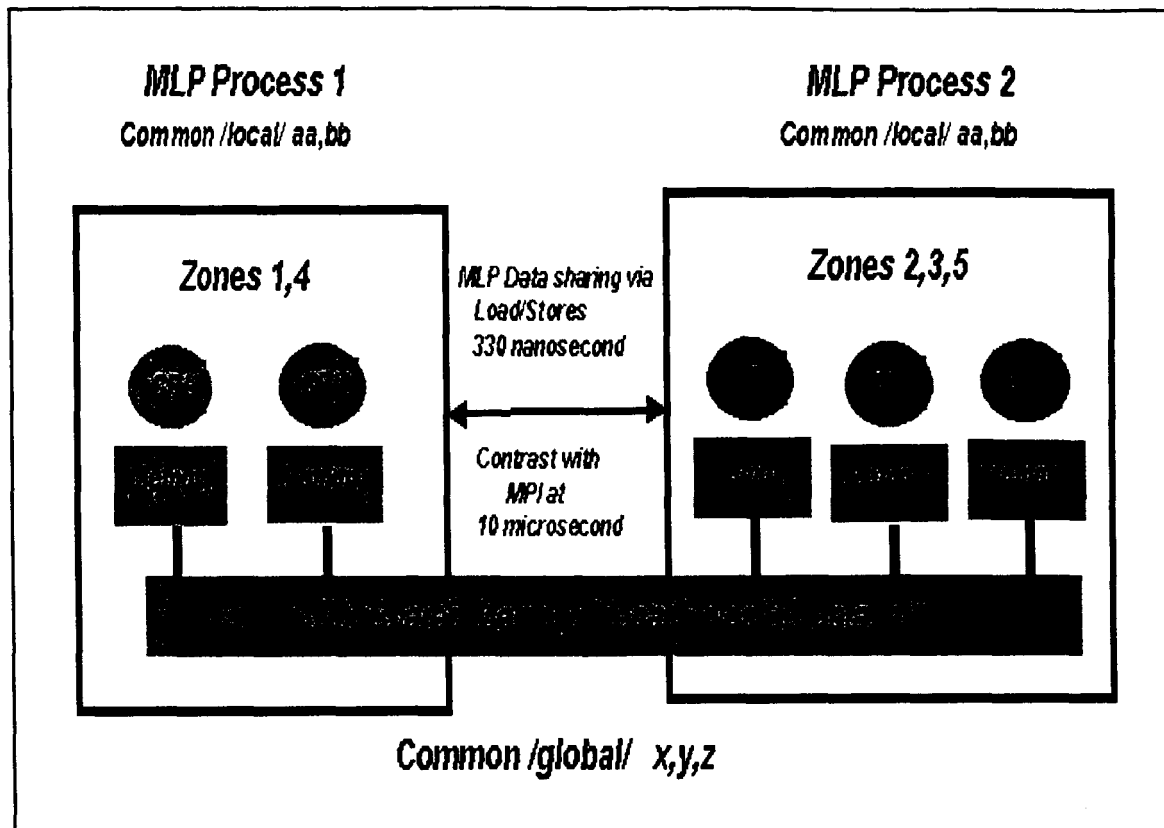
Figure 5. Shared memory MLP organization for INS3D-MLP.
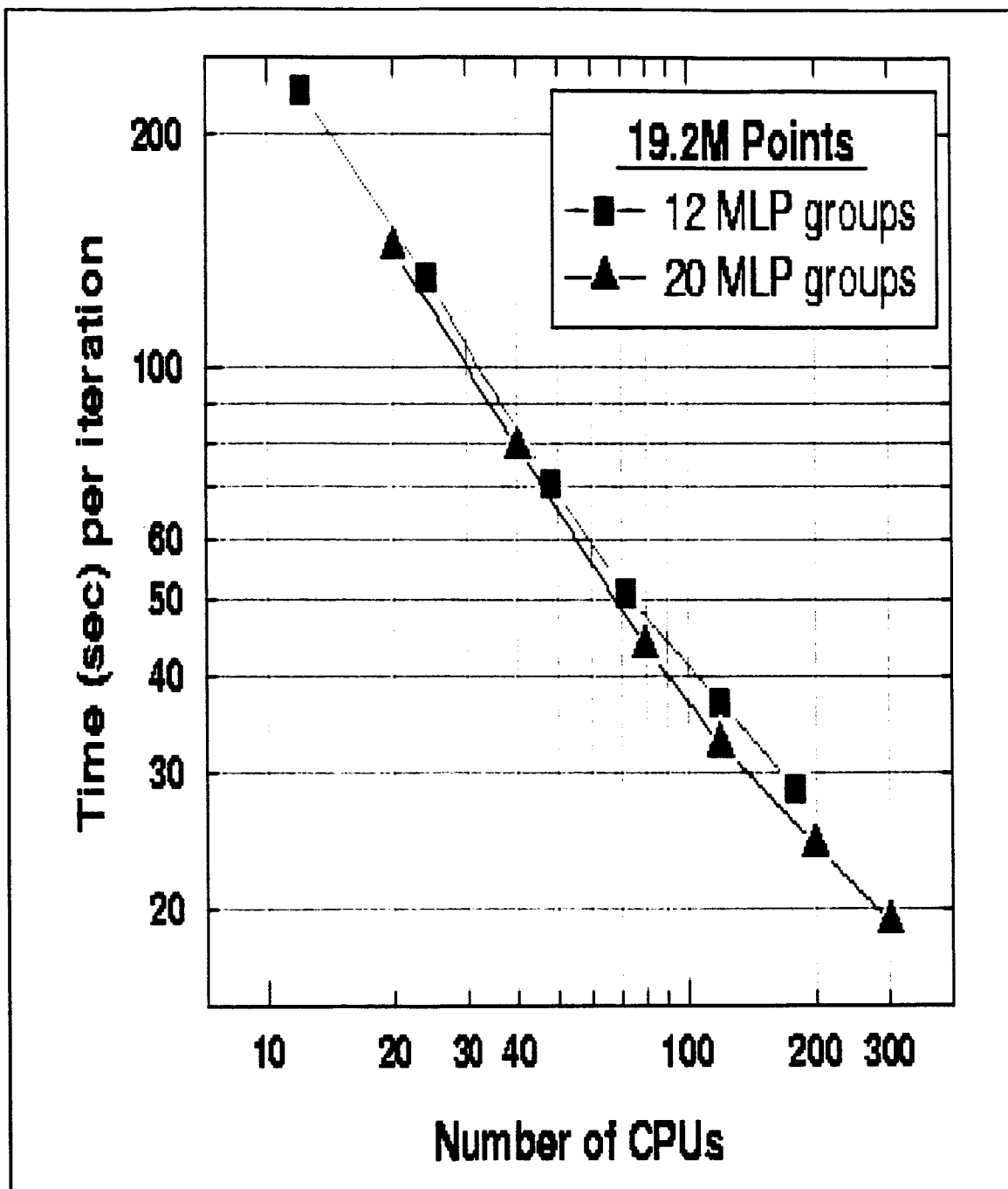
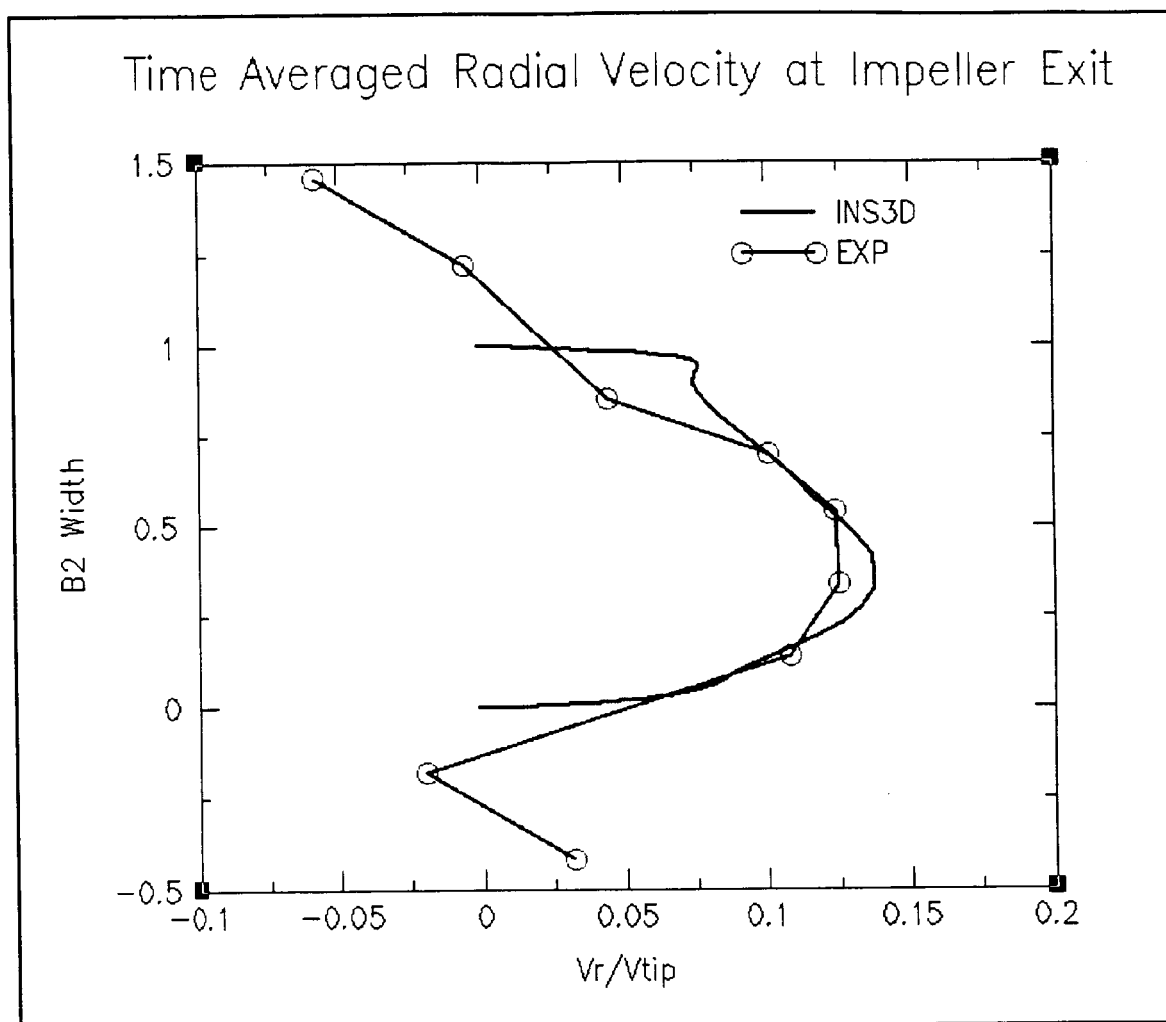Figure 6. Time (sec) per iteration for the impeller computations using INS3D-MLP on SGI Origin platforms.

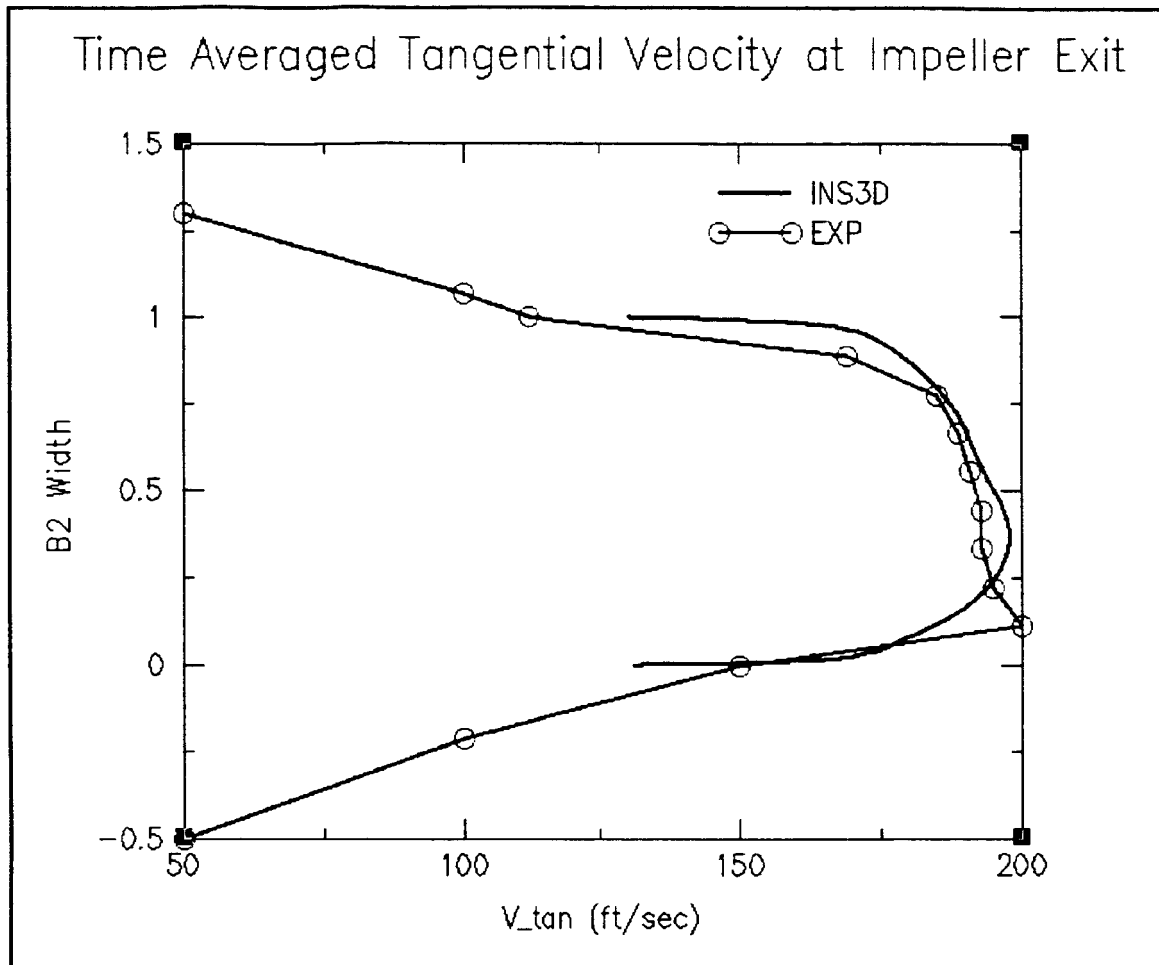Figure 7. Time averaged radial velocity at impeller exit.

Figure 8. Time averaged tangential velocity at impeller exit.

Task 4a: Development of CFD validation package

This section of the final report covers Task 4a of the NRA8-21 Cycle 2 RBCC Turbopump Risk Reduction contract.

The intent of this part of the project was to create a turbomachinery testing database that summarized all of the testing performed over a period of 10+ years on five major turbomachinery components. These components included the SSME High Pressure Fuel Turbopump (HPFTP) impeller; the Advanced Development Pump (ADP) inducer; the consortium baseline impeller (CBI); the consortium optimized impeller (COI) and the 13-vane vane island diffuser (VID). This original data, in the form of personal notes, data reduction printouts, laser velocimeter data, etc. was contained in over 75 notebooks and nearly a dozen reports. The complete organized database was to be a reference source of experimental results. The data could be used to make comparisons with CFD-derived results on the flowfields and overall performance of the same components.

Introduction

Initial efforts on constructing and populating the database began on the SSME impeller setup because it was the first in the long series of components tested. Consequently, it seemed logical to start at the beginning in order to understand the entire sweep of the ensuing tests. Most of the tests shared at least some common hardware, so starting with the first setup also made the most sense in terms of familiarization with the hardware. In addition, the data reduction post-processing scheme shares many common elements throughout the tests. Therefore, it was easiest to start with the original data reduction post-processing methodology before it was adapted to handle the more sophisticated and involved data from later test series.

However, in an effort to boost the timeliness and relevancy of the project goals, efforts on the SSME impeller were put aside to instead turn attention to the CBI. The first component in the CBI tester was the ADP inducer, consequently, the first efforts on the CBI database centered about setting up the ADP inducer database. The inducer flowfield data was composed of 3D laser velocimeter measurements made upstream, downstream and between the blades of the inducer. This was a sensible approach since the output of the inducer provides the input to the impeller, so accurately knowing the inducer flowfield would set up the proper boundary conditions for the impeller CFD calculations. However, after a period of time it was decided to switch focus again and instead concentrate on the CBI itself.

The reasons for this shift were threefold. First, one of the overarching goals of the project was to work on issues of engine throttle-ability over wide flow

ranges. An inducer is not a significant part of the throttle-ability equation, certainly not as much as a diffuser. Secondly, there is a good deal of complexity in setting up the computational grids for the inducer, which would consequently use up a significant amount of time and budget. Lastly, there was a need to quickly show some comparative results between codes, and the codes as developed were best suited to modeling impeller flow fields. Consequently, it was decided to instead concentrate on the CBI itself, and not try to model the inducer flowfield at this time.

To that end, the database construction was shifted again to concentrating on organizing the laser velocimeter flowfield data obtained at the inlet and discharge of the CBI. It was decided the three CFD codes, Enigma, Phantom and INS3D, could use the inlet data as input in order to calculate the discharge flow field which could then be directly compared against each other, as well as against the actual measured discharge flowfield.

After work on the CBI database was nearly complete, efforts were again re-focused onto the COI database along with the VID database. This database is broken into two sub-databases, the first dealing just with the COI discharge velocity and pressure data, as well as the VID velocity data. The second sub-set covers just the VID pressure measurements.

The overall philosophy that guided the construction and layout of the database was the subject of a 2003 JANNAF conference paper. The paper, "Databases for Validation of CFD codes for Off-Design Turbopump Operational Analysis," is available from the JANNAF conference organizers.

Status and expenditures

As the databases now stand, they are in varying states of completeness. A total of 320 hours were initially estimated to be needed to compile, organize and create all of the databases. This was later revised to 472 hours once the work had actually gotten underway in earnest. In contrast, in the May 2000 kickoff meeting for the original broad scope task, a total of 720 hours had been proposed to construct the database incorporating just the diffuser pressure and velocity data. In light of that, the time allocated to construct five databases was far less than sufficient. This is also more transparent when looking at the actual expenditures used to put the databases into their current state.

In the period from January 2003 to July 2003, which is the during the pre-$330K funding from MSFC, approximately 400 hours were spent on the database activities. Individual labor hour breakdowns for this period are not available, so the figure quoted assumes 80% of the total hours charged during this time were for the database construction.

In the period from July 2003 to January 2004, which is when the $330K funds from MSFC were available, 858 hours were spent on the database. Of the $330K in funding, about $67K was removed to cover a cost overrun from the 2000 effort; for a pre-determined fee; and to cover the cost of monitoring the contract. In addition, the average hourly rate at which the contract would be billed increased 14% from the time the statement of work was submitted to the time the funds were received. Funds actually available for engineering use were $263K. Overall, this equated to a decrease of about 400 man-hours in the project hours.

The following sections will address the databases which were constructed for the various components. Each section will provide a description of the worksheet for the relevant workbook for that component. The actual workbooks for all components are attached in electronic format, i.e., as Excel files, in Appendix C.

The SSME HPFTP database

This setup was for the SSME HPFTP impeller coupled with an upstream flow turning inducer, with the impeller followed by an SSME crossover, then a facility volute. Velocimeter data was collected at the inlet and discharge of the impeller. Pressure data was collected on the overall impeller as well as by a Kiel probe traversing radially at the discharge of the impeller. Figure 1 shows a cross sectional view of the tester and the dataplanes.

Right from the beginning it should be noted that because the SSME impeller database was started first, but later set aside to pursue other higher priority components, the structure and form of its existing database differs from that of the other, latter, more complete and standardized databases.
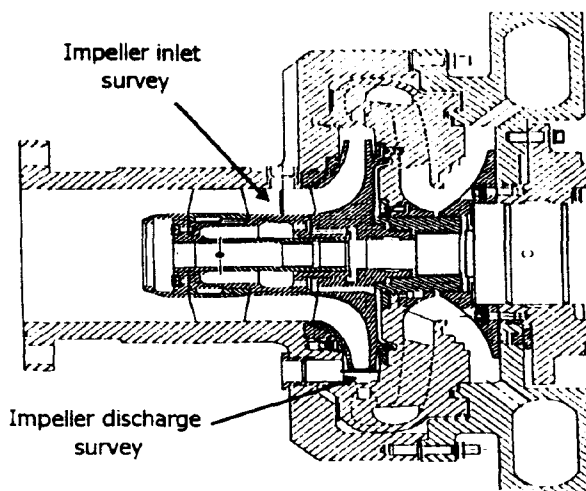
Tester cross section

The purpose of this section is to show an overview of test setup in order to familiarize the user with the test hardware. The sheet contains a single black and white cross-sectional view of the tester setup with the main components identified. The sheet is 100% complete.

Geometry & design info

The purpose of this worksheet is to provide basic hydrodynamic and geometric data on the components that comprise the tester. The table shows hydrodynamic design criteria and dimensions of the inducer, impeller, crossover and volute. The sheet is 90% complete and is missing part numbers and dimensions of the crossover and volute, and a few pieces of data on the inducer.

Figure 1. The SSME HPFTP impeller tester setup and velocimeter dataplane locations.

Measurement matrix

This sheets purpose is to provide a quick glance evaluation of what type of testing was performed, on which component and at which flow rates. The table shows the four major components of the tester, namely the inducer, impeller, crossover and volute, and for each delineates whether static, dynamic or total pressures were measured; whether laser velocimeter data was acquired on that component; and whether pump performance data were collected on a specific component. All of the information is keyed to show whether the data was acquired at design or off-design flow conditions. This sheet is 100% complete.

Acquired data comparison

This sheet is unique to the SSME database and is composed of several summary tables. The first relates information on the number of radial data stations versus flowrates for velocimeter data acquired at the inlet to the impeller. The second table deals with the impeller discharge survey. It shows the number of velocimeter data points within each region of the flow survey at each of the three radial planes at the discharge. It further identifies whether the data taken at

each radial plane was located in the B2 region, near the window or near the wall, with further details about how the multi-windowing was performed. The third table concerns the Kiel probe survey at the impeller discharge and relates the number of radial positions as a function of flowrate. The final table summarizes the velocimeter data in terms of the number of data points as a function of flowrate and location within the pump. This sheet is 100% complete.

L2F measurement matrix

This is a large table filled with details about the velocimeter testing and meant to provide a summary overview of the testing performed. It is organized by component in the tester, such as inducer, impeller, volute, etc. as well as by flowrate. At each of the four tested flowrates, the entry for that component spells out some detail of the data that was collected. For example, for the upstream impeller survey, information is provided on such factors as the number of axial planes; the location of the planes relative to the impeller leading edge; the radial locations (in %) within the flow annulus; the annulus width; whether ensemble averaging was used, etc. Color-coding is used to help group the common entries together. This sheet is 100% complete.

Laser monitoring files impeller inlet

The purpose is to document the actual average flow conditions for the entire tester which were recorded during the laser velocimeter data acquisition segment on the SSME impeller. From the information contained in this large table, the user is free to verify flow conditions during each test or use the data to normalize the velocimeter data to a specific condition, for example to a constant inlet pressure or flowrate. The table uses color-coding to group the information by flowrate.

This table ties together general identification information such as test number, test date, overall test configuration, laser data filename and laser data experiment number with laser data position information. All of this data is then correlated to two types of averaged data, the first being fundamental parameter measurements. These include general test parameters, like flowrate, pump speed, water temperature and torque as well as overall pump pressures recorded at locations such as the pump inlet, impeller inlet, upstream shroud, impeller discharge and pump discharge.

The second type of averaged data were calculated parameters based on measurements of pressures. These data have been corrected for transducer height and orientation relative to the pump centerline and include reference to the PID and MDS numbers from the original data printouts. Included in the calculated parameters listing are general conditions such as flow ratio, inlet water density, vapor head, inlet NPSH, NSS and the impeller inlet flow coefficient. Other calculated parameters include the inducer inlet total pressure, the impeller

inlet static pressure, shroud parameters, the impeller discharge static pressure, the inducer static-to-static headrise and the impeller static-to-static headrise.

The sheet is 20% complete as it is formulated but not populated. The data to be entered do not exist in electronic format, and therefore, has to be manually entered, which is a very time consuming process. The table needs 2,058 entries in total.

Laser monitoring files impeller discharge

This sheet serves a similar purpose as for the impeller inlet monitoring sheet. It is organized in nearly the same fashion, but is much larger due to the fact that the discharge survey was conducted at two or three radial planes, as opposed to one plane at the inlet. Additionally, the discharge data was collected over multiple blade spacings, i.e., downstream of the circumferential spacing from a full blade to a short partial and then to long partial; and then again from long partial to short partial then on to the full blade. The inlet data was collected only from a full to the adjacent full blade.

This sheet is only about 20% complete in that it is formatted but not populated with the actual monitoring data. There are 8,700 pieces of information to be entered and this must be done manually due to a lack of any existing electronic version.

Pressure tap locations

The purpose of this sheet is to provide the user both a graphical overview, as well as the actual physical locations, as to where the various pressure taps were located on the tester housing. A small table was started but no graphics or photos were created or used, and experience with the other databases shows that this type of visual information is essential to imparting an understanding to the user on the location of the pressure taps. This sheet is only 5% complete.

Test number versus laser file number

This sheet is designed to correlate the two file name tagging systems used during data acquisition. The test number refers to the Engineering Development Laboratory's method of naming and delineating test files, while the laser datafile number refers to a bookkeeping reference used by the laser velocimeter. In particular the laser datafile number was used to correlate the data provided in the laser monitoring file printouts (which are the post-processed average tester and facility parameters, like flowrate, torque, inlet pressure, etc.) with the laser file name. This table also serves to provide a double historical reference to the original data files, if there is a need to refer to them again at some point. This sheet is 100% complete.

Laser data impeller inlet

This worksheet has a rudimentary beginning. It contains all of the velocimeter data recorded at the impeller inlet. The data is organized broadly by a section with information on the general test conditions, and concurrently by laser data positional information. The first category includes the test number and date, a short description of the overall test configuration (including such factors as the flowrate, etc.) the laser datafile name, experiment number and time required for acquisition. The second category conveys the laser data station location within the inlet annulus in terms of its percent of the distance from the impeller hub to the tunnel ID.

This information is followed by thirty two columns of velocimeter data. The velocity data in the sixteen windows encompassing the circumferential space from an inducer full blade to the adjacent full blade is given. This is followed by the sixteen windows of flow angle data measured in each of the corresponding velocity windows. The table is color-coded to demarcate the data by flowrate. The normal course of action would be to follow this table with several other tables of data derived from the first. For example, adjustments have to be made for any angular offset between the velocimeter zero angle reference and true vertical, as well as to covert the angle data into a reference frame that is relative to the tangential direction of the impeller blade rotation. Subsequent tables then use the adjusted flow angles in conjunction with the total measured velocity to calculate and present the axial and tangential components of the flow vector. None of these steps were performed however before attention was focused on the other tester components. Consequently, this table is about 20% complete.

Laser data impeller discharge

This sheet fulfills a similar function as the impeller inlet sheet, but for the data collected at the impeller discharge. The laser data positional information is different in that there are three radial planes where the data was collected, rather than just the single axial plane at the impeller inlet. The laser data stations are noted in terms of the percent of the distance across the impeller B2 width. The velocimeter data were not entered into the table, and no subsequent processing was performed to calculate velocity components, etc. This table is about 5% complete.

Concluding remarks

As noted in the start of this section, the SSME database is the most non-complete of the databases. It is also not in the same format, nor contains the same type of information, as the other component databases. In particular, the SSME database is missing sections on continuity calculations which verify the validity of the measured data. It is also missing HQ data on the impeller as well as the abundance of graphics and enhanced photos which enables the user to

more easily understand how, where and why the data was acquired. But unlike the other databases, it offers a rich opportunity for data in light of the fact that it has data collected at both the inlet and discharge over four wide ranging flowrates. Most of the other impeller databases are very limited in flowrate range. Finally, the SSME impeller discharge pressure was mapped extensively using a Kiel probe: twelve flowrates and ten radial positions across the discharge at each flowrate. This kind of information was not collected on the other impellers, making the SSME data unique and valuable.

The CBI database

This setup was for the ADP inducer coupled with the consortium baseline impeller (CBI) which was followed by a vaneless diffuser space, the same SSME HPFTP first stage crossover and then the same facility volute. Data was collected on both the inducer and the impeller flow fields. Figure 2 shows a cross-sectional view of the tester and the locations where data was acquired.
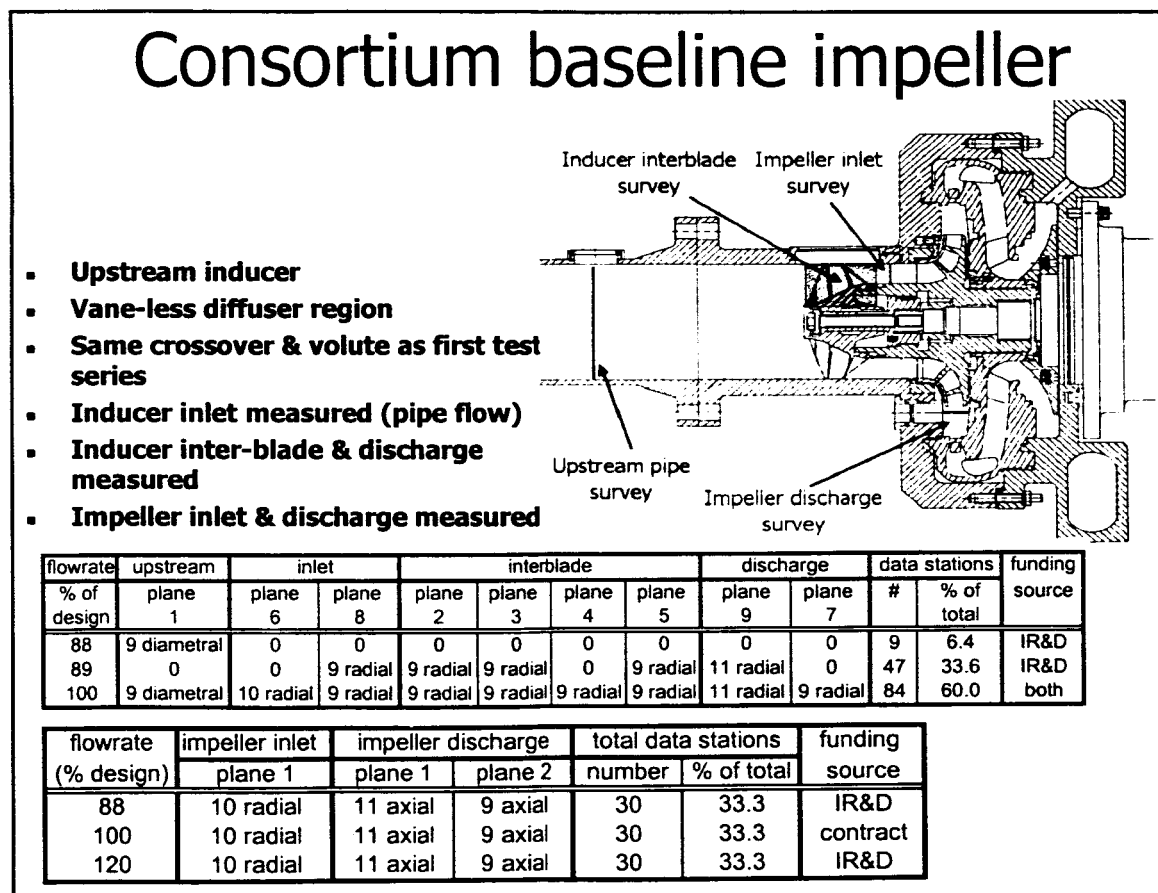

Consortium baseline impeller

- Upstream inducer
- Vane-less diffuser region
- Same crossover & volute as first test series
- Inducer inlet measured (pipe flow)
- Inducer inter-blade & discharge measured
- Impeller inlet & discharge measured

flowrate	upstream	inlet		interblade				discharge		data stations		funding
% of design	plane 1	plane 6	plane 8	plane 2	plane 3	plane 4	plane 5	plane 9	plane 7	#	% of total	source
88	9 diametral	0	0	0	0	0	0	0	0	9	6.4	IR&D
89	0	0	9 radial	9 radial	9 radial	0	9 radial	11 radial	0	47	33.6	IR&D
100	9 diametral	10 radial	9 radial	9 radial	9 radial	9 radial	9 radial	11 radial	9 radial	84	60.0	both

flowrate (% design)	impeller inlet	impeller discharge		total data stations		funding source
	plane 1	plane 1	plane 2	number	% of total	
88	10 radial	11 axial	9 axial	30	33.3	IR&D
100	10 radial	11 axial	9 axial	30	33.3	contract
120	10 radial	11 axial	9 axial	30	33.3	IR&D

Figure 2. The CBI impeller tester setup and velocimeter dataplane locations.

Tester cross section

The purpose of this section is to show an overview of test setup in order to familiarize the user with the test hardware. The sheet contains a single black and white cross-sectional view of the tester setup with the main components identified. The sheet is 100% complete.
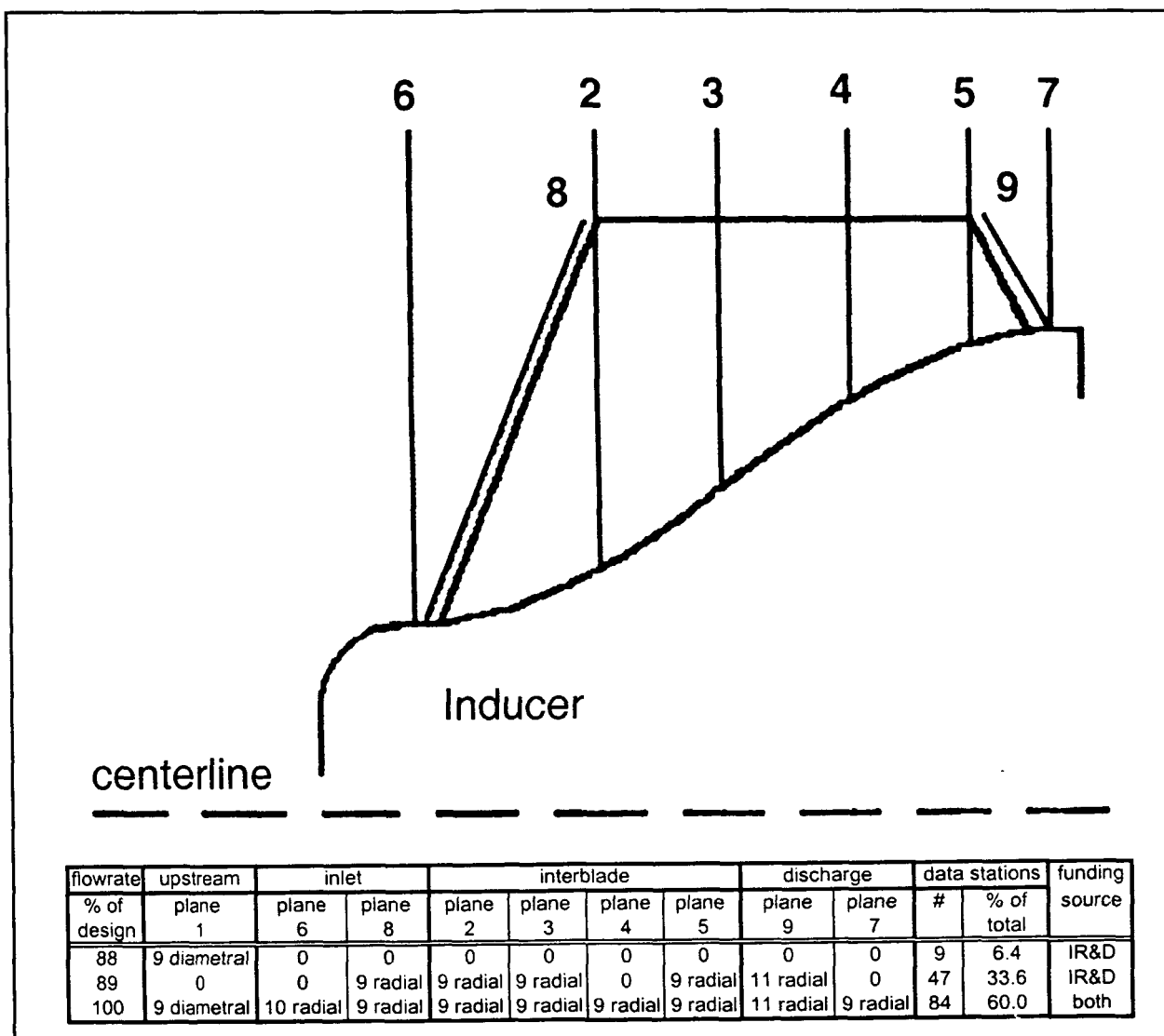

flowrate	upstream	inlet		interblade				discharge		data stations		funding
% of design	plane 1	plane 6	plane 8	plane 2	plane 3	plane 4	plane 5	plane 9	plane 7	#	% of total	source
88	9 diametral	0	0	0	0	0	0	0	0	9	6.4	IR&D
89	0	0	9 radial	9 radial	9 radial	0	9 radial	11 radial	0	47	33.6	IR&D
100	9 diametral	10 radial	9 radial	9 radial	9 radial	9 radial	9 radial	11 radial	9 radial	84	60.0	both

Figure 3. The location of the velocimeter dataplanes on the ADP inducer and the flow conditions of the testing.

Geometry and design info

The purpose is to provide basic hydrodynamic and geometric data on the components that comprise the tester. The table shows hydrodynamic design criteria and dimensions of the inducer, impeller, crossover and volute. The

sheet is 90% complete and is missing part numbers and dimensions of the crossover and volute.

Overall measurement matrix

The purpose is to provide a quick glance evaluation of what type of testing was performed, on which component and at which flow rates. The table shows the four major components of the tester, namely the inducer, impeller, crossover and volute, and for each delineates whether static, dynamic or total pressures were measured; whether laser velocimeter data was acquired on that component; and whether pump performance data were collected on a specific component. All of the information is keyed to show whether the data was acquired at design or off-design flow conditions. This sheet is 100% complete.

L2F measurement matrix

The purpose is to provide quick glance summary of parameters important to the laser velocimeter testing. This table links a variety of information to the laser velocimeter data including report numbers, test dates, type of laser velocimeter data collected (2D or 3D), number of planes of data acquired, where the data planes are located, how the multi-windowing was setup, etc. This information is provided as a function of component and flowrate. The table is 20% complete because it is formulated but not populated.

Laser monitoring files inducer

The purpose is to document the actual average flow conditions for the entire tester which were recorded during the laser velocimeter data acquisition segment on the ADP inducer. From the information contained in this large table, the user is free to verify flow conditions during each test or use the data to normalize the velocimeter data to a specific condition, for example to a constant inlet pressure or flowrate.

This table ties together general identification information such as test number, test date, overall test configuration, laser data filename and laser data experiment number with laser data position information, such as the location of the inducer axial data planes. All of this data is then correlated to two types of averaged data, the first being fundamental parameter measurements. These include general test parameters, like flowrate, pump speed, water temperature and torque as well as overall pump pressures recorded at locations such as the pump inlet, impeller inlet, upstream shroud, impeller discharge and pump discharge.

The second type of averaged data were calculated parameters based on measurements of pressures. These data have been corrected for transducer height and orientation relative to the pump centerline and include reference to the

PID and MDS numbers from the original data printouts. Included in the calculated parameters listing are general conditions such as flow ratio, inlet water density, vapor head, inlet NPSH, NSS and the impeller inlet flow coefficient. Other calculated parameters include the inducer inlet total pressure, the impeller inlet static pressure, shroud parameters, the impeller discharge static pressure, the inducer static-to-static headrise and the impeller static-to-static headrise.

The table is 20% complete as it is formulated but not populated. The table contains 8,960 entries in total.

Laser monitoring files impeller

The purpose is to document the actual average flow conditions for the entire tester which were recorded during the laser velocimeter data acquisition segment on the CBI. From the information contained in this large table, the user is free to verify flow conditions during each test or use the data to normalize the velocimeter data to a specific condition, for example to a constant inlet pressure or flowrate.

This table ties together general identification information such as test number, test date, overall test configuration, laser data filename and laser data experiment number with laser data position information, such as the location of the laser data positions at the impeller inlet and discharge. All of this data is then correlated to two types of averaged data, the first being fundamental parameter measurements. These include general test parameters, like flowrate, pump speed, water temperature and torque as well as overall pump pressures recorded at locations such as the pump inlet, impeller inlet, upstream shroud, impeller discharge and pump discharge.

The second types of averaged data presented are calculated parameters based on measurements of pressures. These data have been corrected for transducer elevation relative to the pump horizontal centerline as well as tap location relative to the pump horizontal centerline. These data include reference to the PID and MDS numbers from the original data printouts. Also included in the calculated parameters listing are general conditions such as flow ratio, inlet water density, vapor head, inlet NPSH, NSS and the impeller inlet flow coefficient. Other calculated parameters include the inducer inlet total pressure, the impeller inlet static pressure, shroud parameters, the impeller discharge static pressure, the inducer static-to-static headrise and the impeller static-to-static headrise. This table is 95% complete and needs a few missing parameters. The table contains 10,034 entries in total.

Pressure tap locations

The purpose of this section is to provide the user both a graphical overview, as well as the actual physical locations, as to where the various pressure taps were located on the tester housing.

The section contains a small table, two figures and several photographs. The table relates information on the axial, radial and angular location of the static pressure taps used in the testing. It includes the measurement location, the port ID, its axial and radial location, its angular orientation on the tester and reference to the drawing where the information was synthesized. There are also two figures in this section, the first is a to-scale rendering of the data contained within the table, showing all of the pressure tap locations on an analog of the tester housing. The second figure is an enhanced scan of part of a print showing the cross-sectional view of the tester. The figure relates the axial distance from the impeller blade leading edge to the plane of the impeller inlet and discharge static pressure taps.

Finally, there are nine scanned photos with graphical enhancements to illustrate the location of the static taps referred to in the table and previous figure. The photos also help to show the logic used to determine exactly which tap was which, since the available written records made that determination impossible. This sheet is 100% complete.

Laser station locations

The purpose of this section is to provide the user both a graphical look, as well as actual physical measurements, as to where the various laser velocimeter data stations were located relative to the components tested.

The section is divided into five parts. Each part is meant to be particular to just one of the four broad locations where the laser velocimeter data was acquired. To that end, each part contains both graphically enhanced scans of hardware prints as well as photos to illustrate the test setup for that part of the program. Additionally, each section contains either tables and/or to-scale figures (generated in MS Draw) which are used to explain the location of the laser data stations.

The first part shows a cross sectional view of the entire tester, with the four primary laser velocimeter data locations for this test series illustrated, namely the upstream pipe, ADP inducer including interblade region, CBI inlet and CBI discharge.

The second section centers around the upstream pipe inlet survey. Graphically enhanced scans of prints are used to illustrate the distance of this laser velocimeter survey plane from the nose of the inducer. A photo shows the

optical window port on the pipe while an incomplete table is supposed to give details of the inlet pipe survey locations relative to the pipe wall. The table is supported by an incomplete graphic showing the data stations in the inlet pipe.

The next section pertains to data acquired at the inlet to, within the blade rows of, and at the discharge of the ADP inducer. A figure shows the location of the velocimeter data planes on the inducer, while a photo shows the setup of the velocimeter during this phase of the testing. An in-complete table will provide the actual locations of the data stations along all of the data planes within the inducer.

The following section pertains to the measurements acquired at the inlet to the CBI. A figure is used to illustrate the location of the window and the laser data plane relative to the impeller. However, the figure shown does not actually contain a view of the inlet window, nor do any of the prints available for the task. The only way a truly appropriate view can be generated is to re-visit the prints on the CATIA database and create the custom view desired. An accompanying photo shows the setup of the laser velocimeter during the CBI inlet testing.

Finally, the last part of this section pertains to the measurements acquired at the discharge of the CBI. The graphically enhanced scan of the cross sectional view of the tester illustrates the location of the two radial planes where the data was acquired relative to the OD of the impeller. The photo shows the setup of the velocimeter and how the mirror was used to steer the beams into the window and to the region at the impeller discharge. The photo is followed by three nearly identical to-scale drawings of the discharge region of the CBI. The first figure concentrates on detailing physical dimensions in the region such as the width across the passage, the distance to the crossover, the size and location of the window, the size and relative spacing in front of and behind the impeller, etc. The second figure details the location of the data points along each of the two data planes in terms of the percent of the distance from the window inner surface to the back wall. The third figure presents this same data but expressed in actual distances (in inches), rather than percents of the local width. The final figure was also drawn to scale including the angle of the discharge of the impeller blades. This figure is used to explain the multi-windowing process used to acquire the CBI discharge data. In particular it shows the user relationship between the windowing number and the circumferential location of the impeller vane, and emphasizes the fact that data was acquired in the full to partial vane spacing separately from the adjacent partial to full blade spacing. This sheet is 60% complete with the items noted in the above sections needing completion.

Test number versus laser filename matrix

This sheet is designed to correlate the two file name tagging systems used during data acquisition. The test number refers to the Engineering Development Laboratory's method of naming and delineating test files, while the laser datafile

number refers to a bookkeeping reference used by the laser velocimeter. In particular the laser datafile number was used to correlate the data provided in the laser monitoring file printouts (which are the post-processed average tester and facility parameters, like flowrate, torque, inlet pressure, etc.) with the laser file name. This table also serves to provide a double historical reference to the original data files, if there is a need to refer to them again at some point. This sheet is 95% complete.

Data processing flow chart

The purpose of this sheet is to help explain the processing of the 2D laser velocimeter data. A good deal of effort went into the creation of this sheet but is justified for a number of reasons. Firstly, the chart is applicable to explaining the data processing for all of the impeller discharge data so it was widely useful. Secondly, since the velocimeter data was collected in the multi-windowing mode, it was necessary to explain the process in which these hundreds and hundreds of data points were aggregated to just a few dozen values. In this way, the user would be able to understand the process of the aggregation and how it compresses the data. Thirdly, the chart explains how the velocity components are derived, how the full- to- partial and partial- to- full blade datasets are aggregated together and finally, how the data is used to generate the plots for which the continuity calculations were based.

A problem with this sheet is that it never seems to print out exactly in the same format as it appears on the monitor (indeed, it only appears correctly on the monitor at 100% magnification). Instead, some entry always ends up getting distorted when printed. But since the database will most likely be used on a PC anyway, this is not a major drawback. This sheet is 100% complete.

ADP + CBI HQ data

The purpose of this sheet is to present the ADP and CBI head-versus-flow pressure data in a single location and in a simple, but complete format. This sheet is 100% complete.

Laser data inducer (3D data)

The purpose of this sheet is to present all of the 3D L2F data collected on the ADP inducer. This includes the data collected in the far upstream pipe, as well as the eight axial planes located throughout the inducer.

This is a very large data table due to the fact that data was collected in a total of 9 axial planes and at 2 flowrates. In addition, the 3D data contains two flow angles (one in the plane normal to the beam direction, the other in the plane containing the beams) for every data point, rather than just one. Consequently, there are a total of almost 9,000 entries in the table.

The table is 20% complete; with the table setup but not populated with L2F data, which comprises about 75% of the data entries in the table. Efforts on this table were sidelined in order to process higher-priority information.

Laser data impeller inlet (2D data)

The purpose of this sheet is to present all of the 2D L2F data collected at the inlet to the CBI.   This is an important sheet. It has data collected in the inlet annulus to the CBI at three different flow rates. The original raw data is collected in a single table at the top of the sheet. Subsequent tables build on this one and each subsequent table carries out a single operation on the data. The left side of the table contains information to generally identify the dataset. For example, the test number and date; the overall test configuration composed of location, flowrate and blade number; the laser data station position in terms of per cent of the flow annulus. The right side of the table has the actual velocimeter data, comprised of a total velocity and a flow angle as measured in each window of the multi-windowing process.

The next table further down on the same sheet shows the results which occurred when the relative angle between the laser spots and true vertical are corrected for each of the flow angles in each of the windows. Next, the L2F flow angle data is re-referenced to the impeller frame, in which the data is referenced with respect to the tangential direction of the impeller rotation. Next, the axial velocity component of the total measured velocity vector is calculated. Following this operation, the tangential velocity component is next calculated and placed in its own table.

At this point, the averaging of the data starts. First, the total velocity table with the re-referenced flow angles is copied and the circumferential average of the multi-windowed total velocity and adjusted flow angle is calculated. A more compact version of this table is then created in which the L2F data collected over two separate impeller blade-to-blade spacings are averaged together. Two sub-tables present the overall circumferentially averaged total velocity and flow angle at the inlet to the CBI at the three flowrates. Small plots of average total velocity as a function of annulus width and average flow angle as a function of annulus width are generated next to the summary tables to show the overall data trends.

Beneath the total velocity and average flow angle table starts the section of the sheet with the averaged component data tables. The first of these is the axial velocity component which is first circumferentially averaged, and then the data from the two separate blade-to-blade spacings are averaged together. Small sub-tables to the right of the main table show the average axial velocity at the inlet to the CBI at each of the three flow rates. Finally a small plot of the average axial velocity as a function of flow annulus at the three flow rates is presented to show the overall data trends.

The process detailed above for the axial flow velocity component is then repeated for the tangential velocity component in a series of similarly constructed tables beneath the axial velocity tables.   This sheet is 100% complete.

Continuity at impeller inlet non-zero wall

The purpose of the continuity calculation sheet is to provide the user with a feel for the validity of the measured inlet data. This is accomplished by plotting the circumferentially averaged axial velocity component, fitting the data with a 6th order polynomial curve-fit equation, then using the equation to calculate the contribution of every 0.1% increments of the flow annulus width to the overall flow rate. This means the area of each 0.1% of the radius within the flow annulus is used along with the curve-fit equation of the axial velocity within that zone to calculate the contribution of each small zone to the overall flow rate. The contributions are summed and converted into gallons per minute.

The process is carried out for all three flow rates for which the data was collected. The process did not force the axial velocity at the boundaries (i.e., the inner window surface and the hub of the impeller) to be zero, but rather used whatever velocity the curve-fit equation calculated at the boundaries. The results showed continuity matches relative to the actual facility flowmeter measurements of about 98%. The graphs for each flow rate used are color-coded to match the organization of the tables from which the data is extracted.   This sheet is 100% complete. Details are available in appendix A.

Continuity at impeller inlet no-slip conditions

The purpose of this sheet is to offer another view of the continuity calculation procedure in which the velocity at the boundaries was forced to zero velocity, which is also known as the no-slip boundary conditions. The same averaged axial velocity was plotted but the 0% and 100% radius locations were given the velocity of 0.00 m/s before the 6th order polynomial curve-fit equation was determined. From that point, the methodology was the same as far the non-zero wall case in the previous sheet. The results showed the continuity calculations agreed with the facility flow meters within about 93%. This sheet is 100% complete. Further details are available in appendix A.

Continuity at impeller inlet summary (sensitivity to adjustment factors)

This sheet is included because it was spurred by questions as to the sensitivity of the continuity calculations to the angle adjustment factors that were made on the original raw L2F data in previous tables. The purpose of the sheet is to summarize the results of a series of iterations performed on the data in which the angle adjustment factors were changed by an arbitrarily small +/- 1 degree amount. The adjustments were done at all three flow rates and using both the non-zero and no-slip wall boundary conditions. The results show that a

+/- 1 degree change in the overall correction factors leads to between a +/- 2% to +/- 5% change in the calculated integrated flow rate at the inlet to the CBI. A 15-page document is included in the appendix to provide the details of this section. This sheet is 100% complete.

Laser data impeller discharge (2D)

The purpose of this sheet is to present all of the 2D L2F data collected at the discharge to the CBI. This is an important sheet. It has data collected in the discharge region of the CBI at three different flow rates and at two different radial planes. The original raw data is collected in a single table at the top of the sheet. Subsequent tables build on this one and each subsequent table carries out a single operation on the data. The left side of the table contains information to generally identify the dataset. For example, the test number and date; the overall test configuration composed of location, flowrate and blade number; the laser data station position in terms of per cent of the flow passage at both radial planes, etc. The right side of the table has the actual velocimeter data, comprised of a total velocity and a flow angle as measured in each window of the multi-windowing process.

The next table further down on the same sheet shows the results which occurred when the relative angle between the laser spots and true vertical are corrected for each of the flow angles in each of the windows. Next, the L2F flow angle data is re-referenced to the impeller frame, in which the data is referenced with respect to the tangential direction of the impeller rotation. Next, the radial velocity component of the total measured velocity vector is calculated. Following this operation, the tangential velocity component is next calculated and placed in its own table.

At this point, the averaging of the data starts. First, the total velocity table with the re-referenced flow angles is copied and the circumferential average of the multi-windowed total velocity and adjusted flow angle is calculated. A more compact version of this table is then created in which the L2F data collected over two separate impeller blade-to-blade spacings are averaged together. Two sub-tables present the overall circumferentially averaged total velocity and flow angle at the discharge to the CBI at the three flowrates. Small plots of average total velocity as a function of the CBI B2 width and average flow angle as a function of B2 width are generated next to the summary tables to show the overall data trends.

Beneath the total velocity and average flow angle table starts the section of the sheet with the averaged component data tables. The first of these is the radial velocity component which is first circumferentially averaged, and then the data from the two separate blade-to-blade spacings are averaged together. Small sub-tables to the right of the main table show the average axial velocity at the inlet to the CBI at each of the three flow rates. Finally, a small plot of the

average radial velocity as a function of B2 width at the three flow rates is presented to show the overall data trends.

The process detailed above for the radial flow velocity component was then repeated for the tangential velocity component in a series of similarly constructed tables beneath the radial velocity tables. This sheet is 100% complete.

Continuity at impeller discharge non-zero wall

The purpose of this section is to present all of the continuity calculations that were performed at the discharge of the CBI using the non-zero wall method. This process uses the averaged radial velocities measured at plane 1, which is the plane nearest the impeller outer diameter. The calculations were performed in a two different fashions. In the first technique, the idea was to curve fit all of the data collected along the radial plane, from near the inner window all the way to near the back wall. Both of these two boundaries were located past the impeller B2 region. The rationale for including these data points in the calculation was the thought that the velocities measured in the far regions would counteract the velocities in the B2 region, thereby yielding a good average of the flowrate.

The second technique was to forgo the data collected outside the realm of the impeller B2 and instead use only the data from within the B2 region. Additionally, for this non-zero wall technique, the end point velocities (corresponding to the 0% and 100% B2 locations) were calculated using the 6th order polynomial curve fit on the radial velocity data from the entire discharge, created in the above step. This allowed the two end points to attain non-zero values. Next, a new curve fit was generated using these non-zero wall velocities, but only over the B2 region. The new curve fit equation was used to numerically integrate the equation in 0.1% increments as before to generate a single value for the flowrate.

Both techniques were applied to the data collected at 80%, 100% and 120% Qd with each section of the worksheet color-coded by flowrate to help differentiate the process. In addition, as part of a sensitivity analysis, the calculations using the second technique were expanded to investigate the effects of changing the location of the radial dataplane. Details of why this was studied are in appendix B for the CBI continuity calculations. The process, seen further down on this same sheet, was a simple matter of changing the radius at plane 1 from the nominal 4.647" to 4.547" (0.100" closer to the impeller) and 4.747 (0.100" further away) and re-running the calculations. This sheet is 100% complete.

Continuity at impeller discharge no-slip conditions

This sheet mimics the form and function of the prior sheet, but applies the no-slip boundary conditions to the radial velocity data within the impeller B2 region.

As before, the write-up in appendix B contains details of this procedure. This sheet is 100% complete.

Overall continuity summary and Alignment error analysis

These two sheets contain an assortment of graphics and tabular calculations. They are the source of much of the information contained in the supplementary continuity calculation procedure write-ups that are in appendix A, B, and D. They are both 100% complete.

Supporting documentation

Two documents were written to explain the continuity calculation procedures and how the sensitivity analysis was performed. One document was for the data at the CBI inlet and the other was for the data at the CBI discharge. Both of these documents are available in appendix A and B, respectively.

About a dozen other spreadsheets contain the calculations that go into the sensitivity analysis, i.e., in determining the effect on the continuity calculation of changing the factors that go into adjusting the flow angle data. These have been bundled together and are available in electronic format at the end of the report.

The COI database

This setup is for the ADP inducer coupled with the consortium optimized impeller (COI) which was followed by a vane-island diffuser (VID), a secondary crossover and then a facility volute. Velocimeter data was collected at the discharge of the impeller at a single radial plane and within the diffuser at seven planes spanning the space from a vane leading edge to the discharge of the vane. Pressure data was collected on the impeller and on the diffuser. For the CFD code validation efforts, it was assumed the inlet flow to the COI was the same as that for the CBI. No laser velocimeter data were collected at the COI inlet, which made implementation of this assumption necessary.

The database is actually split into two separate ones; one covering just the laser velocimeter measurements on both the impeller (discharge) and within the diffuser vanes, and the other covering the pressure measurements made within the diffuser passages.

Laser velocimeter database

Tester cross section

The first sheet in the workbook contains a black and white cross-sectional view of tester setup with the main components identified. The purpose of this

sheet is to familiarize the user with the test hardware by providing an overview of the test setup. A search through the available hardware prints failed to turn up a cross-sectional view of the tester which included the window used to gain optical access to the discharge of the COI. Such a view could be created by modifying some prints in CATIA, but this was not pursued due to budgetary considerations. With this shortcoming in mind, however, this sheet is deemed 100% complete for the purpose of providing an overview.

Consortium optimized impeller

- **Same inducer upstream**
- **Impeller close coupled to vane island diffuser**
- **Same crossover & volute**
- **Impeller discharge measured**
- **Diffuser inter-vane flow measured**
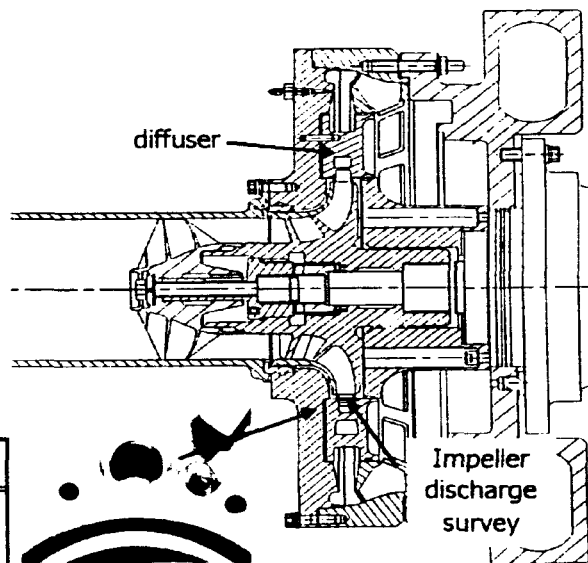
flowrate	discharge	total data stations		funding
(% design)	plane 1	number	% of total	source
30	11 axial	11	20.0	contract
60	1 axial	1	1.8	both
80	12 axial	12	21.8	both
100	20 axial	20	36.4	contract
120	11 axial	11	20.0	IR&D

flowrate	inlet window				passage window			total data stations		funding
(% design)	arc	throat	plane B	plane C	inlet	mid-way	discharge	number	% of total	source
80	0	15	0	0	15	15	15	60	33.9	IR&D
100	33	15	12	12	15	15.	15	117	66.1	contract

Figure 4. Locations of the velocimeter dataplanes at the discharge of the COI.

Geometry and design info

The purpose of the next sheet is to provide basic hydrodynamic and geometric data on the components that comprise the tester. The table shows hydrodynamic design criteria and dimensions for the inducer, impeller, diffuser, crossover and volute. The table is only partially filled out and therefore the sheet is only about 30% complete.

Overall measurement matrix

The following sheet is used to provide a quick glance evaluation of what type of testing was performed, on which component and at which flow rates. The table shows the five major components of the tester, namely the inducer, impeller, diffuser, crossover and volute, and for each delineates whether static, dynamic, or total pressures were measured; whether laser velocimeter data was acquired on that component; and whether pump performance data were collected on a specific component. All of the information is keyed to show whether the data was acquired at design or off-design flow conditions. The sheet is 100% complete.
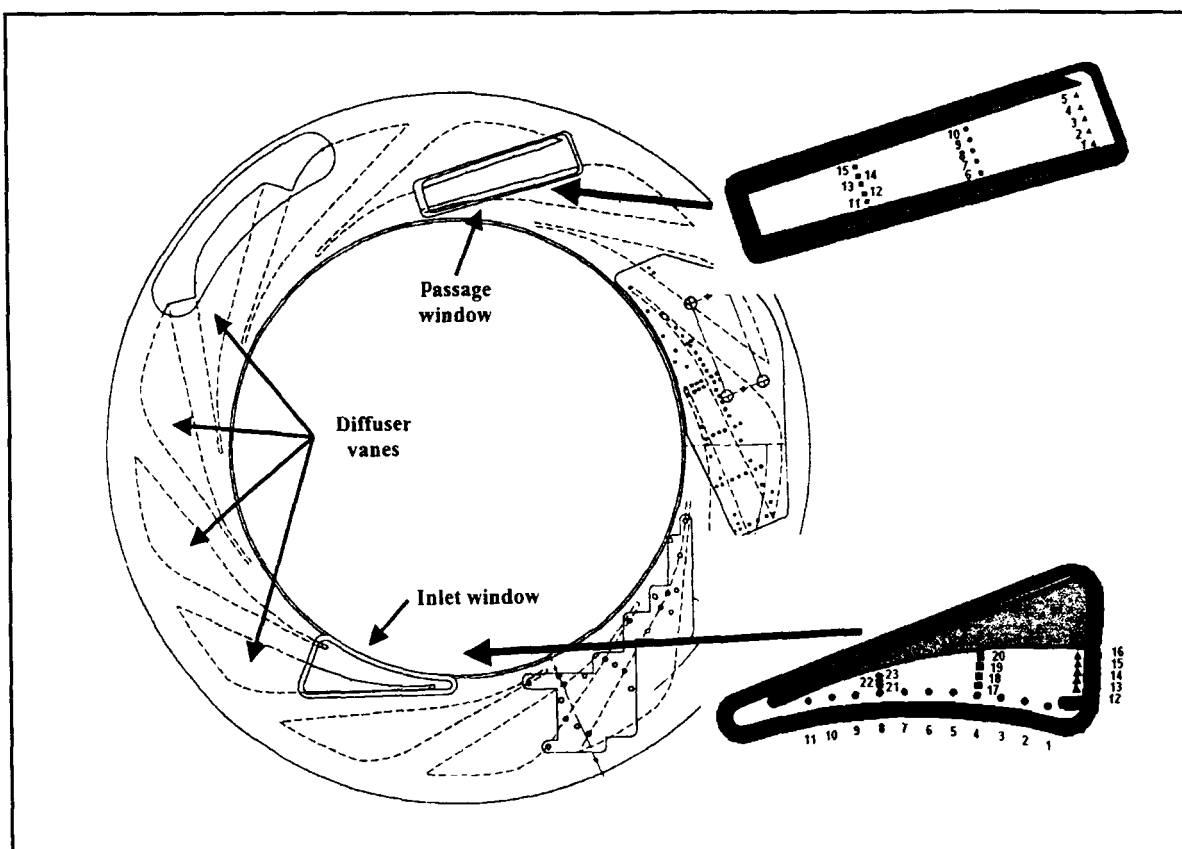
Figure 5. Locations of the velocimeter dataplanes within the VID. Data was acquired at the diffuser inlet and within a vane-island passage at the 39 points identified in the graphic and at three depth planes for each point as well.

L2F measurement matrix

This sheet is similar in concept to the previous one, but it is focused exclusively on the laser velocimeter measurements performed on both the impeller and the diffuser. The table links a variety of information to the laser velocimeter data including report numbers, test dates, type of velocimeter data

collected (i.e., 2D or 3D), the number of planes of data acquired, where the data planes were located, how the multi-windowing functions were setup, etc. This information is related as a function of component and flowrate. This table is only about 20% complete.

Laser monitoring files impeller

The goal of this sheet is to document the actual average flow conditions for the entire tester which were recorded during the laser velocimeter data acquisition segment on the COI. From the information contained in this large table, the user is free to verify flow conditions during each test or use the data to normalize the velocimeter data to a specific condition, for example to a constant inlet pressure or flowrate.

This table ties together general identification information such as test number, test date, overall test configuration, laser data filename and laser data experiment number with laser data position information which, in this case, refers to data acquired at the single radial plane at the impeller discharge. All of this data is then correlated to two types of averaged data, the first being fundamental parameter measurements. These include general test parameters, like flowrate, pump speed, water temperature and torque as well as overall pump pressures recorded at locations such as the pump inlet, impeller inlet, upstream shroud, impeller discharge and pump discharge.

The second types of averaged data presented are calculated parameters based on measurements of pressures. These data have been corrected for transducer elevation relative to the pump horizontal centerline as well as tap location relative to the pump horizontal centerline. These data include reference to the PID and MDS numbers from the original data printouts. Also included in the calculated parameters listing are general conditions such as flow ratio, inlet water density, vapor head, inlet NPSH, NSS and the impeller inlet flow coefficient. Other calculated parameters include the inducer inlet total pressure, the impeller inlet static pressure, shroud parameters, the impeller discharge static pressure, the inducer static-to-static headrise and the impeller static-to-static headrise.

This table is only 5% complete because it has been created but not populated with data from the printouts. The data to be entered are not available in electronic format and so must be entered by hand, which is a time consuming (and costly) process. Consequently, this activity was post-poned in order to work higher priority inputs to the database.

Laser monitoring files diffuser

The purpose, form and function of this sheet is similar to the previous sheet, but this sheet is specific to the data collected only during testing on the diffuser.

It too is only 5% complete due to a need to input the higher priority diffuser velocities and pressures into their worksheets instead.

Pressure tap locations

The concept behind this sheet was to present the user with both a graphical overview, as well as the actual physical locations, as to where the various pressure taps were located on the tester housing. The pressure tap locations referred to here are for the ones used to provide a measure of the impeller and diffuser performance parameters. These are not the same as, nor to be confused with, the 66 static pressure taps located at discreet points within the diffuser itself. This sheet is only 5% complete and needs to have graphics constructed to illustrate the location of the 13 diffuser discharge static pressure taps as well as the impeller discharge static taps. These graphics will be supported by photos of the hardware identifying the taps.

Laser station locations

This sheet will contain both graphics and tables of information relating the location of the velocimeter data stations to test hardware. This table is 0% complete.

Test number versus laser filename matrix

This sheet is designed to correlate the two file name tagging systems used during data acquisition. The test number refers to the Engineering Development Laboratory's method of naming and delineating test files, while the laser datafile number refers to a bookkeeping reference used by the laser velocimeter. In particular the laser datafile number was used to correlate the data provided in the laser monitoring file printouts (which are the post-processed average tester and facility parameters, like flowrate, torque, inlet pressure, etc.) with the laser file name. This table also serves to provide a double historical reference to the original data files, if there is a need to refer to the original data again at some point in the future. This sheet is only 5% complete.

Data processing flow chart

This sheet is a copy of the sheet with the same title in the CBI workbook. Although the workings of the flow chart are basically the same for the COI, there are some small changes that should be made to this chart to correct for the conditions at the discharge of the COI. For example, data was only collected at a single radial plane for the COI, but the flow chart refers to multiple planes. Additionally, a similar flow chart should be constructed to explain the data processing that is needed to convert the 3D velocimeter data to its sub-components. Therefore, this sheet if for reference only.

ADP + COI HQ data

The performance data for the COI will be presented in tabular format on this sheet. In addition, this sheet will contain another table with performance data on just the diffuser so its HQ curve can be constructed as well. Having this data in a single location will facilitate its use to make comparisons between CFD generated HQ predictions and actual measured HQ data. This sheet is 0% complete.

1996 laser data impeller discharge

The purpose of this important sheet is to present all of the 1996 2D L2F data collected at the discharge to the COI. It has data collected in the discharge region of the COI at three different flow rates and at a single radial plane. Unfortunately, the data at the two off-design flowrates was limited to measurements in the center of the impeller B2.

The 1996 dataset was selected over other years efforts for several reasons. First, this was the testing with the "original" COI. Because this impeller was damaged in subsequent years testing, it had to be remade. Although the other newer versions of the COI were nearly identical to the original one, there were slight differences. The chief difference between the 1996 data and others was the fact that the impeller wear ring was new in 1996. This means it was very effective in keeping the high pressure impeller discharge flow from forcing its way upstream past the wear ring over the impeller labyrinth seal. If a more significant recirculation flow was present at the impeller discharge in subsequent years, it might effect the pattern of the discharge flow, rendering it difficult to make year to year comparisons.

Secondly, the impeller discharge data from 2001 has its own set of flaws, the most serious of which is the fact that some of the data is possibly contaminated by changes to the impeller flowfield as a result of part of the diffuser breaking off and damaging the impeller, and/or the discharge Kiel probe damaging the impeller. Additionally, gaseous nitrogen was used to inject supplemental seed particles as one point during the testing. This was discovered after the fact to have changed the inducer performance for a period of several hours, thereby possibly changing the impeller flowfield as well.

As for the structure of this section, the original raw data is collected in a single table at the top of the sheet. Subsequent tables build on this one and each subsequent table carries out a single operation on the data. The left side of the table contains information to generally identify the dataset. For example, the test number and date; the overall test configuration composed of location, flowrate and blade number; the laser data station position in terms of per cent of the flow passage width at this radial plane, etc. The right side of the table has the actual

velocimeter data, comprised of a total velocity and a flow angle as measured in each window of the multi-windowing process.

The next table further down on the same sheet shows the results which occurred when the relative angle between the laser spots and true vertical are corrected for each of the flow angles in each of the windows. Next, the L2F flow angle data is re-referenced to the impeller frame, in which the data is referenced with respect to the tangential direction of the impeller rotation. Next, the radial velocity component of the total measured velocity vector is calculated. Following this operation, the tangential velocity component is next calculated and placed in its own table.

At this point, the averaging of the data starts. First, the total velocity table with the re-referenced flow angles is copied and the circumferential average of the multi-windowed total velocity and adjusted flow angle is calculated. A more compact version of this table is then created in which the L2F data collected over two separate impeller blade-to-blade spacings are averaged together. Two sub-tables present the overall circumferentially averaged total velocity and flow angle at the discharge to the CBI at the three flowrates. Small plots of average total velocity as a function of the CBI B2 width and average flow angle as a function of B2 width are generated next to the summary tables to show the overall data trends.

Beneath the total velocity and average flow angle table starts the section of the sheet with the averaged component data tables. The first of these is the radial velocity component which is first circumferentially averaged, and then the data from the two separate blade-to-blade spacings are averaged together. Small sub-tables to the right of the main table show the average axial velocity at the inlet to the CBI at each of the three flow rates. Finally a small plot of the average radial velocity as a function of B2 width at the three flow rates is presented to show the overall data trends.

The process detailed above for the radial flow velocity component is then repeated for the tangential velocity component in a series of similarly constructed tables beneath the radial velocity tables. This sheet is 100% complete.

Continuity at impeller discharge non-zero wall

The purpose of this section is to present the continuity calculations that were performed at the discharge of the COI using the non-zero wall method. This process uses the averaged radial velocities from the prior worksheet which were collected at the single plane located mid-way between the impeller OD and the diffuser ID. This plane was situated at a radius of 4.600" which located it 0.078" past the impeller OD. The continuity calculations were performed in a two different fashions, but had a common approach. The general process was to plot the relevant radial velocity data, apply a 6th order polynomial curve fit to it, then

use the curve fit equation to calculate the flow contribution in 0.1% increments across the flow region.

In the first technique, the idea was to curve fit all of the data collected along this radial plane, from near the inner window all the way to near the back wall. Both of these two boundaries were located past the impeller B2 region. The rationale for including these data points in the calculation was the thought that the velocities measured in the far regions would counteract the velocities in the B2 region, thereby yielding a good average of the flowrate.

The second technique was to forgo the data collected outside the realm of the impeller B2 and instead use only the data from within the B2 region. Additionally, for this non-zero wall technique, the end point velocities (corresponding to the 0% and 100% B2 locations) were calculated using the 6th order polynomial curve fit on the radial velocity data from the entire discharge, created in the above step. This allowed the two end points to attain non-zero values. Next, a new curve fit was generated using these non-zero wall velocities, but only over the B2 region. The new curve fit equation was used to numerically integrate the equation in 0.1% increments as before to generate a single value for the flowrate.

Because there were only two datapoints at the off-design flow rates, the continuity calculations were only made at the 100% design flow rate point. The first technique, using the "wall-to-wall" approach yielded a continuity match of about 94% compared with the measured facility flowrate via flowmeters. The second technique, using only data across the B2 but with non-zero wall velocities, yielded about 96%.

Continuity at impeller discharge no-slip conditions

This sheet mimics the form and function of the prior sheet, but applies the no-slip boundary conditions to the radial velocity data within the impeller B2 region. Like the second integration technique, this method ignores data collected outside the realm of the impeller B2 and instead use only the data from within the B2 region. For the no-slip condition, the end point velocities corresponding to the 0% and 100% B2 locations, were defined to be equal to zero. Then, a 6th order polynomial curve fit equation was calculated for this data set, which had zero velocities at the boundaries, but the real measured radial velocities at the other locations within the B2. As before, the curve fit equation was numerically integrated in 0.1% increments to generate a single value for the flowrate.

Due to the lack of sufficient quantity of data at the off-design flow rates, the procedure was only applied to the case of 100% design flow. The result was a continuity match of 92.3%. Further down on the sheet, the calculations were repeated but with radial location of the dataplane changed from 4.600" to 4.547", or only 0.025" past the impeller OD (nominal was 0.078" beyond the impeller OD). In another iteration, the radius was changed to 4.647", or 0.125" beyond

the impeller OD. This data was used to evaluate the sensitivity of the continuity calculations to perturbations in the location of the impeller discharge radial data plane. The results showed the continuity calculations were not very sensitive to this factor, since the integrated flow rate was 91.3% for the smaller radius, and 93.3% for the larger radius. This sheet is 100% complete.

Overall continuity summary and Alignment error analysis

Due to a lack of time and budget, these sheets were not completed. It is expected, however, that the analysis will show results similar to that seen at the discharge of the COI. This is due to the commonality of the alignment approach between the setups for the two impellers. This sheet is 0% complete.

Diffuser laser station roadmap

This worksheet has tables which relate positional information about the twenty four data stations at the diffuser inlet window and similarly about the fifteen data stations within the diffuser passage. The first table tags the laser ID with the data station identifier from the prints. From the same print, the rectangular and polar coordinates of the data stations are given. The adjacent table re-references the data stations to the coordinate system used to locate the static pressure taps. With this information, the plots below these tables show the coincidence of location between the laser data stations and the static pressure taps, as was the intent.

Further down on the sheet, the next table conveys the same type of information about the passage window data points, including a table with the points re-referenced to the static pressure tap frame. A plot illustrates the coincidence of the passage data points with the passage static taps, as intended.

Still further down on the sheet are a couple of figures. The first set illustrates the diffuser laser data station number and where the station is located relative to the diffuser vane. The associated laser data plane is also identified in the accompanying figure. The other set of figures illustrates the same concept but for the stations located in the passage window. A comprehensive table tying the laser data stations to actual physical coordinates has not been completed. This sheet is about 80% complete.

Diffuser inlet L2F data (3D)

The diffuser L2F data had to be split between two separate worksheets, one for the data at the diffuser inlet and the other for the data in the diffuser passage, between two diffuser vanes. This was required because the processing of the two datasets differ. The passage window data requires more processing and a different kind of processing due to the fact that the passage window was tilted in

ways that the inlet window was not. In order to take the effects of these tilts on the data into account, the two datasets had to be segregated.

This will be a very large sheet composed of numerous tables. The top table contains all of the recorded 3D laser velocimeter data at the four different planes at the diffuser inlet. The table is color-coded to highlight the data collected at 80% Qd from that collected at 100% Qd. The table starts by noting the test number, test date, laser filename and laser experiment number, along with words to describe the general location of the dataplane, such as throat. The window is identified in another column followed by several columns which relate the data points general coordinates in Cartesian and rectangular coordinates for two different reference frames. Finally, the next columns flag the flowrate at which the data was acquired and the depth plane within the diffuser, meaning near the shroud, in the middle of the passage or near the hub.

After the identification and test condition parameters the next forty eight columns contain the raw 3D L2F data for each point. The total velocity data (in meters per second) are presented as a function of window number, of which there were sixteen. This is followed by another sixteen columns which contain the 2D flow angle in degrees (called alpha) as a function of window number. The 2D angle is the flow angle in the plane perpendicular to the beam propagation direction. The next sixteen columns have entries for the 3D flow angle in degrees (called beta), again as a function of window number. The 3D angle is the flow angle in the direction in the plane that contains the beam, but which is oriented either toward or away from the optical head.   At this point, all of the flow angles are relative only to the angle referencing system of the L2F optical heads. In subsequent tables, these flow angles will be made relative to the frame of the diffuser. In all, there are 4,224 velocity and flow angle values entered into this table.

Unfortunately, no further processing was done on the 3D L2F data.

Diffuser passage L2F data (3D)

This will also be a very large sheet composed of numerous tables. The top table contains all of the recorded 3D laser velocimeter data at the three different planes in the diffuser passage. The table is color-coded to highlight the data collected at 80% Qd from that collected at 100% Qd. Unlike the diffuser inlet data, the table shows that a complete complement of diffuser passage data was collected at all passage locations at both 80% and 100% Qd.

The table starts by noting the test number, test date, laser filename and laser experiment number, along with words to describe the general location of the dataplane, such as "middle plane". The window is identified in another column followed by several columns which relate the data points general coordinates in Cartesian and rectangular coordinates for two different reference frames. Finally,

the next columns flag the flowrate at which the data was acquired and the depth plane within the diffuser, meaning near the shroud, in the middle of the passage or near the hub.

After the identification and test condition parameters the next forty eight columns contain the raw 3D L2F data for each point. The total velocity data (in meters per second) are presented as a function of window number, of which there were sixteen. This is followed by another sixteen columns which contain the 2D flow angle in degrees (called alpha) as a function of window number. The 2D angle is the flow angle in the plane perpendicular to the beam propagation direction. The next sixteen columns have entries for the 3D flow angle in degrees (called beta), again as a function of window number. The 3D angle is the flow angle in the direction in the plane that contains the beam, but which is oriented either toward or away from the optical head. At this point, all of the flow angles are relative only to the angle referencing system of the L2F optical heads. In subsequent tables, these flow angles will be made relative to the frame of the diffuser. In all, there are 4,368 velocity and flow angle values entered into this table.

Although the velocity and flow angle(s) data have been entered into the first table, no subsequent post-processing was performed. A very detailed and lengthy write-up needs to be done to explain all of the particulars and peculiarities involved in post-processing 3D L2F data. In particular, this discussion needs to address how the 3D L2F operates in general; what adjustments have to be made to the data for angle corrections and why; and what processes are followed to derive the velocity components in the radial, axial and tangential directions. This last bit of information is needed in order to perform any sort of flow continuity calculations, which lend a degree of certainty to the data.

Intervane total velocity plot

In an effort to provide some sort of output for the CFD codes to benchmark, this worksheet was created. Because of delays in understanding how to process the three component (3D) data into radial, tangential and axial components, it was decided instead to create a benchmark that used the total 3D velocity. This benchmark plots the average 3D total velocity at each of the 15 points within the laser dataplanes, the five of which spanned the length of the diffuser passage, from the throat to the discharge. Average used here means the multi-windowed data were added together and divided by the total number of windows.

To start with, this sheet contains a graphic which illustrates the locations of the laser dataplanes within the diffuser, as well as the static pressure planes, which were coincident to the laser data planes. With reference to this graphic (figure 6), a table is presented which contains the measured total 3D L2F velocity at each of the points within the first laser dataplane. The velocities are given at

both 80% and 100% Qd. The velocities are marked by their local X and Y coordinate within the passage, and at the three axial planes near the shroud, in the middle of the passage, and near the hub.

Next, a 2D plot of the dataplane is graphed to scale using the total velocities at that dataplane and at the off-design flowrate. A second plot is created at the design flowrate. These plots assign the total velocity as a function of the local channel height and the local channel width at a point proportionally located to the axial plane near the shroud, in the middle and near the hub, as seen in figure 7.

This process is repeated for the other four dataplanes within the diffuser and their plots are done to the same scale as the first. This way, when comparisons are made, the sense of scale of the size of the flow passage as a function of distance is automatically included. This sheet is 100% complete.
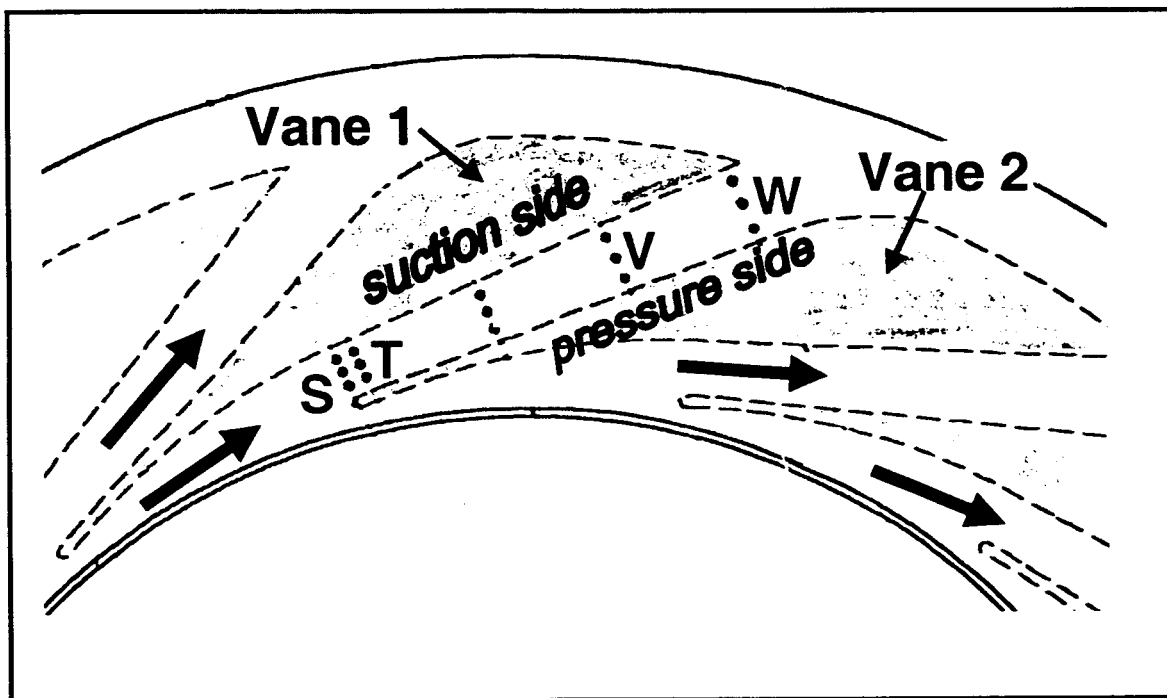
Figure 6. The static pressure measurement planes S, T, U, V and W were coincident in location with the laser velocimeter measurement planes.

Total velocity (m/s) within a vane passage at 80% Qd
Static planes S & T, laser plane B at inlet window
Flow into plane of the page
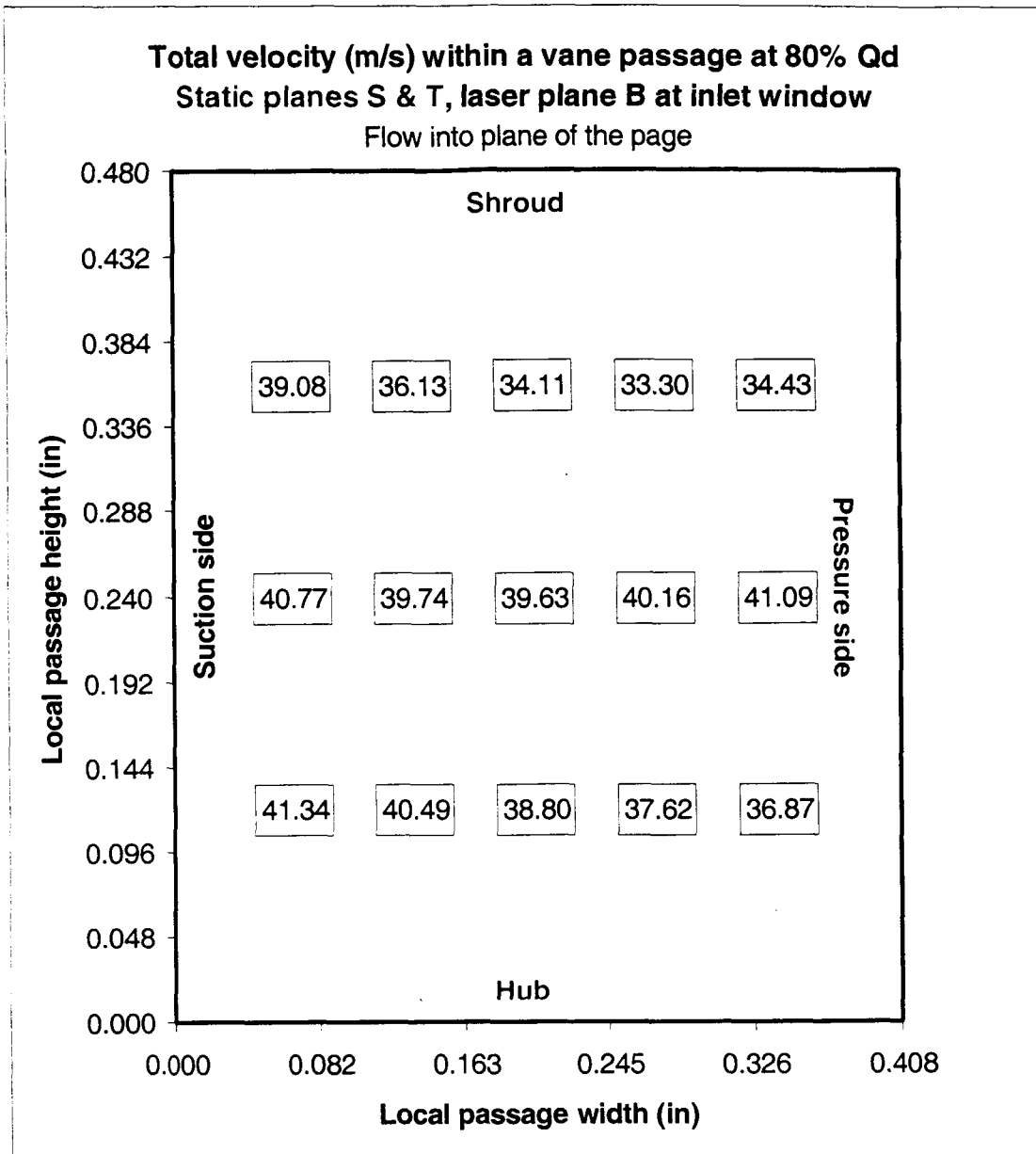
Figure 7. Total velocities measured at 80% Qd at laser plane B on the inlet window (near static planes S and T).

Total velocity (m/s) within a vane passage at 80% Qd
Static plane W, laser plane C at passage window

Flow into plane of the page
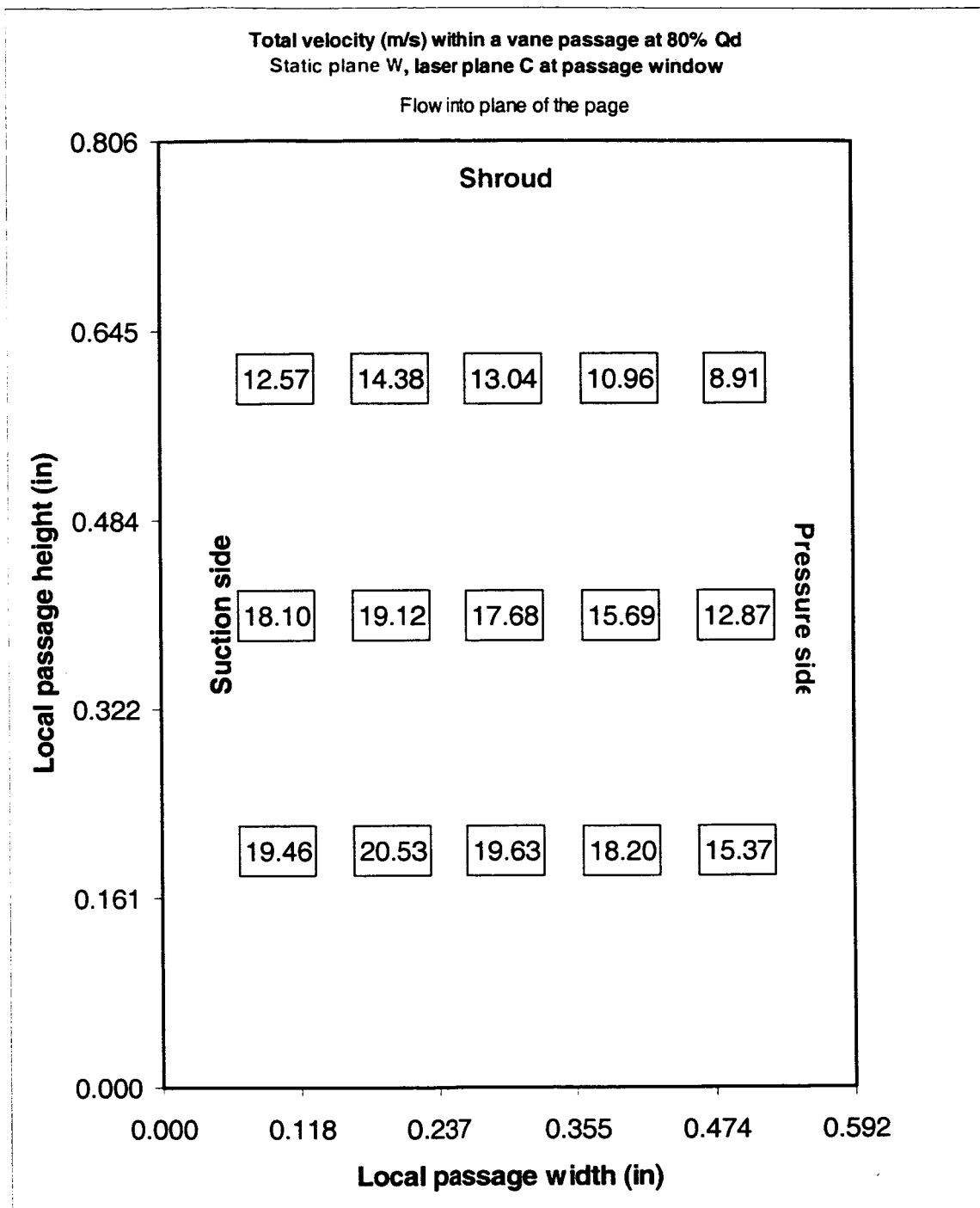
Figure 8. Total velocities measured at 80% Qd at laser plane C on the passage window (near static plane W).

Plane W 80% grid data ft per sec

Although the total 3D velocity plots presented in the previous worksheet are fairly straight-forward, an attempt was made to present this data as a color-coded velocity contour plot. This was accomplished by interpolating the 15 measured data points within that particular plane of the diffuser passage, and using the interpolated data to populate the entire plane with velocity data. From there, the data can be color-coded to reveal more details of the flow. In order to increase the resolution of the color-coding, the velocities were converted from their native meters per second units to feet per second.

This particular sheet shows how the interpolation was accomplished for the total 3D velocity measured at plane W at 80% Qd. First, the sheet was formatted so each cell was square in shape. Next, boundaries were drawn to represent the actual physical size of the passage at plane W; for example, the boundaries are located at row 2 for the shroud, row 81 for the hub (since the passage was 0.806" high at this plane); column B for the suction side of the vane, and column BH for the pressure side of the vane (since the passage was 0.592" wide at this plane). Some slight liberties had to be taken in the overall dimensions of the matrix of cells in order to be able to apply the interpolation scheme on an even number of spacings between data anchor points.

Next, the 15 actual velocity data points are entered into the cell which corresponds to each ones X and Y coordinate within the passage. Then the cells surrounding the passage boundary are all filled with zeros to represent zero wall velocities. The process of interpolation then begins with the data from the cell nearest to the hub and to the suction side of the vane. Its value is averaged with the zero wall velocity and the result placed in the cell which is located mid-way between the real velocity anchor point and the zero wall velocity point. This process is repeated on the cells closer to the side wall until they are filled. The process is also applied in the other direction, to the right of the original anchor point, using the neighboring measured value as the second anchor. After repeated application, the cells between the two anchor points are filled with averages. Finally, the anchor point nearest the pressure side vane is used along with the zero velocity at the pressure side vane wall to completely fill in this row.

This entire process is repeated at the other rows which contain real data anchor points. Then a similar process is applied in the vertical direction. The end result is that the scaled array of cells are filled with velocities which can then be color-coded over some range of values. It is interesting to note that this process has taken 15 data points and expanded them, through interpolation, to over 4,600! This sheet is 100% complete.

W at 80% Qd color contour

This sheet contains the results of applying the color coding to the total velocity matrix set up in the previous sheet. It contains a contour type plot of the velocity at plane W in the diffuser passage and illustrates the flow into the plane of the page, which represents flow into the diffuser passage. The color spectrum was chosen so that lower velocity values were represented by first part of the natural spectrum (red) and increasing values were represented by the latter parts of the spectrum (violet) on through black. The color plot clearly shows that for the flow conditions and location noted, the flow is basically jetting along the hub near the suction side of the vane.

Obviously, more sophisticated contour plotting software can be used on the data to create plots with a higher velocity resolution, and therefore, smoother graphics. This sheet and the previous one were created only to help illustrate what could be useful plots for the CFD comparisons. Figure 9 shows the results of the interpolative scheme for the flow at diffuser plane W. This sheet is 100% complete.
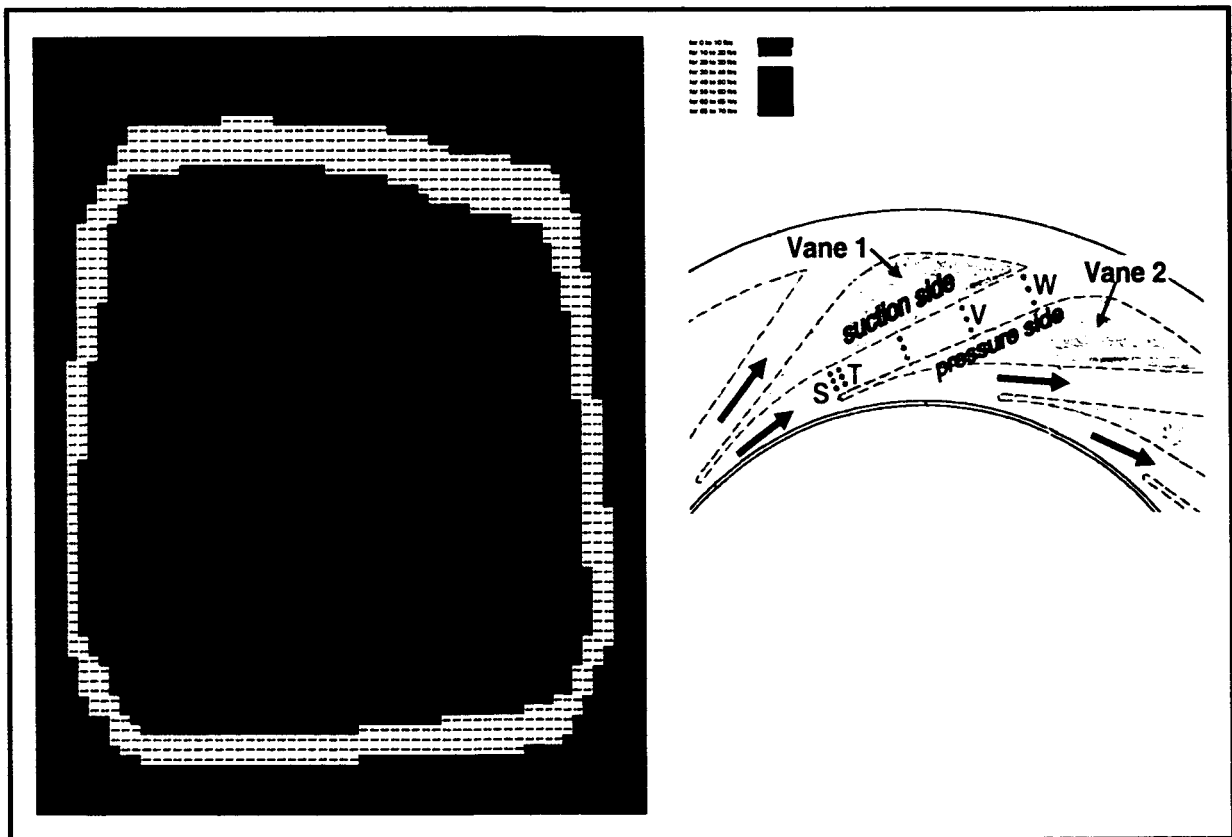
Figure 9. Interpolated total velocities at plane W at 80% Qd with flow into the plane of the page; suction side to the left, pressure to the right, hub below and shroud above.

Plane W 100% grid data ft per sec

This worksheet follows the exact same procedure as outlined above for the 80% Qd case, but uses the data for the 100% Qd case. The plane of the data is the same as before. This sheet is 100% complete.

W at 100% color contour

This sheet is analogous to the 80% Qd case with the plane of the data the same as before. This sheet is 100% complete.

Vane island diffuser static pressure database

Overall diffuser dimensions

The first sheet contains a black and white cross-sectional view of the diffuser alone. Basic part dimensions are given and in particular, the view seen defines the coordinate reference system. This information is required in order to relate the X, Y and/or R, theta coordinates of all of the pressure taps relative to the actual hardware. This sheet is 100% complete.

Static pressure tap locations

The next sheet is a graphic which shows the primary vane passage which was instrumented with 64 static pressure taps. The taps are identified by an alphanumeric callout, which has been color-coded to help delineate tap location relative to the diffuser shroud or hub. The graphic also defines the suction and pressure side of the vane so there is no confusion later as to which side is which when this reference is invoked. The overall direction of the flow through the component is also marked. This sheet is 100% complete.

Static pressure tap roadmap

This sheet takes all of the pressure tap locations shown on the previous sheet and presents the data in a logical tabular format, as seen in figure 6. Color-coding is used in the table to help differentiate the different entries in a logical fashion. The table has an alphabetical listing of the taps by major category, such as the A1 through A11, C1 through C13, D1 through D9, etc. This information is then referenced to the tap's generalized location, meaning before the throat, at the throat, or past the throat.

Next, four broad columns define whether the tap in question was located on the diffuser shroud, on the diffuser hub, on the vane pressure side or on the vane suction side. Further delineations in the shroud and hub columns are made to note whether the taps which were positioned between the vanes were located near the vane pressure side, in the middle of the passage or near the vane

suction side. A fourth category labeled "other" pertains to taps located before the throat but on either the shroud or the hub.
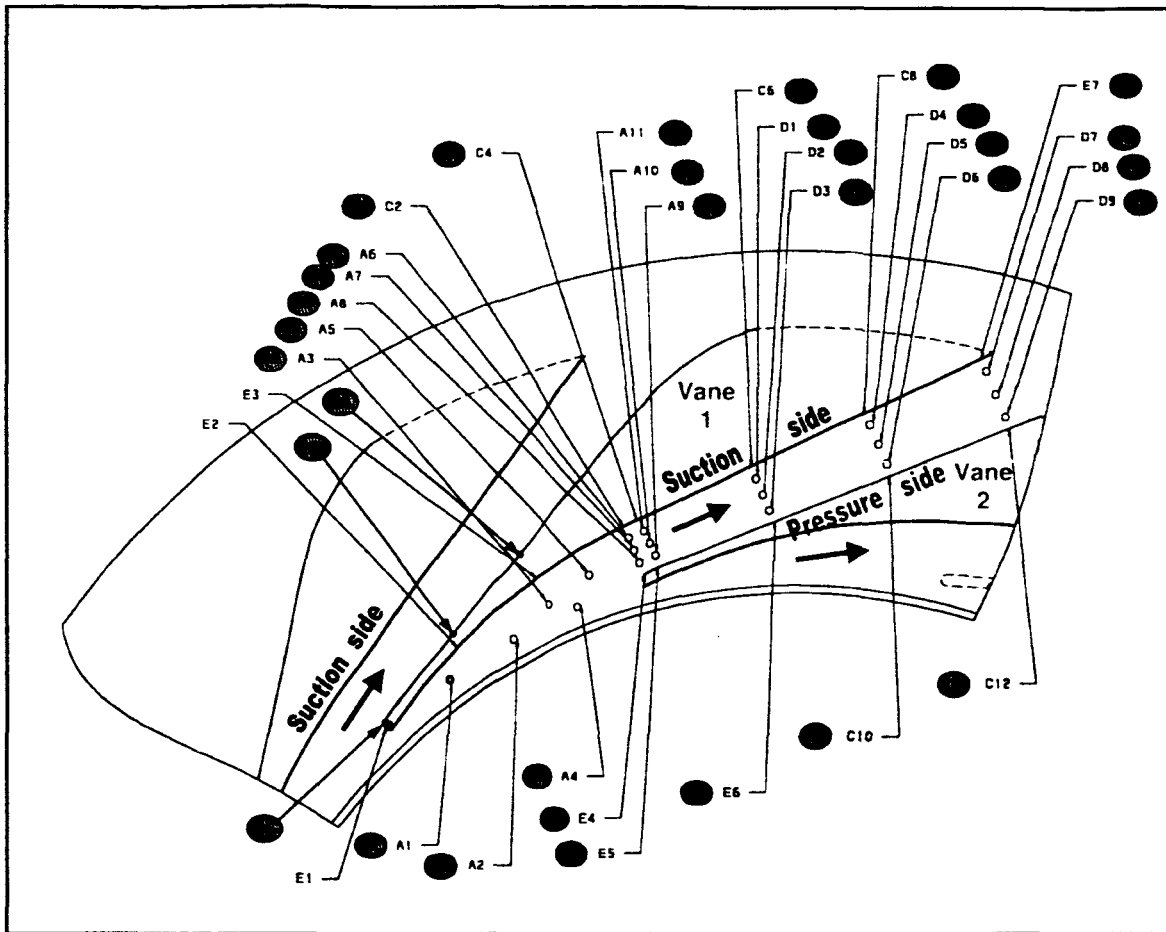
Figure 10. Location of the static pressure taps on the vane island diffuser. Vane 1 and vane 2 are identified. The blue arrows indicate the direction of the flow exiting the COI and flowing into the diffuser. The red lines indicates the pressure side of the vanes and the black lines indicate the suction side of the vanes. Taps which are in green colored circles are located on either the hub or, when referring to a tap located on the suction or pressure wall of a vane, are located near the hub. The other taps identified are either on the shroud, or when referring to a tap located on the suction or pressure wall of a vane, are located near the shroud.

For the taps actually located on a vane, a further subdivision is made to note their position as either near the shroud or near the hub. Sixty four of the sixty six taps are accounted for in the table, with two taps noted to be in-operable during the test. The organization of the table allows the user to quickly and easily identify the pressure taps. This sheet is 100% complete.

1996 Vane island diffuser static pressure tap map

note: taps D6 and E3 were dead and are not shown in the list

NVPS = near vane pressure side   NVSS = near vane suction side   NS = near shroud   NH = near hub

note: an inspection of the diffuser using a boroscope and a light source determined that taps C1, E1 and H2 were not machined in the right location as they all should have been on the suction side of the vane (pre-throat) near the hub. Instead they were machined on the pressure side of the vane.

alphabetical listing of the static taps	Generalized location			On the diffuser shroud between 2 vanes				On the diffuser hub between 2 vanes				On the vane pressure side		On the vane suction side	
	before throat	at the throat	after throat	other	NVPS	middle	NVSS	other	NVPS	middle	NVSS	NS	NH	NS	NH
A1	X			X											
A2	X			X											
A3	X			X											
A4	X			X											
A5	X			X											
A6		X					X								
A7		X				X									
A8		X			X										
A9			X		X										
A10			X			X									
A11			X				X								
C1			X										X		
C2		X												X	
C3		X													X
C4			X											X	
C5			X												X
C6			X											X	
C7			X												X
C8			X											X	
C9			X												X
C10			X									X			
C11			X										X		
C12			X									X			
C13			X										X		
D1			X				X								
D2			X			X									
D3			X		X										
D4			X				X								
D5			X			X									
D7			X				X								
D8			X			X									
D9			X		X										
E1	X													X	
E2	X													X	
E4		X										X			
E5			X									X			
E6			X									X			
E7			X											X	
F1			X								X				
F2			X						X						
F3			X						X						
F4			X								X				
F5			X							X					
F6			X						X						
F7			X								X				
F8			X							X					
F9			X								X				
G1	X							X							
G2	X							X							
G3	X							X							
G4	X							X							
G5	X							X							
G6		X								X					
G7		X								X					
G8		X							X						
G9			X						X						
G10			X							X					
G11			X								X				
H1		X											X		
H2			X										X		
H3		X											X		
H4			X										X		
H5			X										X		
H6			X												X
total number	12	11	41	5	4	5	5	5	5	5	5	5	8	7	5

Generalized location total: 64   Shroud total: 19   Hub total: 20   Vane pressure side total: 13   Vane suction side total: 12   Grand total: 64

Figure 11. A roadmap to explain the locations of the diffuser static pressure taps.

Static taps between vanes

The next sheet contains both graphics and tabular information and its primary purpose is to relate tap identification with physical measurements as to the tap location within the diffuser. For the fifty taps located downstream of the throat and between the two adjacent vanes, a table presents their name and general location along with the actual distance of the tap "plane" measured relative to the diffuser throat. A nearby graphic defines the names of these fives tap planes. Another graphic shows a generic cross-sectional view of the vane passage from a flow direction point of view and uses this to define the name of the taps located around the perimeter of the cross section.

A neighboring figure contains a scan of a cross-sectional view of the diffuser, and is used along with table above it, to give detailed dimensional data as to the location of the various taps at each of the five tap planes. The entries in the figure and table are color-coded to help with the identification of the taps.

Finally, another figure and associated table are provided to explain locations of three taps that were discovered, during the course of setting up the pressure database, to have been machined in the wrong locations on the diffuser. This sheet is 100% complete.

1996 diffuser static data

This sheet contains the bulk of the actual pressure data recorded at the pressure taps whose location was laid out and defined in the previous sheets. The data is from the 1996 test series. Although another data series was available from 1998, there was an overriding reason to use the earlier data. The 1996 data had been post-processed to take into account the height of the individual pressure tap transducer above the pump vertical centerline, as well as the height of the tap location on the tester itself above the pump vertical centerline. The 1998 data had not been post-processed in this manner, nor could it be post-processed now. Although the corrections are undoubtedly small, nevertheless the decision was made to use the more complete 1996 data only. Both sets covered a very wide flow range of 55% to 120% Qd so in that regard, they were equally valid.

Because the 1996 data was post-processed, it represents the average result at that particular static tap of data acquired over a 5 second period of time. The large data table is organized by tap alphabetical listing and gives the location in terms of both X,Y and Z coordinates as well as R, theta coordinates, with the zero reference defined in the first workbook sheet. At each tap, the average pressure is recorded as a function of flowrate (%Qd, with Qd defined as 1210 gpm) in 5% increments starting from 55% and ending at 120%. There are nearly 900 individual data points in the table (64 taps X 14 flowrates), after removing the

data from the two non-functional taps. The table is color-coded to group similar alpha-numeric tap groupings together.

A figure on this sheet contains a plot of the coordinates of the taps to assure their location relative to each other is correct. The plot compares well with the tap locations seen on the second sheet in the workbook. This sheet is 100% complete.

Pressure and suction side vane plots

It was not a goal of the database to create a lot of plots of the data, in part because there are so many ways to look at and present the data, which would have resulted in additional budget and schedule impacts. However, this sheet and the three following it, contain plots ostensibly to perform rudimentary data checks by looking for smooth trends as well as out-of-bounds data. It was also believed these plots might prove useful for quick comparisons to CFD results since their format is straightforward.

This particular sheet plots the data recorded on the pressure and suction side of the two adjacent vanes that define the passage. The data are presented as a function of distance downstream from the throat in order to look at the evolution of the flow through the passage. Consequently, it does not contain any data from the taps upstream of the throat. The data are from the taps located near the shroud as well as those located near the hub. The plots contain supplemental graphics to help identify the data planes within the passage in addition to the location of the tap relative to diffuser hub and shroud. All of the plots are basically repeated again in the lower part of the sheet but at an optimized vertical scale. The first group of plots are all at the same scale to facilitate easy comparisons between plots of a similar nature. This sheet is 100% complete.

Suction side vane only plots

On this sheet, data from the suction side only of the vane is plotted. Unlike the previous sheet, this set contains data from measurements upstream of the throat, all the way to near the leading edge of the vane. The data is presented in such a way as to show the evolution of the pressures along the suction side of the vane near the shroud, as a function of flowrate. Similar plots are constructed for the data measured on the suction side of the vane, but near the hub. Both plots contain color-coded supplemental graphics to help explain the location of the taps along the vane surface. One last plot combines the data from near the shroud with its complement from near the hub and plots that as a function of flowrate. This sheet is 100% complete.

Pressure side vane only plots

This sheet accomplishes the same goal as the previous sheet, but is for the data on the pressure side of the vane, rather than the suction side. Consequently, this set also contains data from measurements upstream of the throat, all the way to near the leading edge of the vane. The data is presented in such a way as to show the evolution of the pressures along the pressure side of the vane near the shroud, as a function of flowrate. Similar plots are constructed for the data measured on the pressure side of the vane, but near the hub. Both plots contain color-coded supplemental graphics to help explain the location of the taps along the vane surface.

One final plot was made to illustrate an interesting observation that was made on the behavior of the flow from the region at the throat (plane S) to that measured a short distance downstream (plane T). The observation was that the static pressure on the pressure side of the vane near the shroud tended to coalesce to about 225 psia at plane T for flowrates of 100%, 95%, 90%, 85% and 80% Qd, while for flowrates above 100% or below 75%, the pressures all coalesced to a value of about 125 psia, or about 100 psia less. No explanation is offered for this observation at this point, and is merely mentioned as a point to ponder. This sheet is 100% complete.

Shroud and hub plots

The final sheet in this workbook once again turns attention on the flow in the passage just between the adjacent vanes. In this case, the data measured on the shroud and on the hub in this region were plotted as a function of distance downstream of the throat for four representative flowrates of 60%, 80%, 100% and 120% Qd. The data on the shroud are plotted separately from that on the hub, but the vertical scales are kept the same to facilitate easy comparisons amongst the plots. Once again, each plot contains supplemental graphics to illustrate the locations of the data points within the passage. A second set of identical plots are presented below these originals. But here the vertical scale is adjusted in the individual plots to obtain maximum resolution of the pressure data.

Another group of plots presents the mean pressure at each plane on both the hub and shroud as a function of distance. The mean was defined as the average pressure of the three taps which composed the tap plane and which spanned the distance from the suction to the pressure side of the passage. These were plotted for the four representative flowrates as a function of distance from the throat. Once again, each plot contains supplemental graphics to illustrate the locations of the data points within the passage. A second set of identical plots are presented next to these originals, where the vertical scale is adjusted in the individual plots to obtain maximum resolution of the pressure data. This sheet is 100% complete.

Concluding remarks

The task to create multiple, detailed and thoroughly documented databases composed of turbomachinery component tests proved too large to complete within the budget constraints of this project. However, there is enough degree of completion to both the CBI and COI databases to prove useful for some CFD code anchoring. In particular, the CBI database contains a complete impeller inlet and discharge survey and component performance data. The COI has a complete impeller discharge survey and total velocities within the diffuser. Even without post-processing, the cross sectional total velocities measured within the diffuser passage should be useful for comparative purposes. Additionally, the VID database contains complete pressure data over a very wide flow range, and the locations of the pressure taps have been thoroughly documented. The SSME HPFTP database is the most incomplete, but potentially is very useful because it will have another impeller inlet and discharge survey at four complete flowrates and two radial planes, as well as a well defined, 10-point total pressure survey (via Kiel probe) at the impeller discharge.

Appendix A

Concerning the continuity calculations for the CBI inlet flowfield survey

The inducer and the impeller were physically connected so the clocking or angular spacing between the blades of the two components was fixed, as seen in figures 1 and 2. Since the impeller had six full blades at the inlet, while the inducer had only four blades at the discharge, it was decided to collect data over two separate, but adjacent 90 degree circumferential arcs. This way, if there was any difference in the flow in these regions due to an interaction between the blades of the two components, it would be discernable.

In this test series, multi-windowed means the measurements were collected in a 90 degree circumferential band which was time phased to the rotation of the impeller and located axially between the inducer and impeller. The circumferential zone was sub-divided into sixteen smaller zones called windows which each encompassed 5.625 degrees of arc. For the CBI inlet survey, data comprised of total velocity and flow angle was acquired in each of these 16 windows in the 90 degree circumferential arc. This dataset was referred to as data from "blade 1".

Next, the process was repeated but this time for data collected in the adjacent 90 degree space and this dataset was referred to as data from "blade 2", as seen in figure 3. The entire process of collecting data from "blade 1" and "blade 2" was repeated at each of the ten radial points set up in the flow annulus between the discharge of the inducer and the inlet of the CBI. The first calculation methodology utilized all of the multi-windowed data but averaged the data from all 16 windows it to a single value at each of the ten radial points in the flow annulus.

Although there were two complete data sets, post-processing revealed there were no meaningful differences in the data. So the two data sets, from "blade 1" and "blade 2", at each particular radial station within the annulus were averaged together. From the averaged total velocity and flow angle, the axial and tangential velocity at each radial point within the annulus was calculated and tabulated. Since only the axial velocity component contributes to the flow rate calculation, the average axial velocity at all ten radial stations was plotted as a function of annulus width and a polynomial curve fit applied. Note that the "R^2" parameter, which is an indication of the "goodness" of the curve fit, was very close to 1.000, or perfect, for this methodology, as well as for the other methodologies to be discussed.

Measurements within the flow annulus spanned from a position corresponding to 10% of the annulus width to 95% of the annulus width. For the first continuity calculations, the end points, corresponding to the 0% and 100% annulus locations, were allowed to attain a non-zero value as determined by the

polynomial. For example, the curve fit equation for the case illustrated in figure 4 shows the velocity at the 0% boundary (the impeller hub) would be 8.43 m/s. The curve fit equation was then numerically integrated in 0.1% increments over the range of the data. Using this technique, continuity matches of about 98% were achieved at the CBI inlet for all three flowrates studied.

The modified version of the original methodology used the averaged axial velocity data but included zero velocities at the walls as part of the data set which was subsequently plotted and fit with a polynomial curve equation. Using this approach, seen in figure 5, continuity matches of about 93% were achieved at the CBI inlet at all three flow rates.

Since the integrated flowrate calculations at the CBI inlet were lower than the flowmeters indicate, it is possible the "missing flow" can be attributed to the radial component of the velocity. The measurements at the CBI inlet were made with the 2D L2F which can only measure the flow in the plane normal to the beam direction. Hence, the total velocity measured in this normal plane can be resolved to tangential and axial flow components, but not radial components. A check of the 3D data recorded at the discharge of the ADP inducer should shed some light on this possibility.

The laser velocimeter makes measurements in its own reference frame, in which, for example, a flow going vertically straight up would be assigned a flow angle of 180 degrees. It is necessary to relate the velocimeters reference frame to the hardware in order to be able to use the data in a sensible manner. The process of relating the velocimeter and the hardware reference frames entails making adjustments to the raw velocimeter flow angles during the data post processing.

The total angle correction factor used at the CBI inlet was the sum of two components. The first component was the correction associated with the relative angle between the measurement volumes and true vertical. Since the pump shaft was measured via an inclinometer to be horizontal within 0.05 degrees, conversely, knowing the spots were exactly vertical allowed the velocimeter data to be referenced to the pump hardware. The relative angle was measured by the usual procedure of projecting the spots onto a distant screen onto which the shadow of a fine plumb wire was cast. The spots were rotated in 0.36 degree increments until they were aligned with the shadow of the plumb line. This process was repeated a total of fifteen times by two independent observers and resulted in a mean relative angle of 1.63 degrees with a standard deviation of 0.33 degrees. The mean angle was recorded and used in the post data processing. By adding this correction angle to the raw velocimeter angle data, the velocimeter data could be related to the tester frame.

The second component of the angle correction factor was the correction needed to relate the measurements relative to the tangential direction of the

impeller rotation. The CBI inlet measurements were acquired with the optical head set up on the north side of the powerhead (figure 6), and the impeller rotating clockwise when viewed from the inlet. From this perspective, the tangential direction was oriented straight up which nominally corresponded to the 180 degree angle in the velocimeter reference frame (ignoring the relative angle offset with true vertical for the moment). Because we knew the shaft was horizontal and we had corrected the velocimeter reference frame to be exactly vertical, we therefore concluded the angle between the tester and the laser measurement volumes was 90 degrees.

Consequently, after the true vertical correction angle was added to each raw velocimeter angle data, the second correction was to subtract these values from 180 degrees in order to relate the flow angle relative to the tangent to impeller rotation. For example, a typical measured flow angle of 145 degrees was corrected to 146.63 degrees relative to true vertical and then converted to 33.37 degrees relative to the tangential direction of impeller rotation, as illustrated in figure 7.

To determine how sensitive the integrated flow calculations were to small changes in the angle correction factors used to convert the laser velocimeter reference frame to that of the tester, both integration methods (i.e., zero and non-zero wall velocities) were tried using a +1 degree and –1 degree change in the overall angle correction factors. The results, shown in table 1, indicate a +/-1 degree change in the angle correction factor leads to a +/- 2% to 5% change in the calculated flowrate.

Calculations were also made to assess the influence of possible mis-alignment of the laser velocimeter on the validity of the data. Mis-alignment can be defined as a physical setup of the velocimeter which unintentionally results in the measurement locations not being at the intended position within the flow annulus. In the case of the CBI inlet flow surveys, the flow region was an annulus bounded on one side by the hub of the impeller and on the other side by the tunnel ID. For the first mis-alignment case, the input laser beam was considered to be located at a range of distances displaced from the horizontal centerline of the pump, as seen in figure 8. This means the flow field measurements were not made along a radius to the pump, but rather along a chord located above (or symmetrically, below) the pump horizontal centerline. What this mis-alignment affects is the radial location of the data point, which in turn affects the plot of the data, the curve fit equation and ultimately, the continuity calculations.

The calculations, however, showed even a relatively large displacement (0.33") above (or below) the pump horizontal centerline resulted in only a 0.001" change in the radial location of the 50% datapoint (i.e., the point located at 50% of the annulus width). Presumably, similarly small changes would also be affected in the radial location of the other points within the flow annulus. In

addition, such a large displacement above or below the pump centerline would have been detected since the displacement results in a mis-measurement of the annulus width by 0.100".

Actual alignment data derived from the laser speckle measured annulus width revealed a width of 1.059" compared with a measured distance of 1.060" (measured tunnel ID minus measured impeller hub diameter). Therefore, it was concluded the L2F was probably not mis-aligned above the pump horizontal centerline by 0.33" as it would have been noticed based on the disagreement between the measure of the flow annulus width.

Displacements above or below the pump centerline which were smaller than 0.33" were possible, but the analysis also showed smaller displacements would not have affected the radial location of the data points by even 0.001", which is too small to affect the curve fit equations and subsequent continuity calculations. Therefore, small displacements above or below the pump horizontal centerline would not unknowingly adversely affect the continuity calculations.

The next mis-alignment studied was the affect of the input beam not traversing the annulus in a normal direction, i.e., perpendicular to the window, which is depicted in figure 9. There are two conditions resulting from this situation. The first is the data station locations are not at the same distance from the discharge of the inducer, as the beam path deviates from the intended path (figure 9). A simple analysis of this situation indicates for an input angle of 10 degrees to the normal, the difference in the axial location of the 10% and 95% data points (D3 in figure 9) would be about 0.119". However, for reasons given in the following paragraph, there is good reason to believe the input angle was less than 1 degree, in which case the difference in the axial location of the 10% and 95% data points would be about 0.012", which is probably small enough to ignore.

The second effect, illustrated in figure 10, is also a result if the L2F measurement volumes are inclined at an angle to the flow, namely the effective separation of the measurement volumes are less than the true separation. This would directly influence the accuracy of the velocities measured. An analysis of the optics involved in the second scenario showed incident angles as large as 10 degrees to the normal would result in a change in the effective separation of the L2F spots of less than 1%.

In addition, a 10 degree incidence angle would result in the reflected laser light from the outer surface of the window reflecting back onto the optical head at a 20 degree included angle. This reflection would be laterally displaced on the transceiver lens of the L2F optical head by a distance of over 3 inches. Such a large displacement would have been readily noticed and corrected. Current alignment procedures strive to overlap the incident and reflected light cones onto the transceiver lens to within 0.25" of each other. This would decrease the non-

perpendicularity of the incident angle relative to the normal to less than 1 degree, which in turn means the change in the effective separation of the measurement volumes would be less than 0.01%. Consequently, mis-alignment of the input beams at the CBI inlet resulting in a non-perpendicular beam path through the flow annulus has no substantial effect on the total velocity measurements, and hence no effect on the continuity calculations.

Summary

A continuity check was performed on the CBI inlet flow survey using the laser velocimeter data. The data are adjusted to bring them into the reference frame of the impeller and the axial velocity component is calculated. Using the axial velocities as a function of annulus width, a polynomial curve fit is applied to the data. If the curve fit allows non-zero wall velocities to be used, the integrated flowrates agree with facility flowmeters within about 98% at all three flowrates studied. If the curve fit is constrained to use zero-wall velocities, the agreement decreases to within about 93% of the flowmeter recorded values.

Calculations were performed to determine the sensitivity of the continuity calculations to small changes in the factors used to convert the raw angle data into the frame of the tester. A +/- 1 degree change in the factors causes a +/- 2% – 5% change in the calculated flowrate. The influence of alignment error sources was modeled and determined a mis-alignment above the pump centerline or a mis-alignment resulting in a non-perpendicular beam path had no appreciable effect on the calculated flowrate.

Recommendations

1. Future laser velocimeter data measurements should strive to acquire data nearer to the boundaries of the flow channel in order to better anchor the polynomial curve fit. A data point at the location equal to 1% of the flow annulus width on both sides of the annulus (i.e., hub and tunnel ID) would be ideal.

2. A method of measuring the angle of an edge of the rotating timing mark machined onto the surface of the test hardware could possibly directly yield the total angle correction factor, in a more direct fashion and with greatly increased accuracy, perhaps approaching +/- 0.2 degrees. This is especially important as analysis indicates small errors (on the order of +/- 1 deg) in the process of converting the raw angle data into the reference frame of the tester can lead to large uncertainties in the integrated flowrates on the order of 5% at the inlet and 15% at the discharge of an impeller.

3. Routine recording of the measured flow angle of seeded jets oriented at specific angles will enable a permanent record of the L2F angle reference

system encountered with each tester setup. This is important because the velocimeter angle reference can vary depending on the L2F model used, whether mirrors are used to steer the beams and on the way the fiber optic receiving cables are connected to the signal processor optics section.
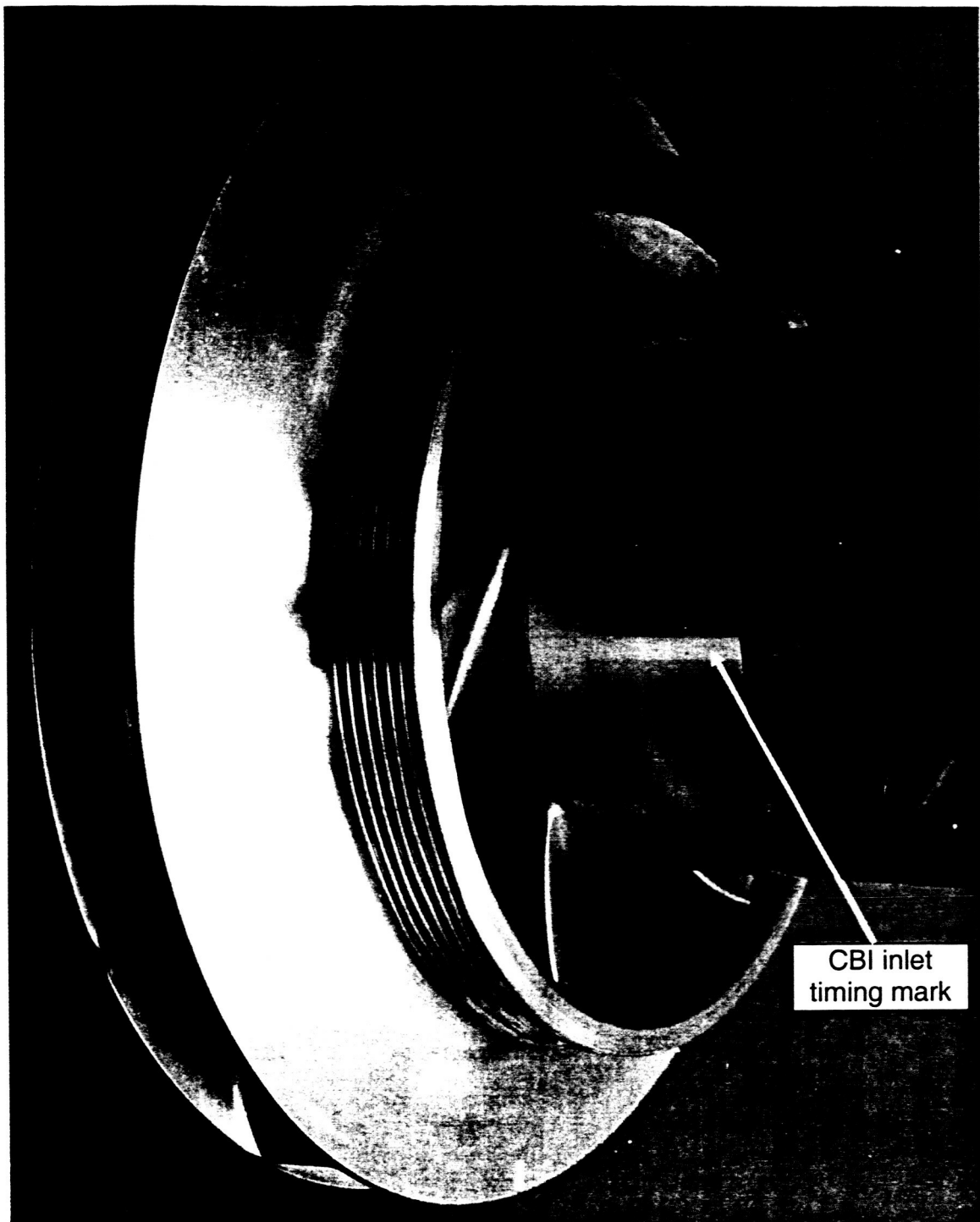
Figure 1. Photo of the CBI with the ADP inducer attached showing the CBI inlet timing mark and the fixed orientation of the blades of the two components relative to each other.
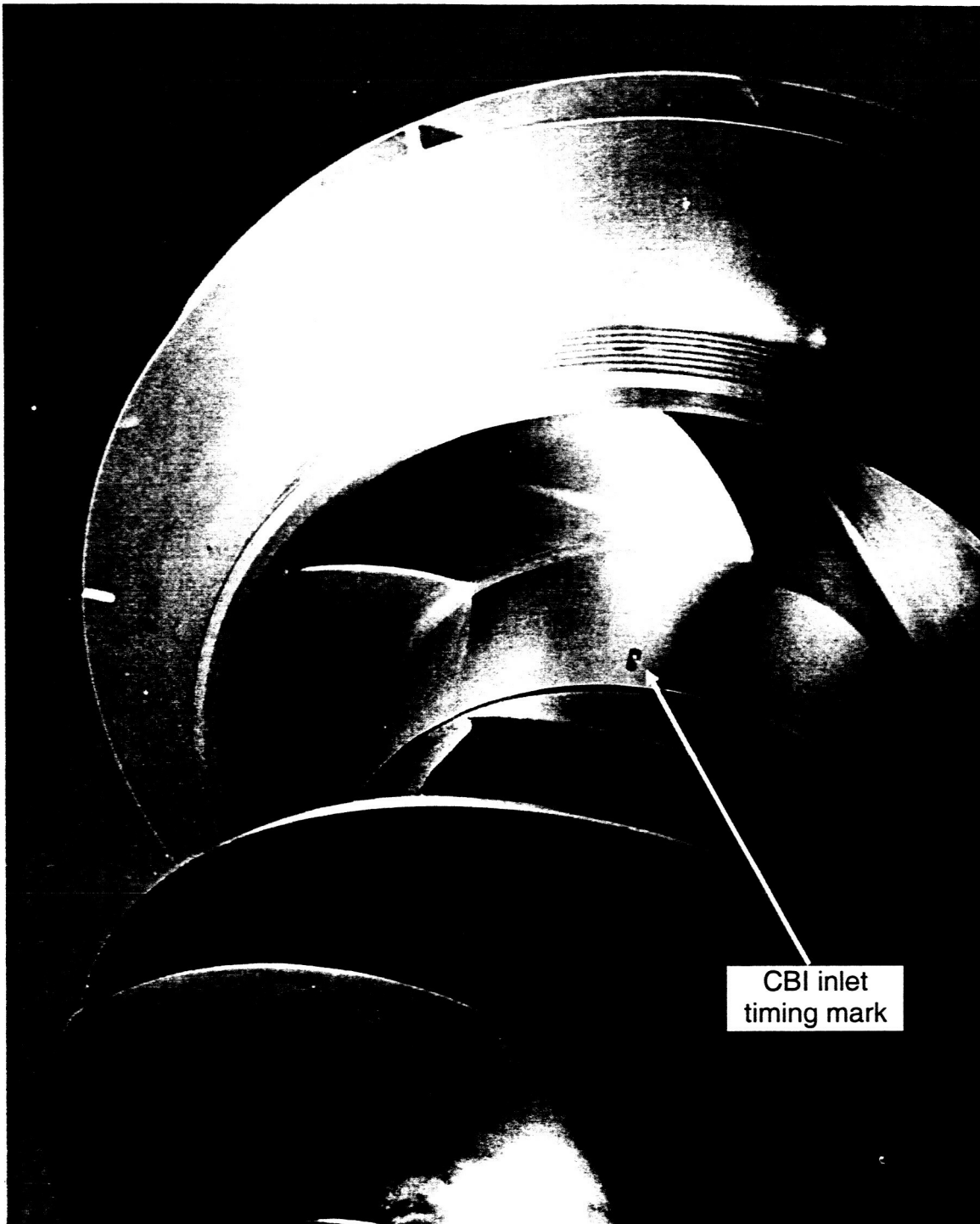
Figure 2. Second view of the CBI with the ADP inducer attached showing the CBI inlet timing mark and the fixed orientation of the blades of the two components relative to each other.
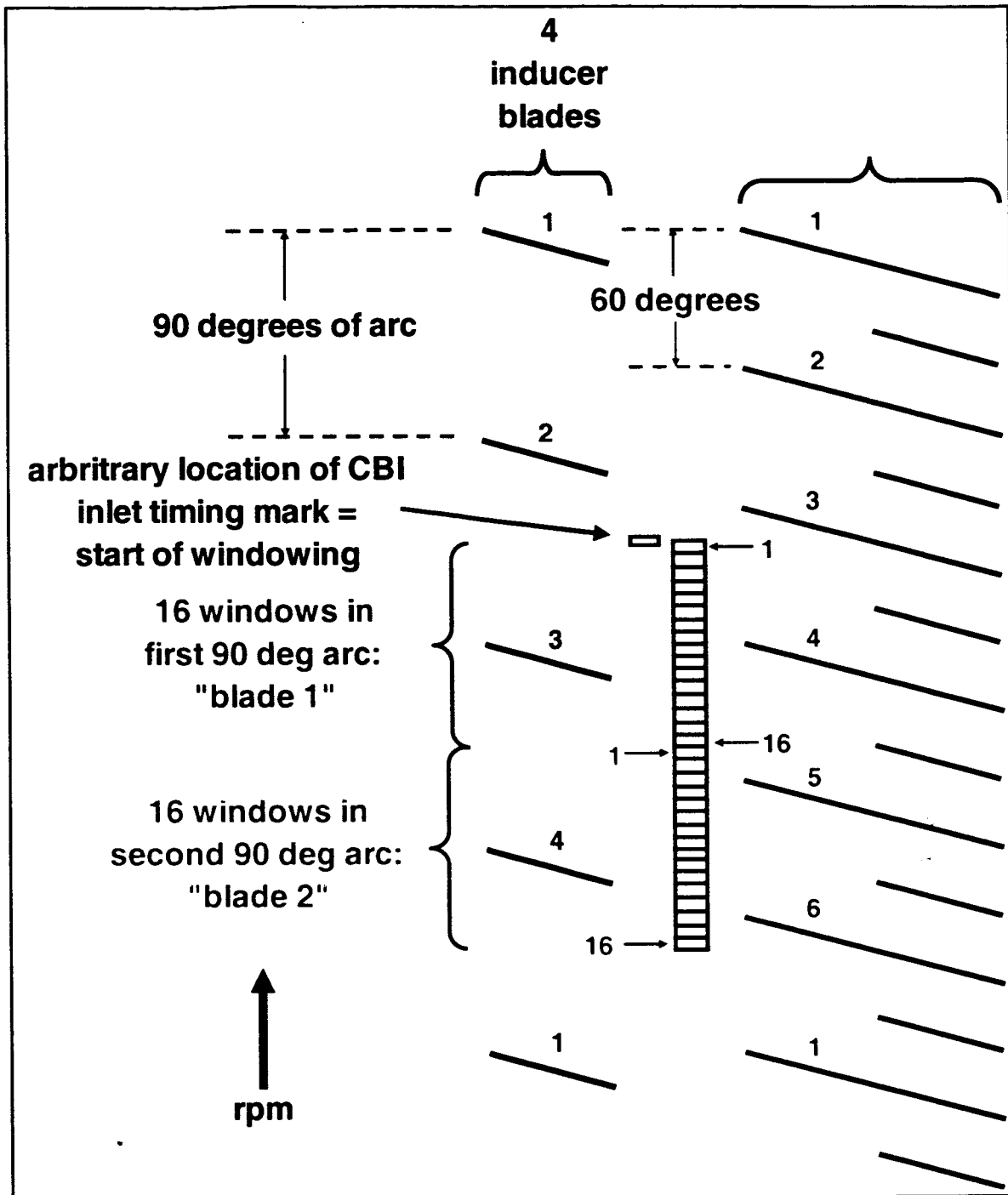
Figure 3. A schematic representation of how the multi-windowing concept was applied to the flow field measurement at the inlet to the CBI.
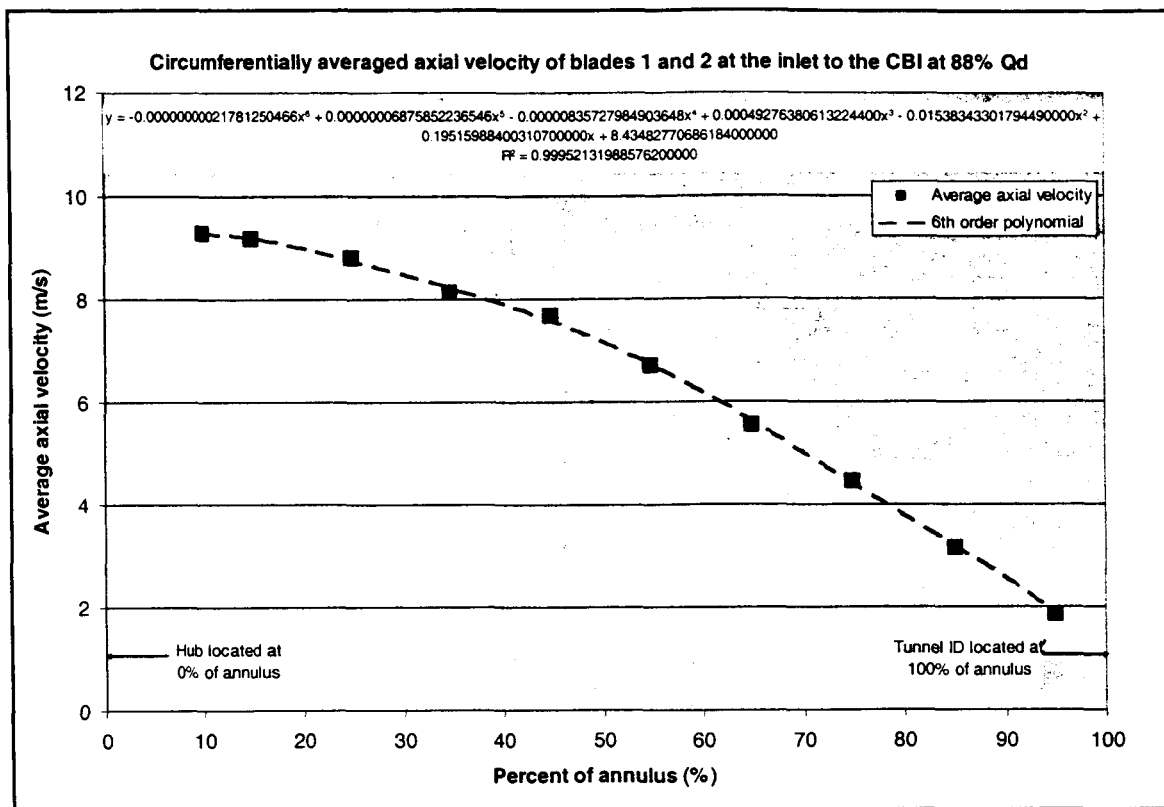
Figure 4. First method to calculate integrated flowrate used averaged axial velocities and non-zero velocities at the boundaries fitted by a 6th order polynomial curve.
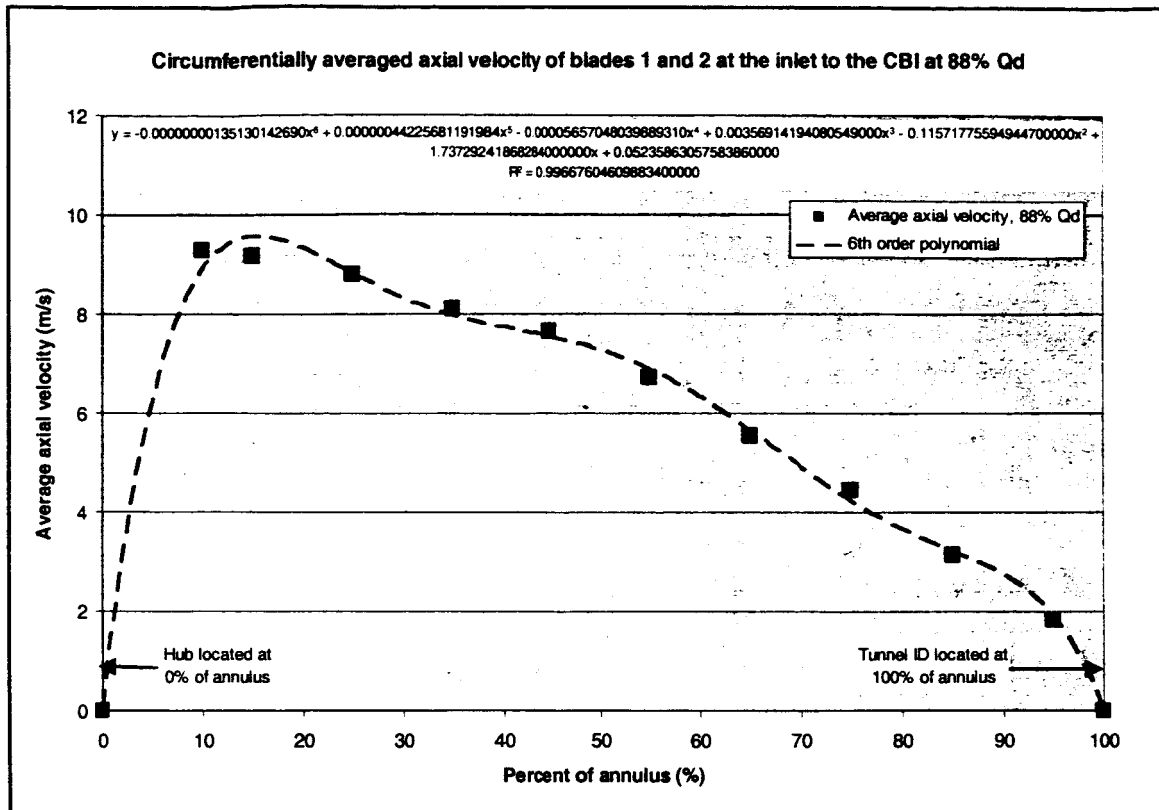
Figure 5. Modified method to calculate integrated flowrate used the same averaged axial velocities plus zero velocities at the boundaries fitted by a 6th order polynomial curve.
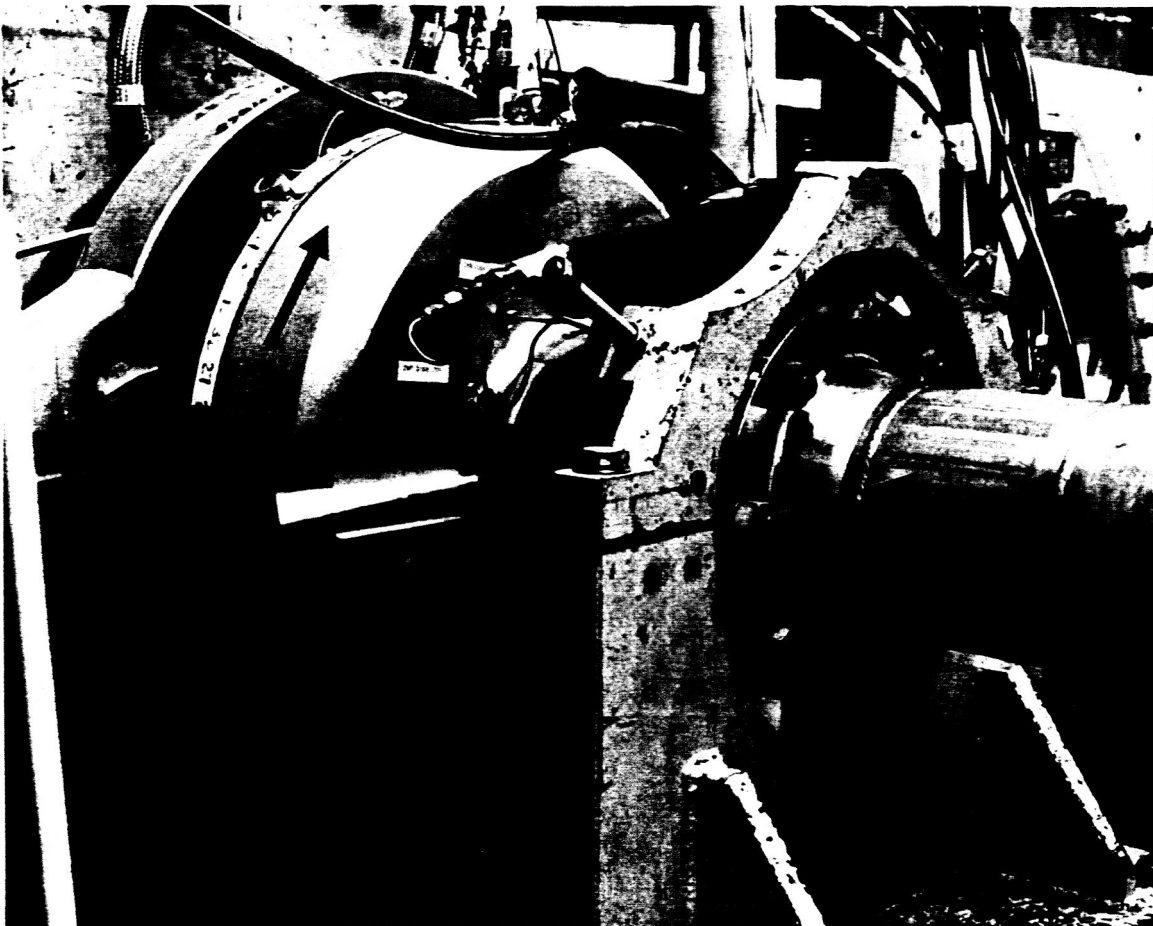
Figure 6. The 2D L2F laser velocimeter setup and aligned on the north side of the powerhead for the CBI inlet flow measurements; flow direction is indicated by the blue arrow while pump rotation is given by the red arrow.
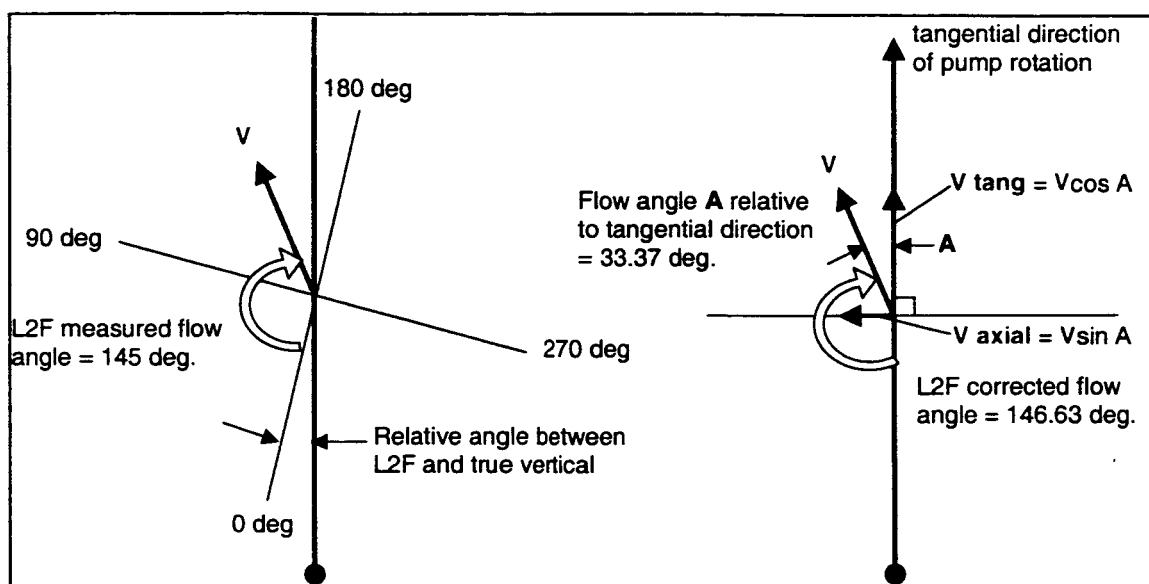
Figure 7. A schematic example of how the angle correction factors are used to relate the velocimeter reference frame to that of the tester.

angle correction used	88% Qd		100% Qd		120% Qd	
	Calculated flowrates as a % of the measured flowrates					
	non-zero wall velocity	zero wall velocity	non-zero wall velocity	zero wall velocity	non-zero wall velocity	zero wall velocity
nominal - 1 degree	92.3	88.4	93.9	89.7	95.6	91.1
nominal	97.4	93.3	97.7	93.4	97.8	93.3
nominal + 1 degree	102.5	98.2	101.5	97.1	100.1	95.4
variation	10.2	9.8	7.6	7.4	4.5	4.3

Table 1. Summary of calculations to determine the integrated flowrate with an included variation of +/- 1 degree in the angle correction factor.

Figure 8. Mis-alignment case in which the input laser beam (large green arrow) is displaced above the centerline of the pump.
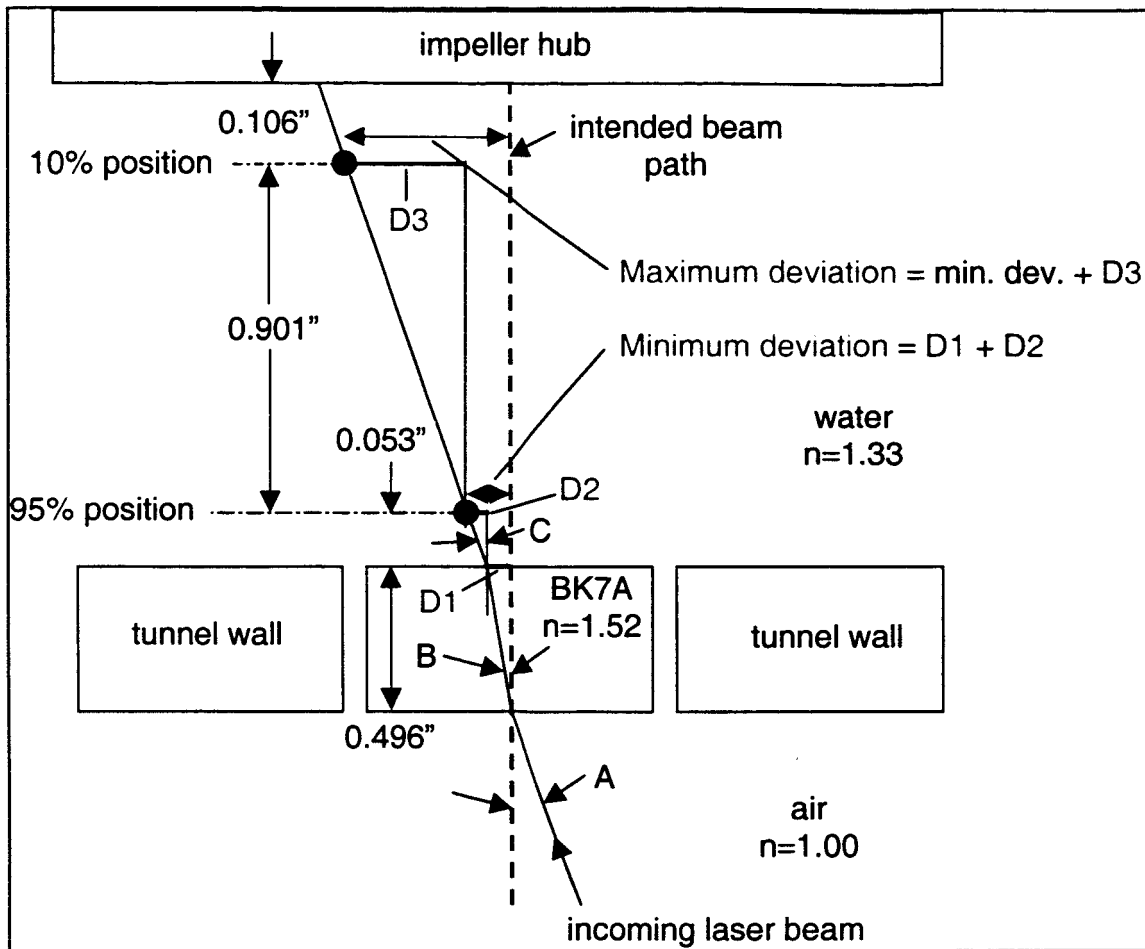
Figure 9. Mis-alignment case in which the input laser beam is oriented at an angle relative to the window and introduces a deviation in the intended beam path.
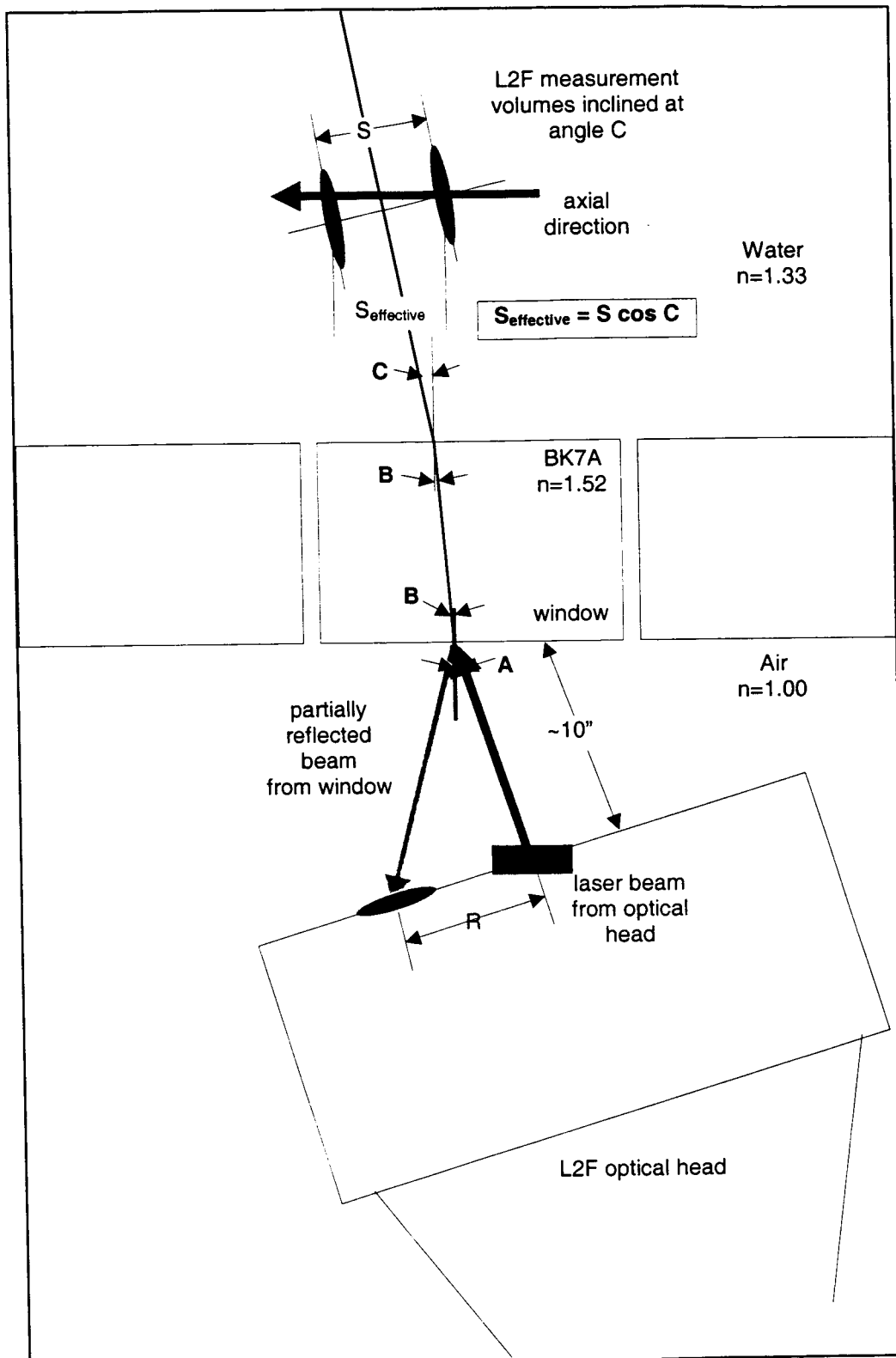
Figure 10. Mis-alignment case in which the input laser beam is oriented at an angle relative to the window and results in a decrease in the effective separation of the measurement volumes.

71

Appendix B

Concerning the continuity calculations for the CBI discharge survey

Background

During the process of constructing the consortium baseline impeller database, a larger than expected discrepancy was discovered in the calculated integrated flowrate using the velocimeter data acquired at the discharge of the impeller. Continuity calculations at several other velocimeter data planes in the tester, namely in the inlet pipe; upstream of the ADP inducer; downstream of the inducer and upstream of the impeller; had all initially yielded integrated flowrates within ~2% of the recorded flowrate from the facility flowmeters. Because the continuity calculations serve as a check on the data validity, these concerns lead to a thorough investigation of the situation at the impeller discharge. Ultimately, it also led to a re-investigation of the upstream CBI data as well, in which the uncertainty grew to about +/- 5%.

Results of using different methods to perform the flow integration calculations

The data collected at the discharge of the impeller was time phased to the rotation of the pump. A timing mark was machined into the shroud of the impeller directly over the point where a full blade attached to the shroud, as seen in figure 1. The passing of this mark was detected by the L2F measurement volumes and used to start the electronic windowing process. The purpose of the windowing was two-fold: first, to provide more detailed spatial resolution of the flow by sub-dividing the circumferential space between blades into smaller sub-sections and secondly, to separate the flow measurements acquired between the impeller full- to- partial blade region with that of the adjacent partial - to - full blade region. Keeping the flows separate permits a check on the flow split between the blades in order to determine if there were any gross mal-distributions of the flow between the impeller blades.

At the start of windowing, the 30 degree arc between the full blade and the adjacent partial blade was sub-divided into 16 smaller zones or windows, as seen in figure 2. In each of these windows, encompassing 1.875 degrees of arc or about 0.152" in arc length (at the first radial plane), total velocity and flow angle measurements were made. The L2F was operated so that data was collected only within this specified blade row, called "blade 1". Data from all other blade regions was skipped until the exact same "blade 1" region rotated into the field of the measurement volumes again. When sufficient data had been collected in the "blade 1" region, the process was repeated for the space occupied by the adjacent partial – to – full blade region, which was called "blade 2". The "blade 1" and "blade 2" data collection methodology was repeated at each of the ten or so points which spanned the radial plane at the discharge.

These points were spread out along the distance from near the inner window surface to the back wall, beyond the hub of the impeller, as seen in figure 3.

For the data post-processing the data from "blade 1" and "blade 2" were processed separately, up until a certain point whereupon all of the data was simply averaged together to give an overall view of the discharge flow. The entire data process is illustrated schematically in figure 4. In short, each "blade" flow angle data was corrected to make it relative to the reference frame of the impeller. Then the radial and tangential velocity components were calculated at each window. Next, the window data were circumferentially averaged so the data from all 16 windows was summed and divided by the number of windows. Finally, the circumferentially averaged data from "blade 1" and "blade 2" were themselves averaged together. This overall averaged data represents the broad general flow field without getting bogged down in too many details and was used to calculate the integrated flow rate.

In the investigation several different methods of integrating the velocimeter data were tried. In all of the cases, the data were from the first plane nominally located 0.125" beyond the OD of the impeller, as seen in figure 3. The general process common to all three methods was to plot the relevant radial velocity data, apply a 6th order polynomial curve fit to it, then use the curve fit equation to calculate the flow contribution in 0.1% increments across the flow region. The high values for the R-coefficient applicable to each polynomial (usually 0.99+) attests to the accuracy of the curve fits.

For the first method, all of the radial velocities at the impeller discharge, encompassing the region from the inner window to the back wall, were used to calculate the integrated flowrate, as seen in figure 5. The reasoning behind this approach was to look for a self-correcting solution: by including the negative radial velocities at the boundaries, a self-balancing solution might result in which the negative velocities would offset the calculated through-flow represented by the contributions of the positive radial velocities. The results, however, showed at 88% Qd, this method could account for only 78% of the measured flowrate, while the figure at 100% Qd was 61% and at 120% Qd the result was 105% of the expected value.

In the second method, the curve fit equation from the first case was used to calculate a velocity at the 0% and 100% B2 location. These values were plotted with data only from within the B2 region, generally located at about 13%, 25%, 38%, 50%, 63%, 75% and 88% of the B2 width. This process is shown in figure 6. The thought in this instance was to calculate the integrated flowrate by concentrating only on the B2 region, thereby negating the effects of the possibly recirculating flow outside the B2. These nine data points (7 within the B2, and the two endpoints using the prior curve fit equation) were plotted, fit with a 6th order polynomial and the equation numerically integrated in 0.1% increments, as before. The results, however, indicated at 88% Qd, this method would account

for 125% of the required flowrate, while the figure at 100% Qd was 111%, and at 120% Qd the result was 106% of the expected value.

In the third method, it was decided to impose a zero velocity on the 0% and 100% B2 locations (no-slip conditions) and then proceed in a manner similar to the second method, with plotting, curve fitting and numerical integration of the data, as seen in figure 7. The results using the third method were at 88% Qd, this method could account for 121% of the required flowrate, while the figure at 100% Qd was 109%, and at 120% Qd the result was 102% of the expected value. This became the baseline condition and probably represents the best interpretation of the data. The results of the three techniques are summarized in table 1.

An argument against imposing the zero velocity condition was the fact that the radial plane of the measurements was actually 0.125" downstream of the OD of the impeller. Consequently, there was not really a wall which required a zero velocity to be imposed. A different factor to consider might be an area reduction due to blockage by the impeller blades or blockage caused by fluid boundary layer buildup. But the boundary layer was considered to collapse immediately downstream of the bladed region of the hardware, and because the data plane was past the OD of the impeller, it might be argued that blade blockage was also not a factor.

Results of investigating "blunder" type of errors on the integrated flowrate calculations

a) Case where "A0" command might have been used and forgotten

Two other possible errors in the data processing scheme were investigated as well. The first case centered on the possible use of a velocimeter firmware command (called the "A0" command) which temporarily assigned the (then) current angular orientation of the beams as the zero degree reference position. All subsequent angle measurements are referenced to this temporary zero degree position.

Using the "A0" command is in contrast to the usual hardware method to find the zero angle. The zero angle is detected photo-electrically whereby the presence of a narrow slit in a disk attached to the mechanism responsible for rotating the optical heads is detected. In the handwritten notes from the alignment of the L2F, there is reference to using the "A0" command during the measurements to determine the angular offset between the zero angle position of the spots and true vertical represented by the wire plumb line (called the RABSATV angle). If the command were left active, then the data collected would have been referenced to an unknown zero angle position.

It should be pointed out that the normal procedure in acquiring L2F data is not to use any sort of momentary angle offset for the very reason that it might be forgotten about in later data processing. Instead, the RABSATV angle is measured, the data recorded and subsequently used in the post-processing. But the mention of use of the "A0" command during part of the alignment phase lead to suspicions that it might have inadvertently been left on, thereby corrupting the angle data references.

The flow continuity calculations were performed assuming the "A0" command was used and forgotten, but only for the first two integrations techniques; i.e., for the "wall-to-wall" case (technique #1) and for the B2 region only case with non-zero wall velocities (technique #2). The results, summarized in table 2, show continuity matches for technique #1 on the order of only 21% to 45% of the measured flow at the three recorded flow rates, while using technique #2 showed continuity matches in the 85% to 96% range for the same conditions. In light of larger than expected mismatch using the presumed more accurate technique #2, it was assumed that the "A0" command was probably not used during normal data recording.

b) Case where the sign of the RABSATV might be wrong, i.e., should be subtracted rather than added from raw L2F angle data

The second potential error in the data processing scheme concerned the sign of the RABSATV correction factor. Confusion in applying the RABSATV factor can arise in two ways. In the first instance, the receiving fiber optics can be attached to the photodetector unit in such a manner as to reverse the definition of the start and stop spots. The effect of this is to change the overall definition of the 0, 90, 180 and 270 degree orientations. The second instance arises from the use of a mirror to steer the beams through the window into the flow region. Mirrors flip their images left to right, but not up to down. This imparts another potential change in the overall definition of the principle directions on the L2F rotation after the beams have reflected from the mirror. Both of these potential error sources manifest themselves by the sign of the RABSATV correction factor.

To investigate the effect, the continuity calculations were re-run incorporating only a change in the sign of the RABSATV factor, from positive to negative. As was the case for the "A0" command investigation, only the first two integration techniques were used in this comparison. The results are summarized in table 3. The data in the table indicates the technique #1 results are completely un-realistic since they result in negative integrated flowrates. Likewise, the results of applying technique #2 are also suspect since the integrated flowrates all reside around 60%, which is a poor correlation. Consequently, it was assumed the sign of the RABSATV correction angle was correctly applied in the previous cases where the value is assumed positive rather than negative.

Factors which affect the uncertainty of the integrated flowrate calculations

As previously mentioned, the integrated flowrate calculation results discussed above were significantly worse than the previous continuity calculations at the other planes within the tester, so further calculations were performed in an effort to bracket the uncertainty in the results at the discharge of the impeller. To this end, the overall optical head alignment procedure and alignment data were analyzed. In a broad sense, there were two factors that influenced the corrections made to the raw velocimeter data. The first involved the determination of the radial plane of the data and the second involved the two angle correction factors used to convert the velocimeter frame of reference measurements into a frame relative to the impeller.

Starting with the more complicated frame of reference conversion issue, there were two factors which defined the total angle correction needed to make the frame of reference conversion. The first was a straight-forward measurement of the angle between the velocimeter measurement volumes and true vertical, represented by the shadow of a plumb line. The magnitude of this factor was a measure of the tilt of the optical head as a result of physically bolting it to the translation system and steel pedestal base. The 20 samples for this measurement had a mean value of 1.69 degrees, a maximum range of +/- 0.68 degrees, and a standard deviation of 0.23 degrees.

The second factor was a measure of the local tangent angle to the impeller at the plane of the measurements. This information was needed to convert the velocimeter data into the frame of reference of the impeller. The optical window opening at the discharge of the impeller was machined into the tester hardware. When the tester was assembled, the window should be at an angle of about 31 degrees below the horizontal centerline of the pump. In order to convert the velocimeter data into the impeller reference frame, it was necessary to precisely measure the actual angle at which data was collected. The window was large enough to allow a variation in the location of the data plane angle, i.e., 31 degrees plus or minus a couple of degrees, so the actual angle needed to be known. The angle was determined by monitoring and analyzing the reflected laser speckle pattern from different parts of the tester in order to assign a coordinate to that point. The laser speckle pattern was created when the velocimeter measurement volumes were precisely focused onto the surface in question. With coordinates from the optical head translation system assigned to the various points at which the laser beams had focused onto the tester hardware, it was possible to make calculations as to the angle at which the data was collected. This process is illustrated in figure 8.

To assess the uncertainty in the final angle calculation, a matrix of uncertainties was constructed. The matrix contained the maximum uncertainty in determining the coordinates of the various points of the tester hardware which go into the angle calculation. The values in the uncertainty of locating the shaft

vertical centerline, for example, were estimated to be +/- 0.010", etc. The value of the uncertainties were based upon both knowledge of error bounds from similar measurements in previous work as well as by analysis of the geometry of the setup and how that influenced the determination of the coordinate. For example, a part of the location uncertainty in determining the shaft vertical centerline (Y scl coordinate) depended upon speckling from the impeller hub. Prior experience indicated this type of alignment was accurate to within about +/- 0.004". Analyzing the geometry of the setup for this measurement showed that even if the point of reflection from the impeller hub was located 0.125" above the pump horizontal centerline (i.e., not measuring along a radius but rather along a chord), the error associated with this offset in determining the location of the impeller hub was only 0.005" (see figure 9). Therefore, in combination, the uncertainty in determining the shaft vertical centerline would be the speckle uncertainty (0.004") plus the possible additional error caused by geometry of the setup (0.005") plus another 0.001" for margin to yield 0.010".

By assigning relatively large (i.e., conservative) uncertainties to key hardware location coordinates determined via the speckle technique, it was possible to estimate the maximum variation in the overall determination of the local tangent angle. With all the ranges of the uncertainties in the data from the matrix) input to the angle calculation equation (seen in figure 10), the results showed the maximum range in calculating the local tangent angle was +/- 0.45 degrees. If the maximum range in the true vertical offset angle was +/- 0.68 degrees and the maximum range in the local tangent angle was +/-0.45 degrees, then overall the range for the angle correction factor was about +/- 1 degree.

In order to weigh the effects of a +/- 1 degree change in the total angle correction factor on the integrated flowrate, the third integration technique detailed above was used. This means only data within the B2 was used, along with imposing the no-slip, zero velocity at the wall condition for the 0% and 100% B2 points and then performing the curve fit and numerical integration. The results showed a +/- 1 degree change in the overall total angle correction factor would lead to a +/- 10% - 15% change in the integrated flowrate, as seen in table 4 and presented graphically in figure 11. This result basically comes about because the radial velocities are the product of the total velocity times the sine of the corrected flow angle. Because the angles were small, a small change in angle leads to relatively large changes in the radial velocity calculated, as seen in figure 12.

Effect of a change in radial location of the data plane on continuity calculations

In regards to the radial plane location, once the angle at which the data was collected was known, the optical head was moved in two directions in order to re-position the measurement volume along the radial line at the desired angle. It was relatively easy to determine the edge of the impeller with the speckle technique, and the uncertainty in doing so was typically on the order of 0.001" to

0.002". As for as bounds on the data location, since the first plane was nominally located 0.125" past the impeller OD, for calculation purposes it was assumed this position could be off by as much as +/- 0.100".

This meant the near point would actually be only 0.025" from the impeller OD, while the far point would be 0.225". It seemed unlikely the data stations would be off by more than this, otherwise the first data plane would be on the impeller shroud and the third plane (nominally R = 5.062", +0.100 results in 5.162") would be unattainable as the incoming laser light would be clipped by the edge of the window. This is the conclusion drawn by the analysis shown in figure 13.

To ascertain the effects on the integrated flow rate calculation with an "incorrect" radial position, the third integration technique (above) was used in which the data only within the B2 was used along with imposing the no-slip, zero velocity at the wall condition for the 0% and 100% B2 points and performing the curve fit and numerical integration. In the first instance, the radial location was changed from the nominal 4.647" to 4.547", or – 0.100" and the calculation performed. The second instance used a radial location of 4.747" or + 0.100". The results, summarized in table 5 and shown graphically in figure 14, showed the integration technique is relatively insensitive to the radial location of the data; the net offset of +/- 0.100" in radius resulted in only about +/- 2% in the calculated flowrate relative to the results for the nominal case with R = 4.647".

Summary

The key finding was that a +/- 1 degree variation in the overall angle correction factor used to convert the velocimeter data into the impeller frame of reference resulted in a +/- 10% – 15% change in the calculated integrated flowrate at the impeller discharge. Using the baseline method for calculating the flow out of the impeller B2 (utilizing the no-slip conditions at the boundaries), the results showed that at 88% Qd, this method could account for 121% of the required flow, while the figure at 100% Qd was 109% and at 120% Qd the result was 102% of the expected value. This means for example, at 88% Qd or 1065 gpm, the integration technique using the converted velocimeter data yielded 1288 gpm, or 121% of the real target value, etc. An analysis of a change in the radial location of the data plane by +/- 0.100" lead to only a +/- 2% change in integrated flowrate. Other possible error in the means of processing the data were studied and deemed to be unlikely contributors.

Recommendations

1. Better care should be taken to document the conditions used on the L2F data collection process. For example, digital camera photos of the connections of the fiber cables to the photodetector would document that facet. Additionally, photo documentation of the setup and results from the RABSATV would prove helpful, along with the use of a seeded jet past the mirror to confirm

angle conventions. It should be noted that during the time of the baseline impeller discharge measurements, there was no such thing as digital cameras. Film-based photos of the overall tester setup were all that were routinely taken after the test series was completed.

Figure 1. The timing mark at the discharge of the CBI was located to coincide with the trailing edge of a full blade at the shroud.

Figure 2. Schematic explaining the multi-windowing process at the discharge of the CBI.

81

Figure 3. An illustration (to scale) of the data station locations relative to the impeller discharge, the inner window surface and the back wall of the tester at the discharge of the CBI.

Example of data processing

QN : flowrate   RN : dataplane radius   BN : blade number   PN : position along radial plane   WN : window number V_n : total velocity in a window A_n : raw flow angle in a window

A'_n : adjusted flow angle in a window VR_n : radial velocity in a window VT_n : tangential velocity in a window   VRcN : circumferentially averaged radial velocity at given position   VTcN : circumferentially averaged tangential velocity at giv

VRcbbN : mean circumferentially averaged radial velocity from blades 1 and 2 at a position along the radial plane   A'cbbN : mean circumferentially averaged adjusted flow angle from blades 1 and 2 at a position along the radial plane

VTcbbN : mean circumferentially averaged tangential velocity from blades 1 and 2 at a position along the radial plane

same color = same QN, RN & BN

1,152 DATA POINTS

Angle adjustment factors (2) applied in order to format data relative to impeller reference frame:
$$A'_n = A_n + (RABSATV + Local\ tangent) - 360$$

1,152 DATA POINTS

4 inducer blades   6 full impeller blades   6 partial impeller blades

90 degrees of arc   60 degrees   30 degrees

Full blade   Partial blade   Full blade

flow   flow   timing mark   rpm

location of CBI discharge timing mark at full blade = start of windowing

Calculate circumferentially averaged total velocity :
$$VcN = \frac{\sum_1^{16} V_c}{16}$$
and circumferentially averaged adjusted flow angle:
$$A'cN = \frac{\sum_1^{16} A'_c}{16}$$

Calculate radial velocity component based on total velocity and adjusted flow angle:
$$VR_n = V_n \sin A'_n$$

Calculate tangential velocity component based on total velocity and adjusted flow angle:
$$VT_n = V_n \cos A'_n$$

72 DATA POINTS

1,152 DATA POINTS

1,152 DATA POINTS

Calculate mean circumferentially averaged total velocity from blade 1 and blade 2:

$VcbbN$, ($Vc1$ $Vc1$) 2 and,
$VcbbN$, ($Vc1$ $Vc1$) 2 etc.

& mean circumferentially averaged adjusted flow angle from blade 1 and blade 2:

$A'cbbN$, ($A'c1$ $A'c1$) 2 and,
$A'cbbN$, ($A'c1$ $A'c1$) 2 etc.

Calculate circumferentially averaged radial velocity :
$$VRcN = \frac{\sum_1^{16} VR_c}{16}$$
and circumferentially averaged adjusted flow angle:
$$A'cN = \frac{\sum_1^{16} A'_c}{16}$$

Calculate circumferentially averaged tangential velocity :
$$VTcN = \frac{\sum_1^{16} VT_c}{16}$$
and circumferentially averaged adjusted flow angle:
$$A'cN = \frac{\sum_1^{16} A'_c}{16}$$

36 DATA POINTS

72 DATA POINTS

72 DATA POINTS

Average radial velocity at plane 1 at discharge of CBI at 88% Qd

$y = -0.00000000007494843046x^6 + 0.0000000020931783333335x^5 - 0.00000181715659379243x^4 + 0.00002431091774984800x^3 + 0.00096779613100093200x^2 + 0.12739912259251600000x + 2.66811256967519000000$
$R^2 = 0.99745711012931900000$

Figure 5. The first integration method utilized all of the data from the inner window boundary (near -30%) to the far back wall of the tester (near +130%), a sort of "wall-to-wall" technique.

Average radial velocity at plane 1 at discharge of CBI in B2 region only

$y = -0.00000000085826924182x^6 + 0.0000002581497717652x^5 - 0.0002873951428283840x^4 + 0.001428710840940540000x^3 - 0.03170918373865560000x^2 + 0.38446161698766400000x + 2.6877447351050700000$

$R^2 = 0.99225023894843900000$

Figure 6. The second integration method used the curve fit from the first case to define (calculate) the velocities at the 0% and 100% boundaries of the B2, or in other words, a B2-only case with presumed (and calculated) non-zero wall velocities allowed.
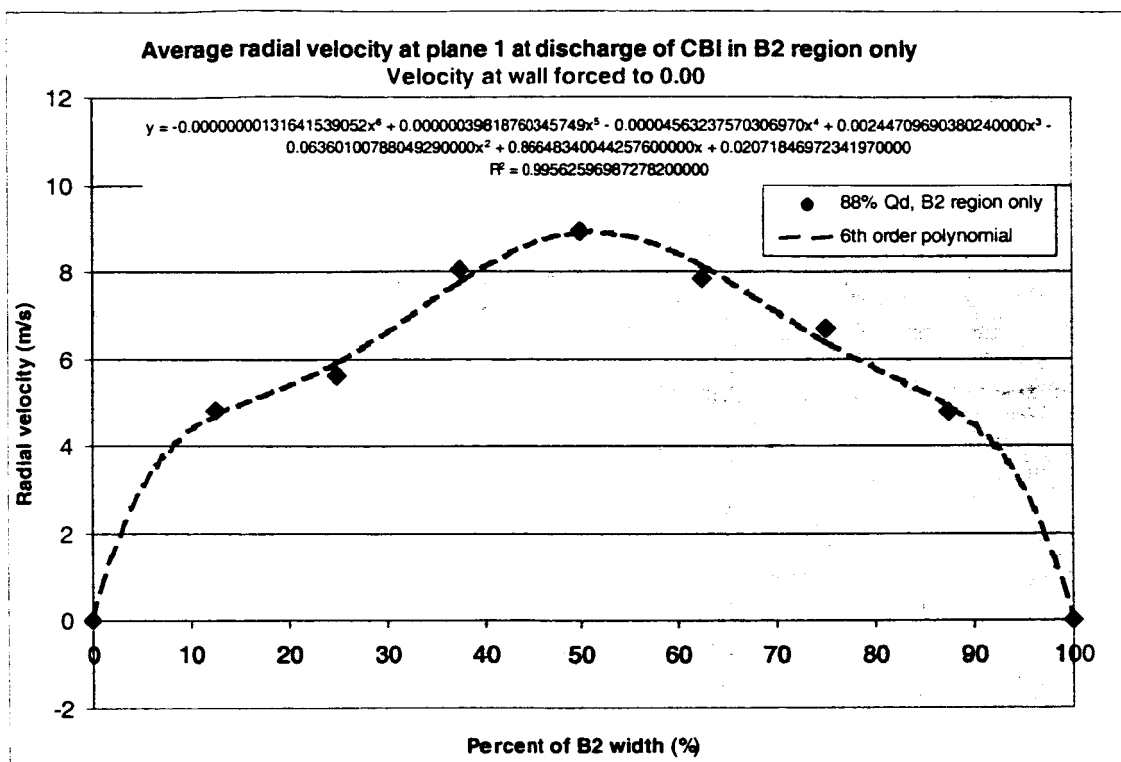
Figure 7. The third integration method forced the no-slip, zero velocity condition onto the data by including zero velocities at the 0% and 100% B2 locations before the polynomial curve fit was applied to the data.

Integration methodology applied	88% Qd	100% Qd	120% Qd
#1: all data at discharge plane 1 from window to wall used	77.9	61.4	104.9
#2: data only within impeller B2 used with calculated non-zero wall velocities	124.6	111.2	105.9
#3: data only within impeller B2 used with assumed zero wall velocities	120.9	108.6	102.3

Table 1. Summary results of the methods used to integrate flowrate where numbers in the table indicate the calculated flowrate as a percent of the measured flowrate e.g., method #1 for 88% Qd, where 77.9% means only 77.9% of the measured flow rate could be accounted for with this method.

"A0" command possibly in use plus this integration technique used	88% Qd	100% Qd	120% Qd
#1: all data at discharge plane 1 from window to wall used	32.7	21.1	45.3
#2: data only within impeller B2 used with calculated non-zero wall velocities	96.0	85.9	85.5
#3: data only within impeller B2 used with assumed zero wall velocities	n/a	n/a	n/a

Table 2. Results of the A0 analysis.

Wrong sign on RABSATV angle plus this integration technique used	88% Qd	100% Qd	120% Qd
#1: all data at discharge plane 1 from window to wall used	-12.6	-19.2	12.9
#2: data only within impeller B2 used with calculated non-zero wall velocities	67.4	60.6	64.9
#3: data only within impeller B2 used with assumed zero wall velocities	n/a	n/a	n/a

Table 3. Results of the RABSATV wrong sign analysis.
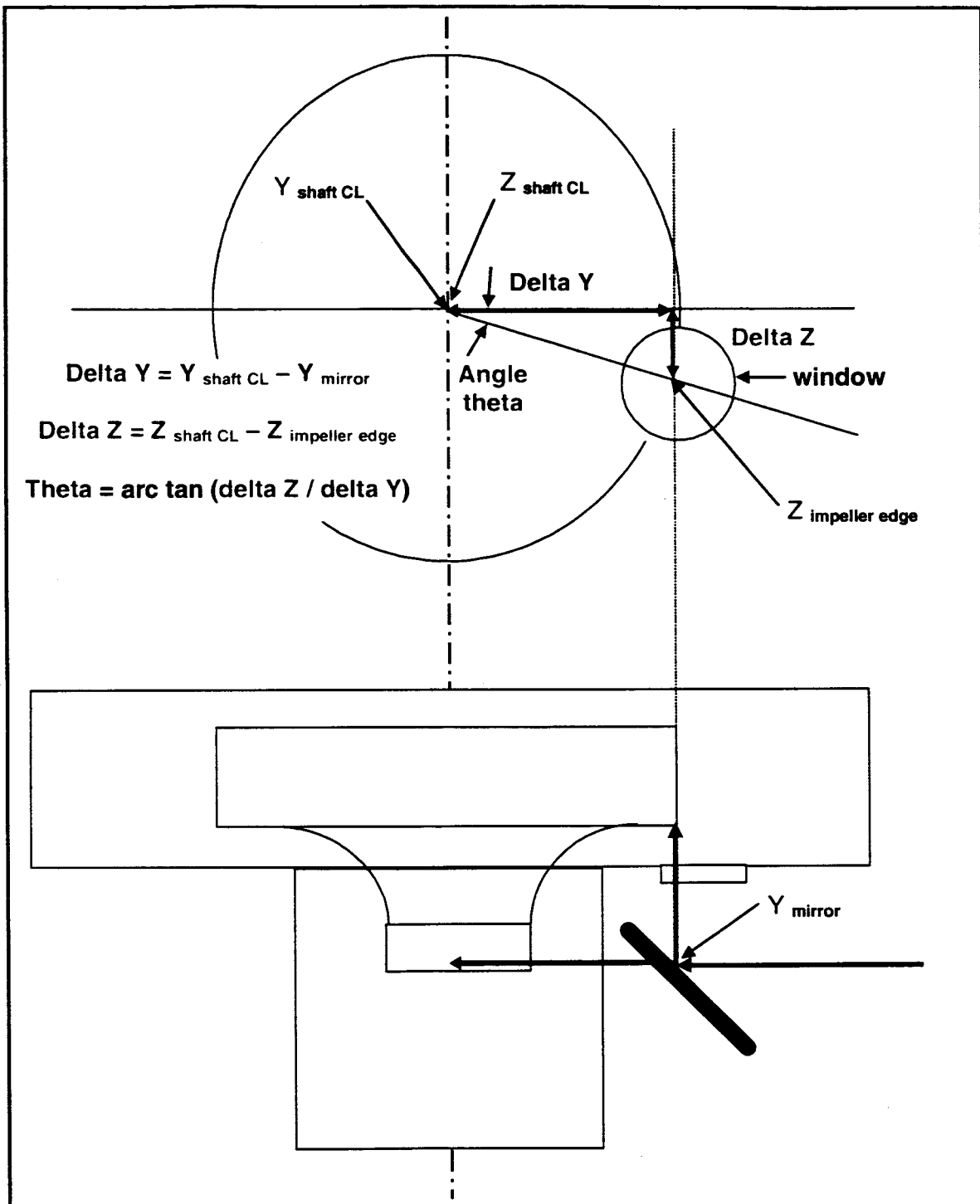
Figure 8. Illustration to show how the speckle alignment data leads to the ability to calculate the angle at which the data was collected at the impeller discharge window.

$$d = \frac{1}{2}\sqrt{4R^2 - C^2}$$

$$h = R - d$$

Effect of mis-alignment above the impeller centerline on determining the coordinate of the impeller hub
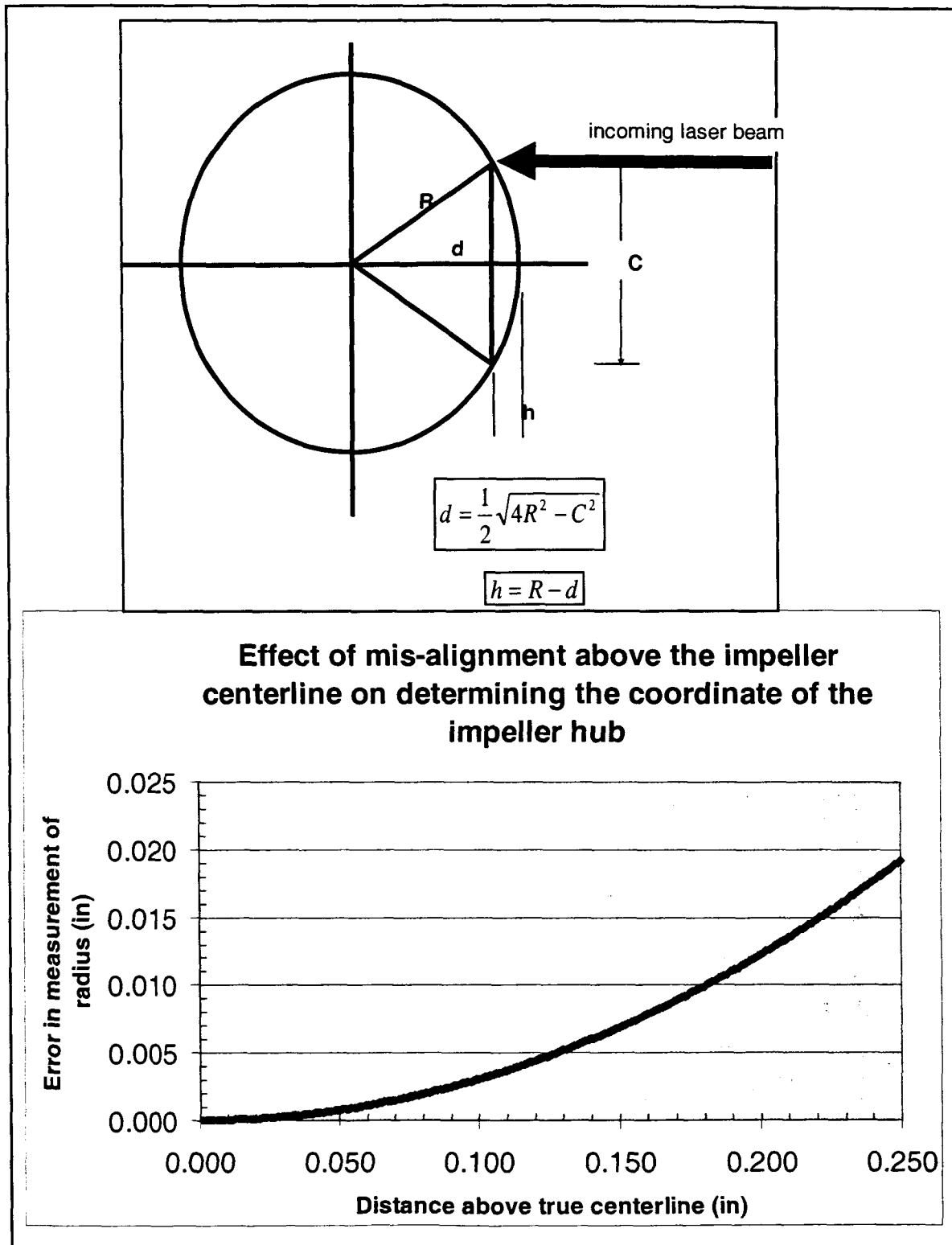
Figure 9. Illustrates that an attempt to inadvertently speckle from the impeller hub at a position above the pump horizontal centerline (above) introduces a very small error in determining the impeller radius (below), even for relatively large displacements above the centerline. The coordinate of the impeller hub is an input in the overall process of calculating the local tangent angle to the impeller.

89

An error analysis on the alignment of the velocimeter optical head relative to the CBI impeller

NOMINAL VALUES

Y mirror	72490	ULD
Y scl	23701	ULD
Z edge	192198	ULD
Z scl	162037	ULD

these are the Unidex coordinates where the indicated boundaries were determined by speckle reflection
ULD means Unidex Linear Digits, and 1.000" = 12,700 ULD but these coordinates are essentially arbritrary
as they only indicate the position of a boundary

ERROR BOUNDS

	(inch)	(ULD)
Y mirror	0.025	317.50
Y scl	0.010	127.00
Z edge	0.005	63.50
Z scl	0.015	190.50

these are estimates of the maximum error in determining the location of the indicated boundary
and are probably on the high side

$\tan(\theta) = (\,(Z\text{ edge} +/- \text{error}) - (Z\text{ scl} +/- \text{error})\,) / (\,(Y\text{mirror} +/- \text{error}) - (Y\text{ scl} +/- \text{error})\,) = (Z_1 - Z_2) / (Y_1 - Y_2) = \text{numerator} / \text{denominator}$

case #	Error bound in parameter coordinate				Z1 (ULD)	Z2 (ULD)	Y1 (ULD)	Y2 (ULD)	numerator (ULD)	denominator (ULD)	angle theta (deg)
	Z edge (ULD)	Z scl (ULD)	Y mirror (ULD)	Y scl (ULD)							
nominal	0	0	0	0	192198	162037	72490	23701	30161	48789	31.724
4P	64	191	318	127	192262	162228	72808	23828	30034	48980	31.516
3P 1N	64	191	318	-127	192262	162228	72808	23574	30034	49234	31.384
3P 1N	64	191	-318	127	192262	162228	72172	23828	30034	48344	31.851
3P 1N	64	-191	318	127	192262	161846	72808	23828	30416	48980	31.840
3P 1N	-64	191	318	127	192134	162228	72808	23828	29906	48980	31.407
2P 2N	64	191	-318	-127	192262	162228	72172	23574	30034	48598	31.716
2P 2N	64	-191	318	-127	192262	161846	72808	23574	30416	49234	31.707
2P 2N	-64	191	318	-127	192134	162228	72808	23574	29906	49234	31.276
2P 2N	64	-191	-318	127	192262	161846	72172	23828	30416	48344	32.176
2P 2N	-64	191	-318	127	192134	162228	72172	23828	29906	48344	31.741
1P 3N	64	-191	-318	-127	192262	161846	72172	23574	30416	48598	32.041
1P 3N	-64	191	-318	-127	192134	162228	72172	23574	29906	48598	31.607
1P 3N	-64	-191	318	-127	192134	161846	72808	23574	30288	49234	31.599
1P 3N	-64	-191	-318	127	192134	161846	72172	23828	30288	48344	32.068
4N	-64	-191	-318	-127	192134	161846	72172	23574	30288	48598	31.933

nominal row: +/- 0.45

min angle	31.276
max angle	32.176
delta angle	0.901

this is the matrix of maximum errors and how they
can be distributed in the equation i.e., sign

Figure 10. Calculations to determine the data plane angle (alpha) as a function of varying the maximum errors in the parameters used in the equation. The matrix of maximum errors uses the estimated maximum error bounds from above (associated with each part of the process of determining the angle) and distributes them in different combinations of either adding to the basic coordinate or subtracting from it.

Total angle correction used	88% Qd case: 1065 gpm expected	100% Qd case: 1210 gpm expected	120% Qd case: 1452 gpm expected
Nominal - 1.0°	136.7% : 1454 gpm calculated	122.5% : 1482 gpm calculated	113.6% : 1649 gpm calculated
Nominal	120.9% : 1287 gpm calculated	108.6% : 1314 gpm calculated	102.3% : 1485 gpm calculated
Nominal +1.0°	105.0% : 1118 gpm calculated	94.6% : 1145 gpm calculated	90.9% : 1320 gpm calculated

Table 4. Results showing how a +/- 1 degree change in the overall total angle correction factor used to process the data leads to a +/- 10% - 15% change in the overall calculated integrated flowrate (using technique #3).
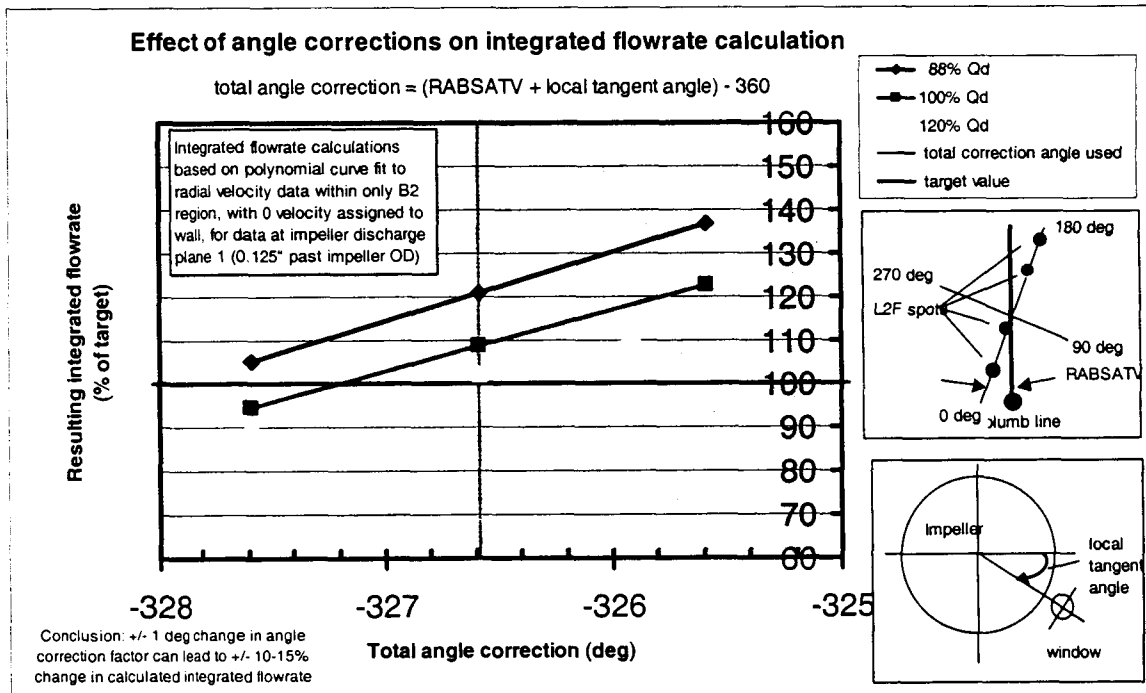
Figure 11. Graph depicts the data shown in table 1 and shows the effect of adding or subtracting 1 degree from the nominal angle correction on the integrated flowrate calculation assuming the integration is performed using technique #3.

91

Effect of small changes in total angle correction factor on the radial velocity
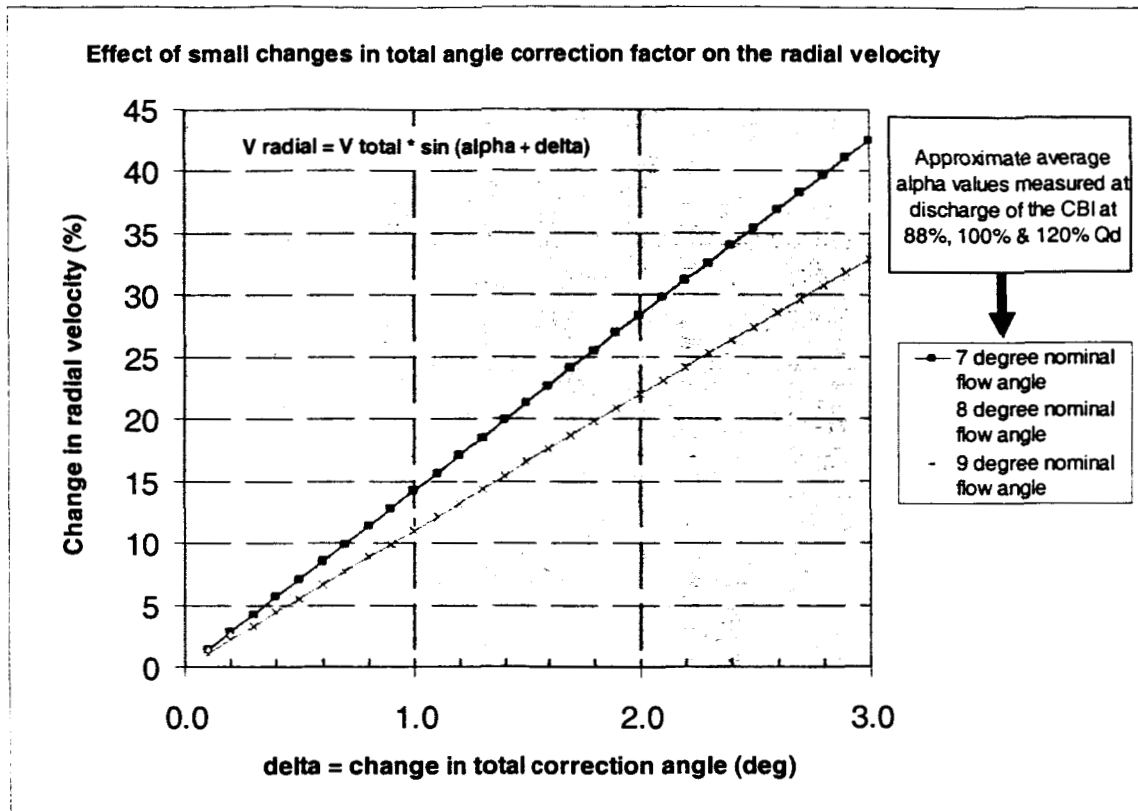
Figure 12. Effect of the change in the radial velocity as a result of a small change in the total angle correction factor for various small nominal flow angles observed at the discharge of the CBI. As noted, a +/- 1 degree change in the angle leads to a 10 – 15% change in the radial velocities, which in turn leads to a 10 -15% change in the integrated flowrates.
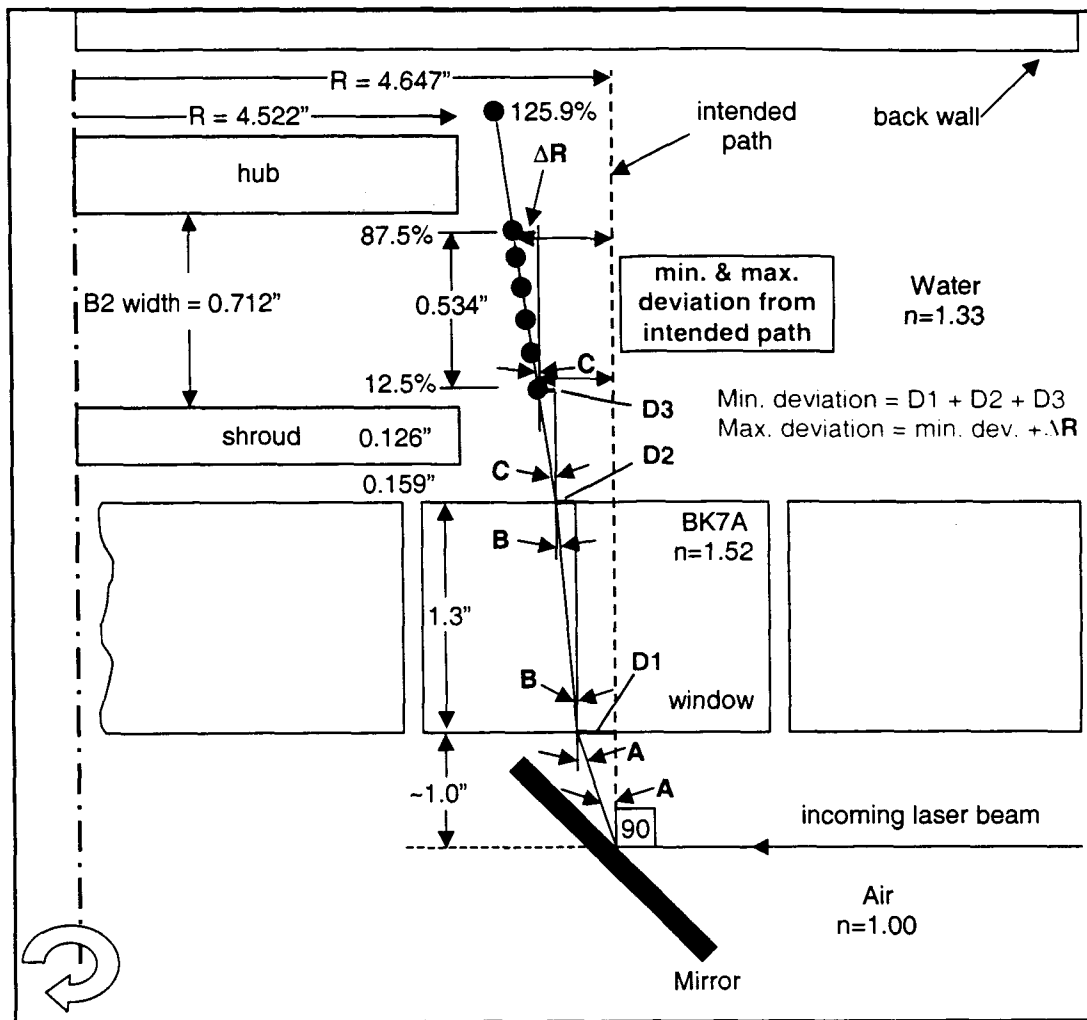
Figure 13. Illustration of the setup at the impeller discharge which could result if the mirror steered the input laser beams at an angle other than 90 degrees relative to the normal to the window. This setup was used to calculate the maximum deviation that would still allow the beam to focus at the 125% location where we know data was successfully acquired, seen in the table below. This maximum deviation would put the data station at a radius other than the intended. In that maximum deviation case, the 12.5% data station would have been off the intended radius by 0.093" while the 87.5% data station would have been off by 0.111". So, for analyzing the effect of acquiring data at other than the intended radius, the locations were chosen as +/- 0.100".

angle A (deg)	n1	n2	n3	angle B (deg)	angle C (deg)	D1 (in)	D2 (in)	D3 (in)	min. dev. (in)	delta R (in)	max. dev. (in)	delta R2 (in)	125.9% point location (in)	possible (Y/N)
5.00	1.00	1.52	1.33	3.29	3.76	0.087	0.075	0.025	0.187	0.035	0.222	0.059	4.401	N
4.50	1.00	1.52	1.33	2.96	3.38	0.079	0.067	0.022	0.168	0.032	0.200	0.053	4.426	N
4.00	1.00	1.52	1.33	2.63	3.01	0.070	0.060	0.020	0.149	0.028	0.177	0.047	4.451	N
3.50	1.00	1.52	1.33	2.30	2.63	0.061	0.052	0.017	0.131	0.025	0.155	0.041	4.475	N
3.00	1.00	1.52	1.33	1.97	2.26	0.052	0.045	0.015	0.112	0.021	0.133	0.035	4.500	N
2.50	1.00	1.52	1.33	1.64	1.88	0.044	0.037	0.012	0.093	0.018	0.111	0.029	4.524	Y
2.00	1.00	1.52	1.33	1.32	1.50	0.035	0.030	0.010	0.075	0.014	0.089	0.024	4.549	Y
1.50	1.00	1.52	1.33	0.99	1.13	0.026	0.022	0.007	0.056	0.011	0.066	0.018	4.573	Y
1.00	1.00	1.52	1.33	0.66	0.75	0.017	0.015	0.005	0.037	0.007	0.044	0.012	4.598	Y
0.50	1.00	1.52	1.33	0.33	0.38	0.009	0.007	0.002	0.019	0.004	0.022	0.006	4.622	Y
0.00	1.00	1.52	1.33	0.00	0.00	0.000	0.000	0.000	0.000	0.000	0.000	0.000	4.647	Y

radial location		Integrated flowrate using polynomial curve fit in the B2 region only with 0 wall velocity (technique #3)		
		Target flowrate (% of Qd)		
	(in)	88%	100%	120%
r - 0.100"	4.547	118.3	106.3	100.1
nominal	4.647	120.9	108.6	102.3
r + 0.100"	4.747	123.5	110.9	104.5

Table 5. Results of continuity calculations to determine the effect of moving the data plane closer to, and further from, the intended data plane location at a radial plane where R = 4.647 inches, which is 0.125" past the impeller OD.
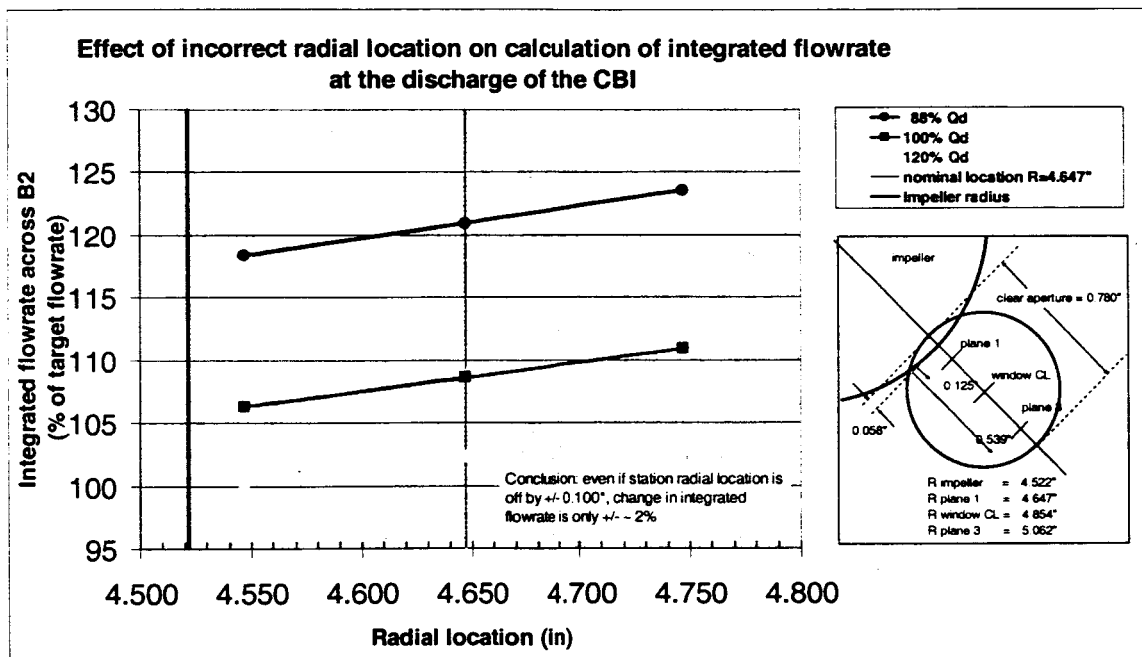
Figure 14. The effect of calculating the integrated flowrate with a +/- 0.100" change in the radial position of the data plane, based on data given in table 5.

Appendix C

SSME HPFTP impeller
database

CBI database

COI database

VID pressure
database

Appendix D

CBI inlet continuity iterations

CBI discharge continuity iterations no slip conditions

CBI discharge continuity iterations nonzero wall conditions

CBI discharge continuity iterations RABSATV changes

Task 4b: CFD code validation
and
Task 5a: Development of concepts for wide flow range turbopump

This section of the final report covers Task 4b and Task 5 of the NRA8-21 Cycle 2 RBCC Turbopump Risk Reduction contract.

The primary objective of Task 4b was to validate the Enigma Computational Fluid Dynamics (CFD) code for pump diffuser analyses and apply the code to wide-flow-range (WFR) diffuser designs. The consortium high-head pump configuration was selected as the candidate validation case for Task 4b.

The primary objective of Task 5 was to perform steady and unsteady analyses on some wide flow range diffuser concepts. Two WFR concepts were examined: 1) the composite vane diffuser (vane-island type), and, 2) the constant thickness thin vane diffuser.

Introduction

Computational fluid dynamics can be used as the diffuser design and analysis tool for evaluating new diffuser concepts for the Deep Throttling Turbopump Task. The purpose of the current effort is to anchor the Enigma Navier-Stokes code with experimental diffuser data and to apply the Enigma CFD analysis to WFR diffuser concepts. CFD validation and analysis cases for several diffuser configurations are presented and discussed. The appendix contains the complete text of the WFR diffuser concept paper presented at the JANNAF Dec 2003 conference.

Numerical Method for Diffuser Design

The basic 3-D Navier-Stokes numerical algorithm is described in Williams.[1,2] This finite-difference algorithm is implemented in the Enigma CFD code and features the Helmholtz pressure method to enforce the fluid zero-divergence condition. The unsteady algorithm utilizes time-implicit, second-order time differencing and dual time-stepping with sub-iterations to converge the nonlinear equations at each time step. Grid node velocities are included in the convection terms to account for moving meshes. The numerical method uses the standard k-$\square$ turbulence model with wall functions. The 2003 version of the EnigmaCFD code used for the rotating machinery calculations presented in this report is a single processor code. A rotating machinery multi-processor EnigmaCFD version should be available in the February/March 2004 time-frame.

Analysis Method Validation for Diffusers

Three diffuser configurations are utilized to anchor/validate the CFD code. These configurations are:

1) A 2-D diffuser
2) The consortium vane-island diffuser with thirteen vanes, and
3) The consortium pump stage with inducer, impeller, diffuser, and collector

Steady 2-D Diffuser Calculations

Muggli et al.[3] presented the results of a comparison between experimental data and predictions from a commercial CFD code for a 2-D diffuser at different diffuser angles. Five cases from Muggli were repeated using the current methodology.

The flow geometry and a typical flow mesh is shown in figure 1. A flow mesh of 109x33 nodes was used for the calculations. The Reynolds number is 1.2×10^5 and the inlet flow conditions correspond to thin inlet boundary-layers (zero-thickness for the current simulation).

The static pressure recovery results are shown in figure 2. The pressure coefficient is defined as $C_p = \Box p / (0.5 \Box V^2_{in})$. For diffuser angles at or below 12 degrees, the current results show good agreement with the experimental data and with a commercial code. However, neither code could predict the diffuser angle at which stall occurs or the magnitude of the stall. Muggli et al.[3] attributes the optimistic pressure recovery prediction to the under-estimation of the separated flow blockage by the standard k-$\Box$ turbulence model.

If the pump stall phenomena is the same as the 2-D diffuser stall exhibited by this case, then this validation case would indicate that the current industrial numerical technology would not be able to predict pump stall trend.

Pump Design Point

The remainder of the validation cases are for the consortium high head pump stage (figure 3) which incorporates a vane-island diffuser with 13 vanes.

The pump is required to raise the inlet pressure by 1100 feet and deliver 1210 GPM of water at 6322 RPM. The specific speed is equal to 1100. The baseline pump configuration is the single stage consortium high head impeller.[4]

Steady-State Vane-Island Diffuser Calculations

The consortium vane-island diffuser was simulated using a single periodic channel and uniform inflow conditions. The purpose of this type of calculation is

to ascertain whether the experimentally observed stall can be explained by a decoupled, diffuser alone calculation. Also, this simple configuration can be used to understand grid resolution requirements.

The flow geometry and typical flow mesh is shown in figure 4. A grid resolution study was performed for diffuser grids with 8,888; 48,887; and 186,480 nodes. In addition, two different convection upwinding schemes were examined: a third-order upwind based scheme, and a monotonic central-difference based scheme.

Figure 5 shows the effect of grid size on the head coefficient for design flow conditions. The head coefficient ($\square$) is defined as:

$$\psi = \Delta H /(U_{tip}^{2} / g)$$

. !

where $\square$H is the static pressure head rise, U_{tip} is the impeller tip speed (249.5fps), and g is the acceleration due to gravity. For this single channel diffuser model, the monotonic central difference scheme provides more uniform accuracy across a range of grid sizes. In general, calculations based on the third-order upwind based scheme are more robust. A baseline flow mesh consisting of 48,887 nodes was used for the head-versus-capacity calculations. Uniform inflow conditions were used for the calculations.

Figure 6 shows the computed velocity and static pressure contours for the design flow case. The static pressure head coefficient variation with flow is shown in figure 7. The head coefficient is based on the impeller tip speed which is 249.5 ft/s. The calculated performance is reported from the inlet to the discharge of the model. It is not surprising that the numerical predictions do not match the experimental data since the computations utilized uniform inlet conditions and do not include the non-uniform flow effects caused by the impeller.

The current third-order upwind based computation does a reasonable job of matching the commercial code even though the commercial code used approximately 3 times more grid points. The current monotonic central-difference based computation does a better job of indicating where the head fall-off begins.

Neither computation captures the magnitude of the head fall-off which suggests that the phenomena (e.g., perhaps it is rotating stall) can not be captured with a single periodic channel/uniform inlet model or that the k-$\square$ turbulence model is deficient for off-design flow calculations. The frozen-rotor and unsteady pump simulations will give further insight into this.

Frozen-Rotor Pump Stage Calculations

A quasi-steady stage simulator was constructing utilizing finite-difference models for the inducer, impeller, diffuser and collector. The test facility collector was modeled as a radial volute. All flow channels were modeled. The experimental test rig inducer/impeller clocking was maintained in the numerical models. The relative clocking of the diffuser to the impeller was arbitrary for the numerical model.

Flow meshes were constructed for each component with overlap mesh regions for coupling the individual models. A coarse mesh of about 573,000 nodes was used for the current simulations. The flow geometry is shown in figure 8.

In the typical frozen rotor method, inertial forces caused by the unsteady flow terms are neglected and the flow is steady in the relative reference frames of the rotating and stationary components. The rotor-stator interaction is calculated by a steady coupling at their interface. The frozen rotor method can be used to calculate the psuedo-time evolution of the forces and flow by repeating the rotor/stator calculations for different angular positions of the rotor. This type of approximation is usually not accurate for real unsteady phenomena - a full unsteady method is needed to capture the true rotor-stator interaction and is discussed in the next section.

However, the frozen-rotor method can be used for quick design calculations and to provide initial conditions for full unsteady calculations.

For the consortium pump stage, the frozen-rotor method is used for the steady-state (in the relative frame) calculation of the stage flow at one clocking of the impeller/diffuser. This type of calculation serves as an initial condition for the full unsteady calculations presented in the next section. In addition, the mechanism of rotating stall is illustrated with this type of calculation.

Six cases were computed for 0.5, 0.6, 0.7, 0.9, 1.0, and 1.1 times the design flow (1210 gpm). These calculations utilized the monotonic central differencing scheme for the diffuser. The computed velocity magnitude contours are shown in figure 9. Sample pressure contours are shown in figure 10.

The velocity magnitude contours indicate that rotating stall can be initiated by a flow resistance/manifold effect, i.e., local impeller discharge-to-diffuser throat turning losses and shear losses cause the flow to favor one channel over another. Unsteady forces and time phasing would then work in conjunction with the time-varying losses to propagate the stall cell.

The predicted diffuser head performance is shown in figure 11. The head coefficient ($\square = \square H/U^2_{tip}/g$) is based on the static pressure rise and the impeller tip

velocity, U_{tip}=249.5 ft/s. The head coefficient drops by about 0.05 when the flow goes from 80% to 60% of the design flow. This is consistent with the experimental data. This indicates that this type of calculation can be used to determine the stall behavior of the new wide-flow-range concepts. As the grid resolution study indicated, a better match between the actual and predicted performance levels can be obtained by using a finer mesh.

The effect of the proximity of the modeled collector to the diffuser was examined by increasing the diffuser-volute distance by nearly 2 inches (figure12). Figure 13 shows the computed velocity magnitudes for the non-extended and extended models. The change in predicted diffuser static head rise was small (figure14) so the initial diffuser-collector spacing was maintained for subsequent calculations. However, the size of the volute and its impact on the diffuser pressure rise remains to be studied.

The shape of experimentally measured diffuser head-capacity curve is very similar to that measured by Kurokawa.[45] The dynamic measurements of Kurokawa indicated that the stall exhibited rotating stall characteristics. This is consistent with the pattern being shown in the frozen-rotor type calculations.

Detailed Comparisons with Experimental Data and Fine Grid CFD Calculation

The computed impeller discharge radial and velocity distributions are compared to the experimental data in figures 15-17. Figure 15 indicates the location of the numerical model plane used for the comparisons.

The computed impeller static pressure rise head is compared to the experimental data in figures 18-19. Figure 18 indicates the location of static pressure head rise planes used for the comparison. The inlet static pressure was assumed to be 50 psi.

The calculated diffuser shroud static pressure is compared with experimental data in figure 20. This figure also includes some unsteady results from the next section of this report. The predictions are consistent with the experimental trend. The predicted throat/channel pressure magnitudes are consistent with the grid resolution study that indicated that the coarse flow model under-predicts the head rise.

Comparisons with fine grid results from the Phantom CFD code are shown in figures 21-24. The overall trends for the impeller discharge velocities and static pressure rise are similar between codes and mesh resolutions (Coarse grid-Enigma; Fine grid-Phantom). Both codes and models are able to predict the diffuser stall trend.

Unsteady Pump Stage Calculations

The unsteady pump stage simulator is a fully unsteady model with moving/sliding meshes and retention of the unsteady terms in the Navier-Stokes equations.

Unsteady calculations have been performed for six different flows – 0.5, 0.6, 0.7, 0.9, 1.0, and 1.1 times the design flow. The coarse grid model used for the frozen-rotor calculations was also used for the unsteady calculations. The inducer and impeller are rotating and the diffuser and volute are stationary with sliding meshes between the impeller and diffuser. Frozen-rotor solutions were used as initial conditions for the unsteady calculations.

Figure 25 shows the effect of different time-resolutions (time-step size) on the calculated unsteady static pressure. The 3371 Hz resolution case shows that the flow appears to achieve time-periodicity within two revolutions for the design flow case (the shaft speed is 105.4 Hz). Higher time/frequency resolutions more accurately capture the magnitude of the rotor-stator interaction.

Figures 26 through 31 show sample calculated pressures traces for the same location indicated in Fig. 25. The calculations were made with 75,847 Hz resolution. The off-design cases in the stall regime (605, 726, and 839 gpm) show non-periodic behavior for at least 3 revolutions (Figs. 26-28). It appears that sub-synchronous flow effects would require more lengthy calculations to capture the low-frequency periodicity. The flow cases for the non-stall regime (1089, 1210, and 1331 gpm) readily achieve time-periodicity (figures 29-31). Figures 32-37 show computed power spectral densities. The spectra show the presence of 6N and 12N harmonics and N is the rotation speed 105.4 Hz. Near synchronous and sub-synchronous harmonics for the deep stall cases may be indicative of low harmonics that can only be resolved by continuing the time integration for many more revolutions.

Composite Vane Diffuser

The traditional diffuser design methodology optimizes the diffuser performance at a single flow point – each flow channel has the same blade shape and channel throat area. In principle, the composite vane diffuser achieves wide-flow range by using a summation of channels that are optimized for different flow points. The concept is developed as a perturbation of the baseline vane-island diffuser, i.e., the same number of blades and overall dimensions are retained. See Gunizburg and Williams[6] or the Appendix for a detailed discussion of the composite vane diffuser design philosophy.

For example, the CompV5 diffuser for wide-flow range utilizes eleven blades with a leading edge blade angle of 6 degrees and two blades with a leading edge

blade angle of 12 degrees (figure 38). The CompV10 diffuser utilizes 6 blades with 6 degrees and 7 blades with 12 degrees.

The composite vane simulator utilizes the components in the consortium pump stage simulator except the traditional diffuser was snapped-out of the simulator and the composite diffuser was snapped-in. Figures 39 and 40 show the computed pressure and velocity magnitude for the CompV10 system at 839 gpm, respectively. Note the 839 gpm flow point is where the consortium diffuser was fully stalled.

The mass flow distribution through the diffuser channels for the traditional consortium diffuser and the composite vane diffuser is shown in figures 41 and 42 for the design flow point. Figure 42 shows how the composite vane diffuser varies the channel mass flow distribution to achieve wide flow range. Figure 43 shows how the composite vane diffuser extends the operating range compared to the traditional diffuser design.

Unsteady calculations with 37,924 Hz resolution were performed for the 839 gpm and 1210 gpm cases. Figures 44 and 45 show the computed pressure time-histories for the 1210 gpm flow point for both the consortium and CompV10 diffuser, respectively. Figure 46 shows the CompV10 pressure time history for the 839 gpm flow point. Power spectral densities for the two CompV10 unsteady cases are shown in figures 47 and 48.

Thin Vane Constant Thickness Diffuser

One of the design aspects of the thin vane constant thickness wide flow range diffuser is fewer low-angle diffuser blades that wrap around a lot. In addition, the thin vane diffuser concept achieves wide-flow range by using a judicious radial placement of the diffuser in terms of the Gap A and B defined below.

The vaned diffuser must accommodate pressure pulsations from the impeller by judicious choice of certain geometric attributes. These are the Gap B, which is the clearance between the impeller blades and the diffuser blades as well as the Gap A, which is the clearance between the impeller shrouds and diffuser shrouds.

See Gunizburg and Williams[6] or the Appendix for a detailed discussion of the composite vane diffuser design philosophy.

The thin vane diffuser simulator utilizes the components in the consortium pump stage simulator except the traditional diffuser was snapped-out of the simulator and the thin vane diffuser was snapped-in. Also, the impeller had to be modified (see figure 49) to accommodate the Gap A and Gap B design guidelines. Figure 50 show the computed velocity magnitude and pressure for

the thin vane diffuser system at the 1210 gpm point. The predicted thin vane diffuser performance is shown in Figure 51.

Conclusions

In summary, it was found that:

1) Commercial level codes with standard k-□ turbulence models cannot accurately predict 2-D diffuser stall trends
2) The Enigma CFD code and Phantom CFD code were able to predict the stall trend for the consortium high-head pump
3) The calculated velocity magnitude contours indicate that rotating stall can be initiated by a flow resistance/manifold effect, i.e., local impeller discharge-to-diffuser throat turning losses and shear losses cause the flow to favor one channel over another
4) The composite-vane diffuser was successful in extending the stall-free range of the diffuser.

Grid resolution studies for a single diffuser channel indicate that the overall head-rise predictions can be improved by increasing the number of flow nodes for the pump stage simulation. Also, based on the results of this contract, it appears that general diffuser off-design analyses should incorporate, at a minimum, the coupled impeller and diffuser.

References

1.Williams, M., "A Helmholtz Pressure Equation Method for the Calculation of Unsteady Incompressible Viscous Flows," Int. J. Numer. Meth. Fluids, Vol. 14, 1992, pp. 1-12.

2.Williams, M., Chen, W., Brozowski, L., and Eastland, A., "Three-Dimensional Finite Difference Method for Rotordynamic Fluid Forces on Seals", AIAA J., Vol. 35, No.8, 1997, pp. 1417-1420.

3.Muggli, F.A., Eisele, K., Casey, M.V., Gulich, J., Schachenmann, A., "Flow Analysis in a Pump Diffuser – Part 2: Validation and Limitations of CFD for Diffuser Flows," ASME J. Fluids Eng., Vol. 119, Dec 1997, pp978- 984.

4.Ferguson, T. V., Guinzburg, A., McGylnn, R. D., and Brozowski, L. A., "Laser Velocimeter Measurements of the Flow within a Vane-Island Diffuser," Paper FEDSM99-6985, Proceedings of 3rd ASME/JSME Joint Fluids Engineering Conference, July 18-23, 1999, San Francisco, California.

5.Kurokawa,J.,Saha,S.L.,Matsui,J.,and Kitahoa, T., 2000,"Passive Control of Rotating Stall in a Parallel-Wall Vaneless Diffuser By Radial Grooves," ASME J. Fluids Eng., 122, Mar., pp. 90-97

6.Guinzburg,A. and Williams, Morgan, "Advanced Deep Throttling Pump Diffuser Concept Development", JANNAF Conference, Colorado Springs, CO, December 2003.
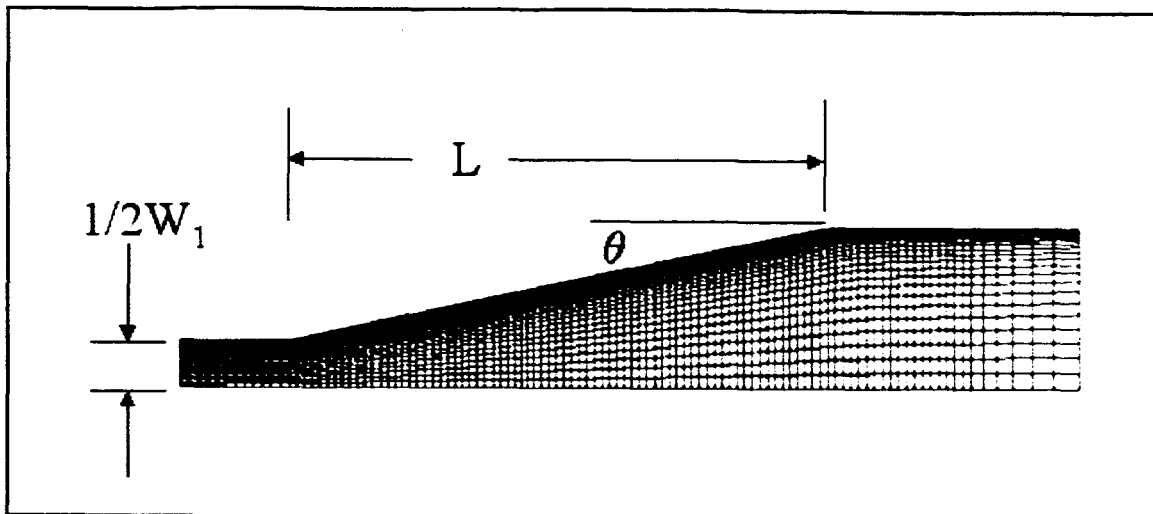
Figure 1. 2-D diffuser geometry (symmetric half).
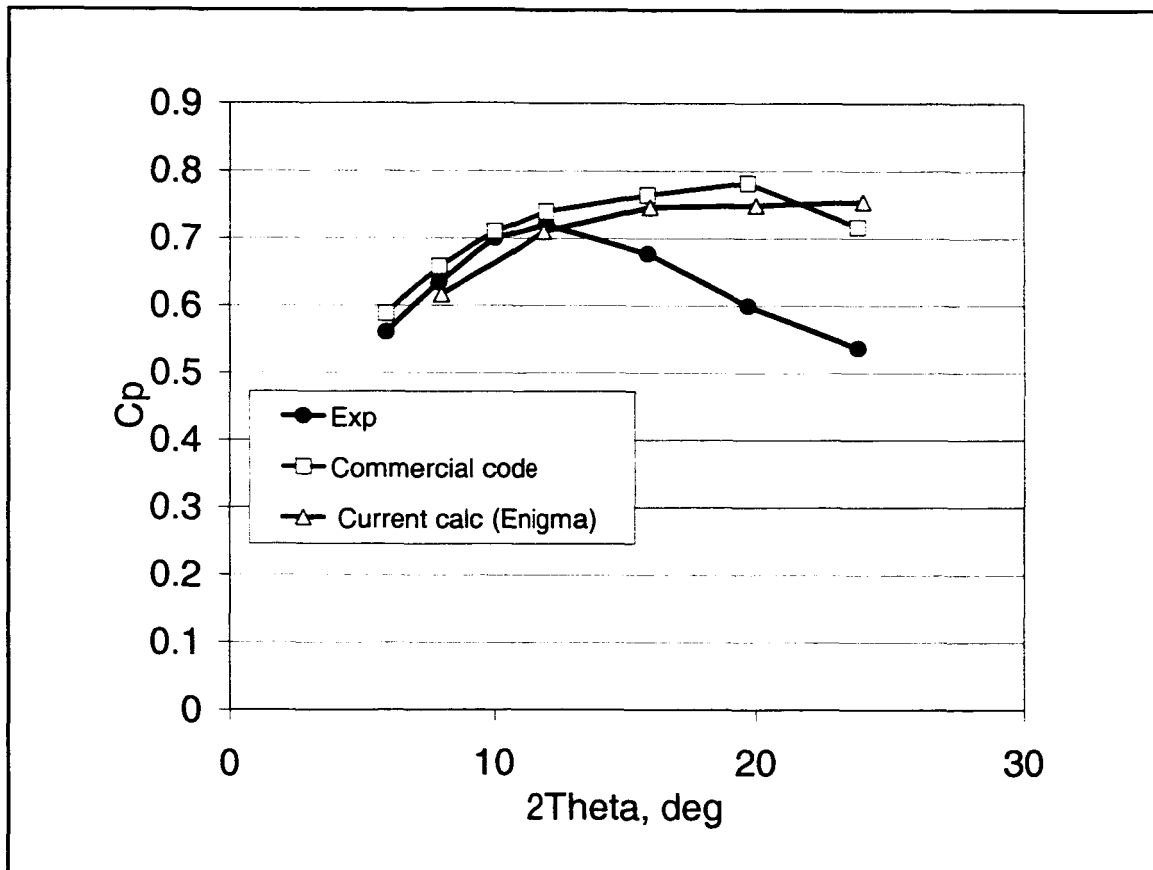
Figure 2. Predicted pressure recovery for the 2-D diffuser.
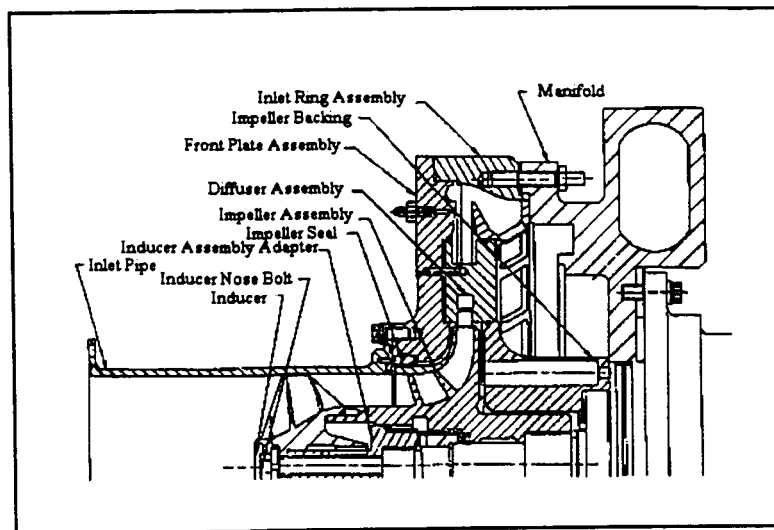
Figure 3. Cross-section of the consortium high-head impeller pump stage.
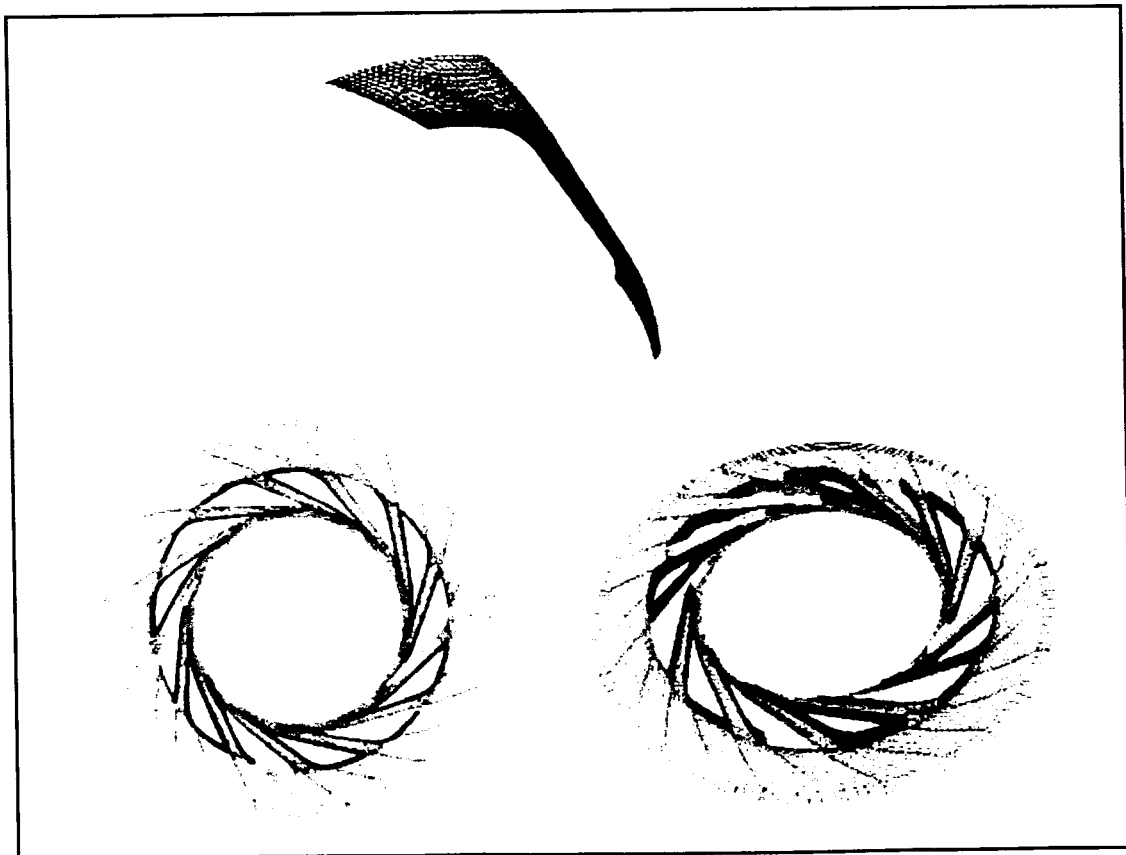
Figure 4. Flow mesh for vane-island diffuser with 13 vanes.
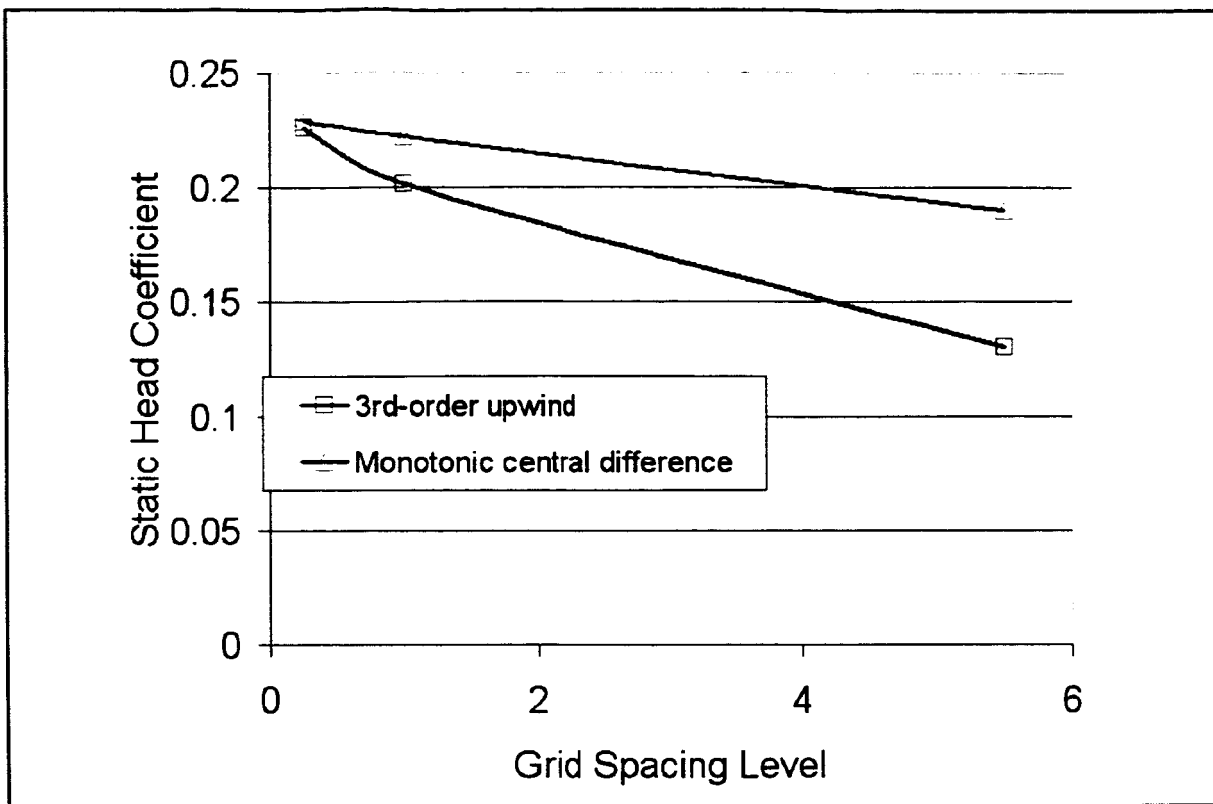
Figure 5. Grid resolution study for design flow conditions (grid spacing level of 0 is infinite/finest grid).
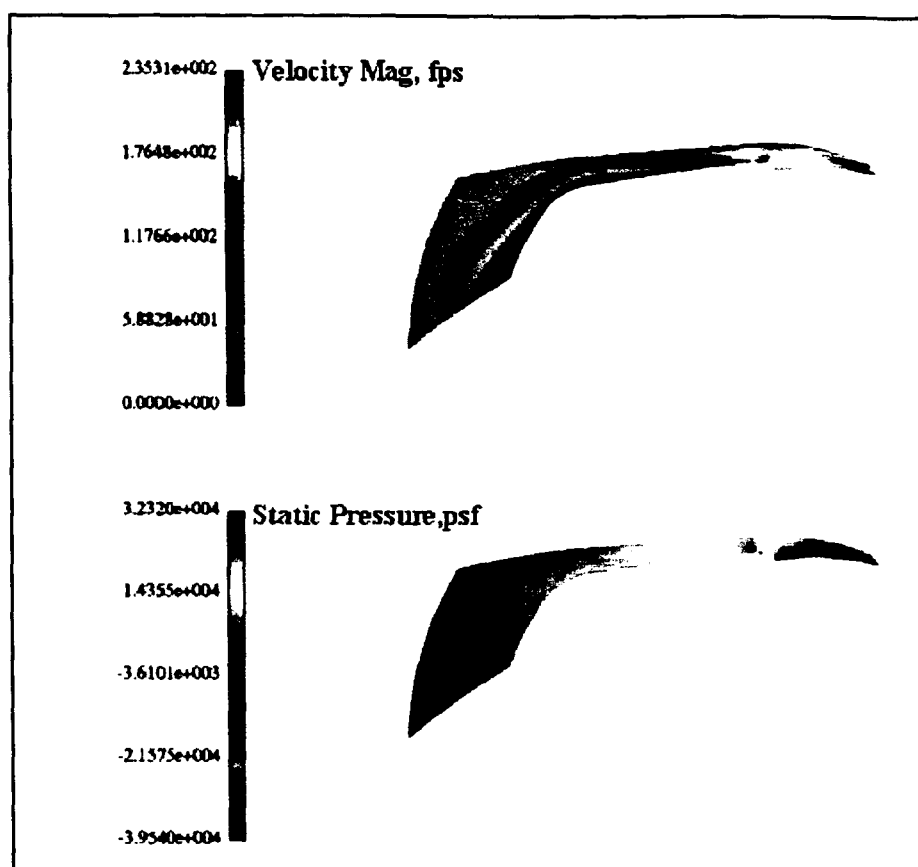
Figure 6. Typical velocity magnitude and pressure contours (design flow) for single periodic channel of consortium vane-island diffuser.
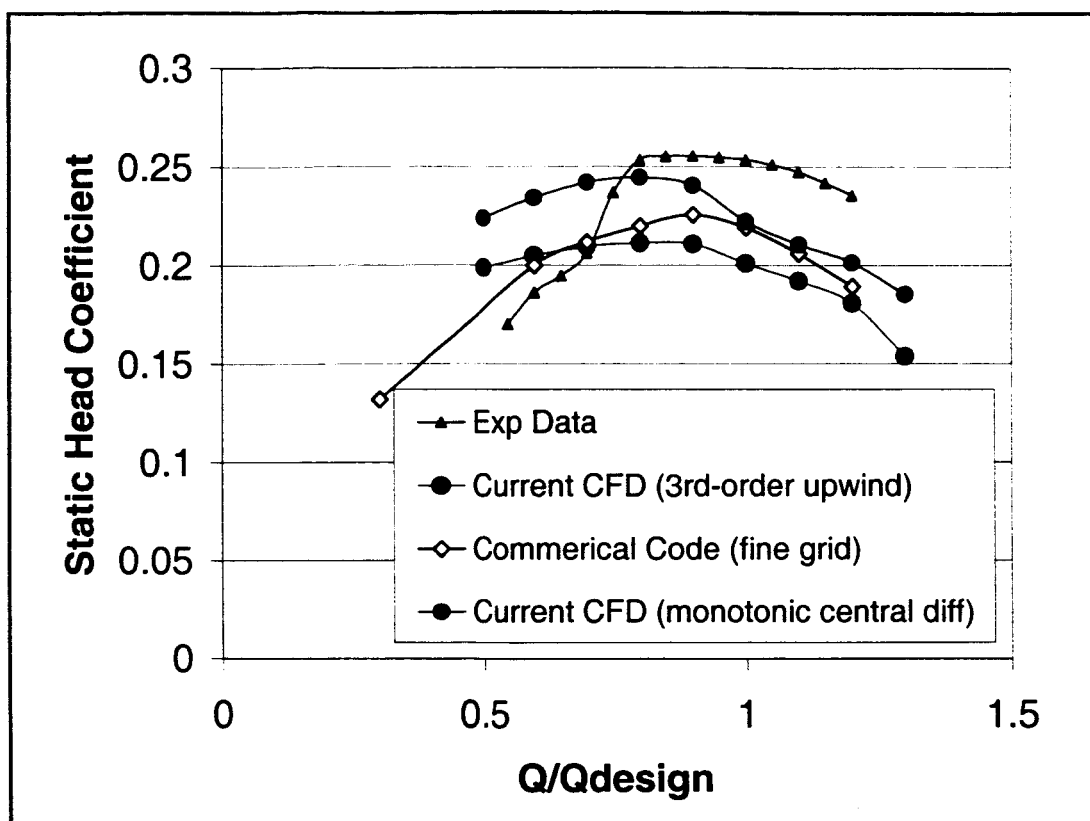
Figure 7. Predicted performance for single periodic channel model of consortium vane-island diffuser with uniform inflow conditions.
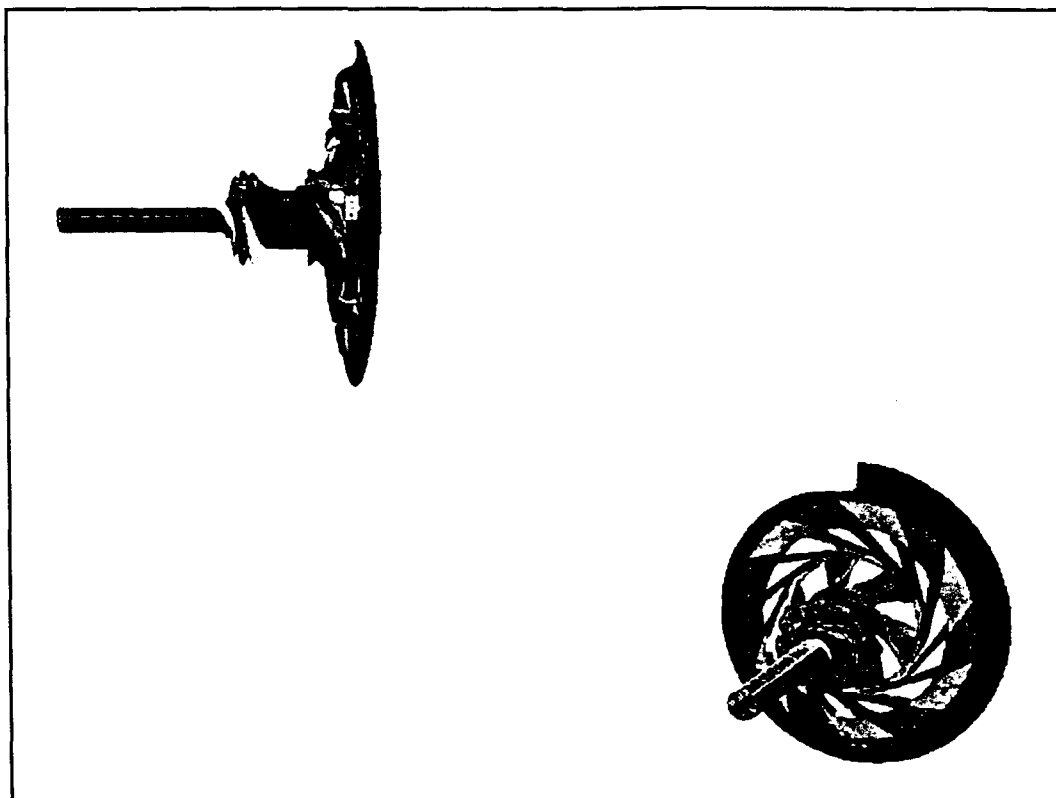
Figure 8. Consortium high head pump stage simulator with all flow channels.
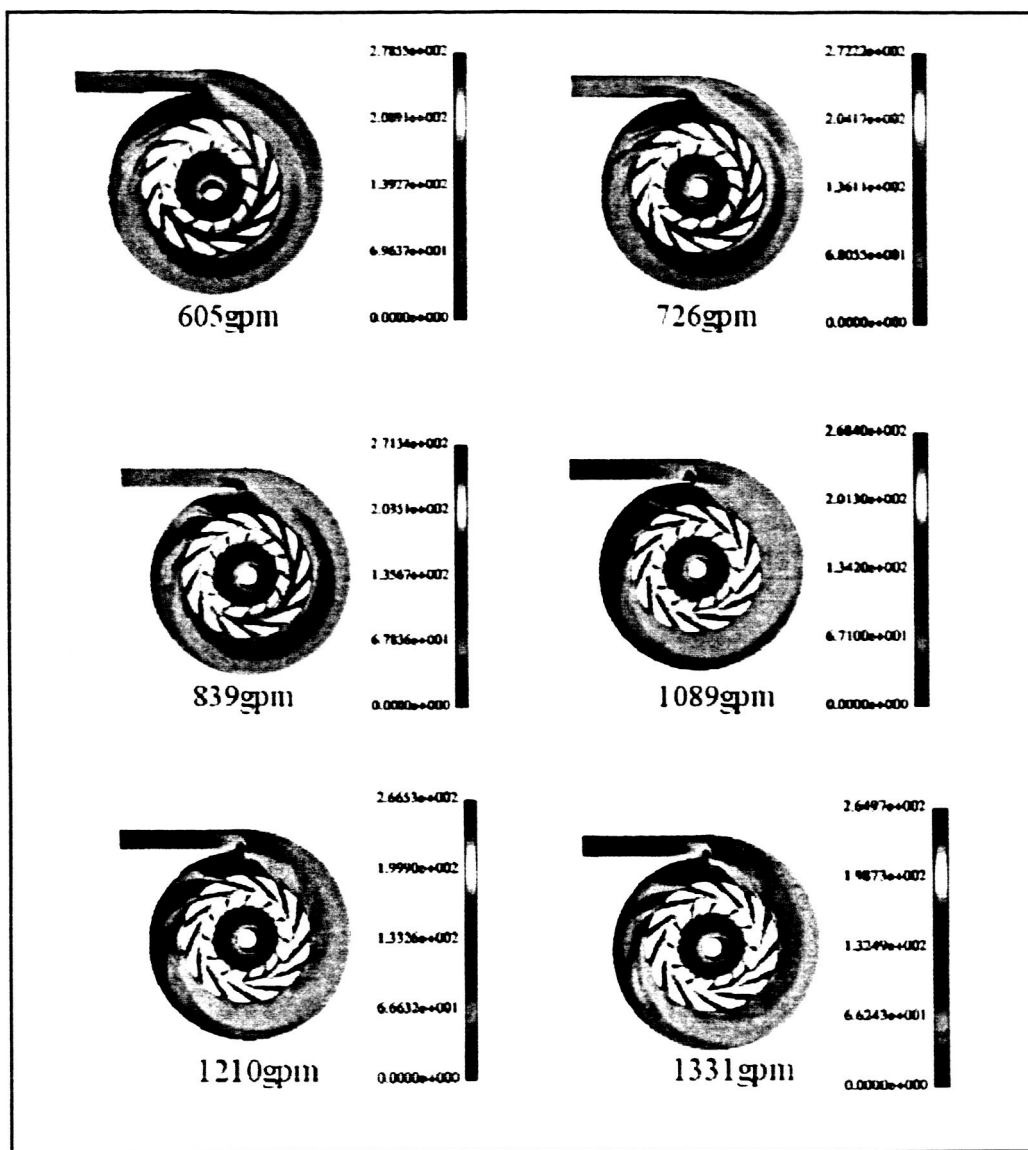
Figure 9. Computed velocity magnitude contours for the consortium high-head pump stage frozen-rotor model at arbitrary impeller/diffuser clocking.
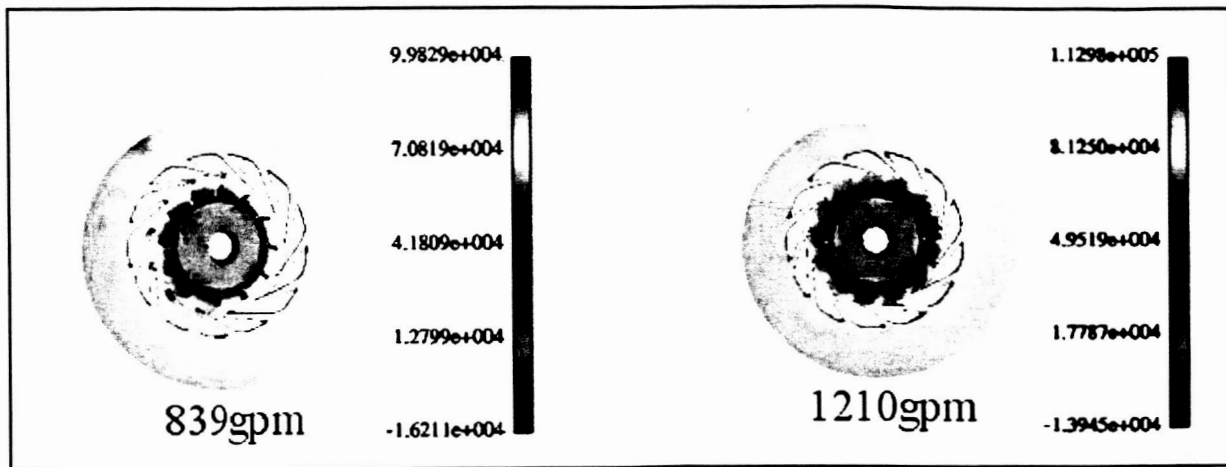
Figure 10. Typical computed pressure (psf) contours for the consortium high-head pump stage frozen- rotor model at arbitrary impeller/diffuser clocking.
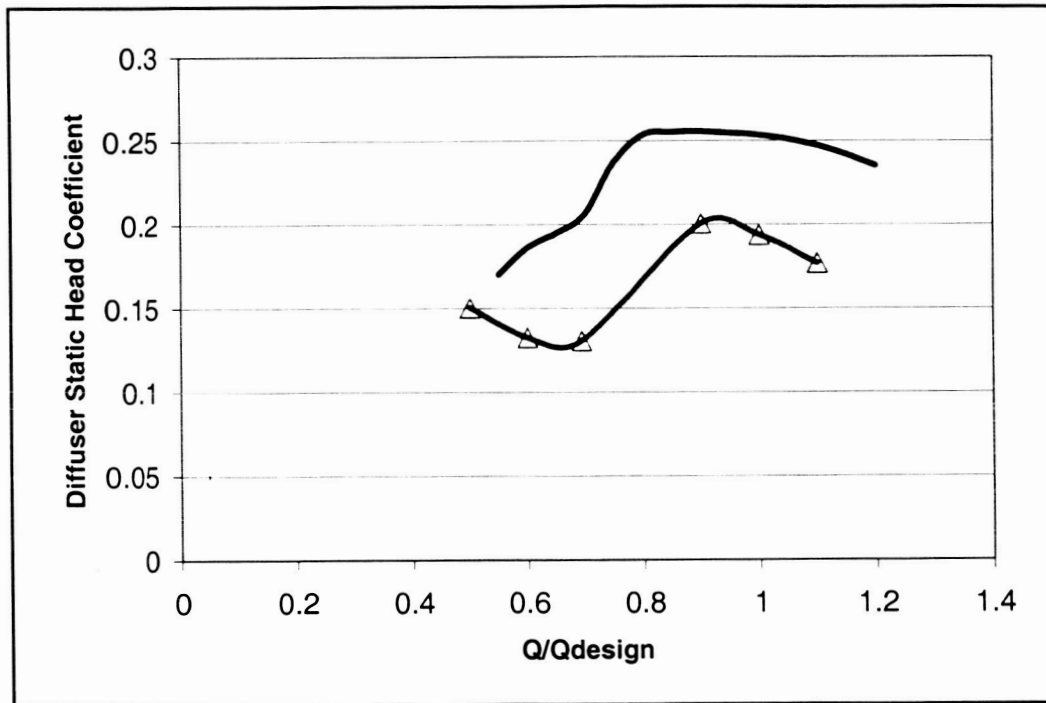
Figure 11. The coarse flow mesh predicted stall (triangles) comparison with experiment (solid line) for the consortium vane-island diffuser.
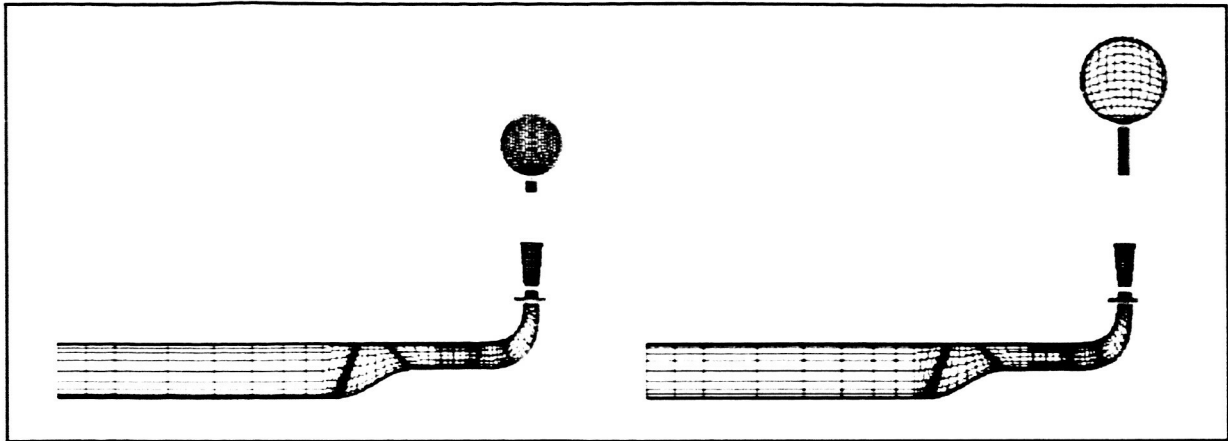
Figure 12. Proximity study: flow meshes with consortium pump stage "collector" approximately 0.4" and 2.0" from diffuser.
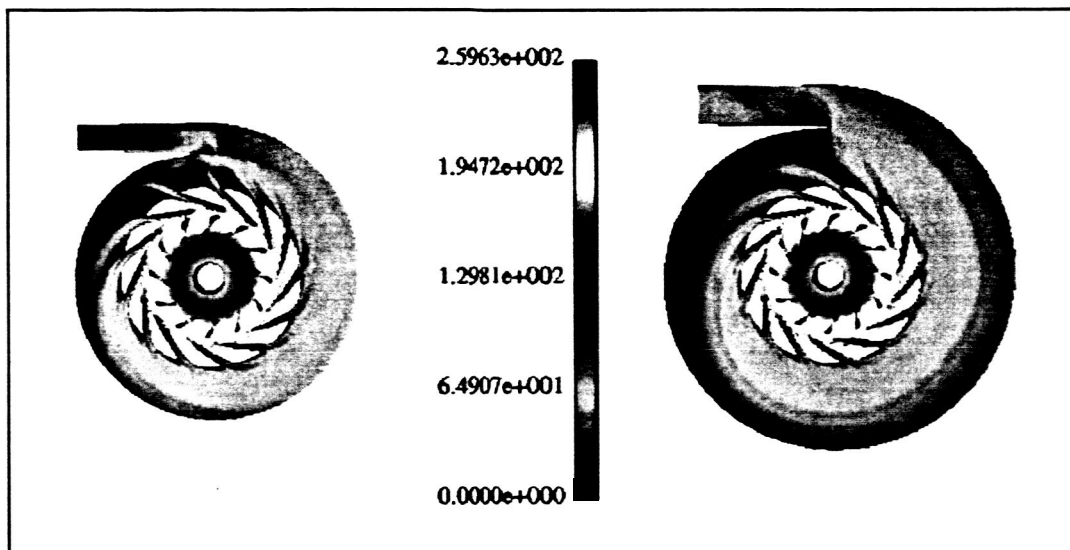
Figure 13. Proximity study: computed frozen-rotor velocity field (fps) for non-extended and extended collector geometry.
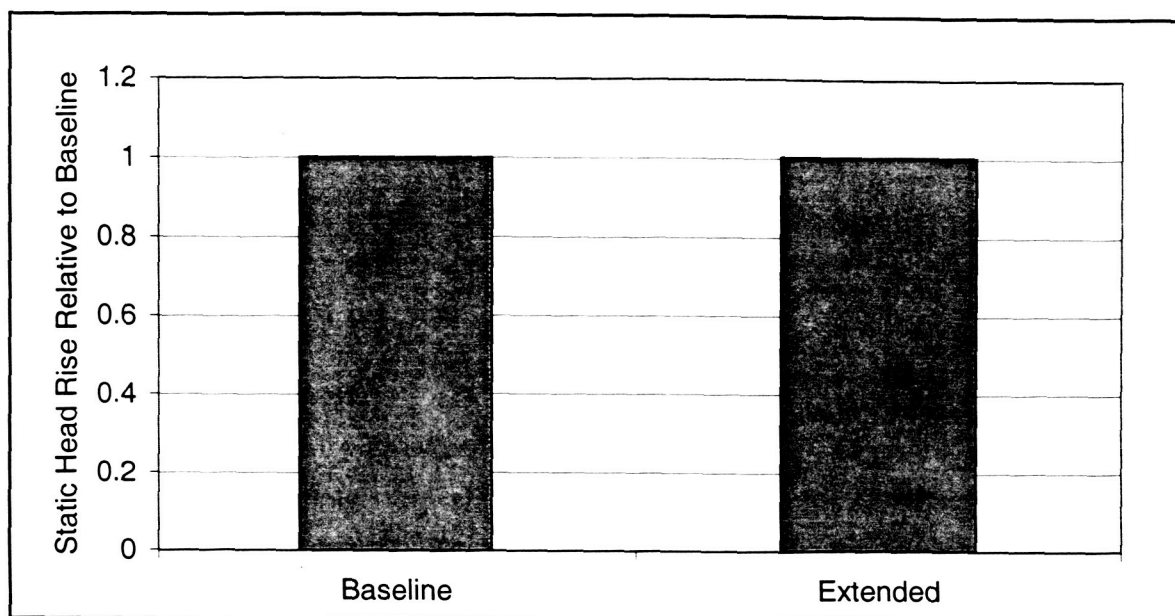
Figure 14. Proximity study: effect of collector proximity on diffuser static head rise.

R=4.596"
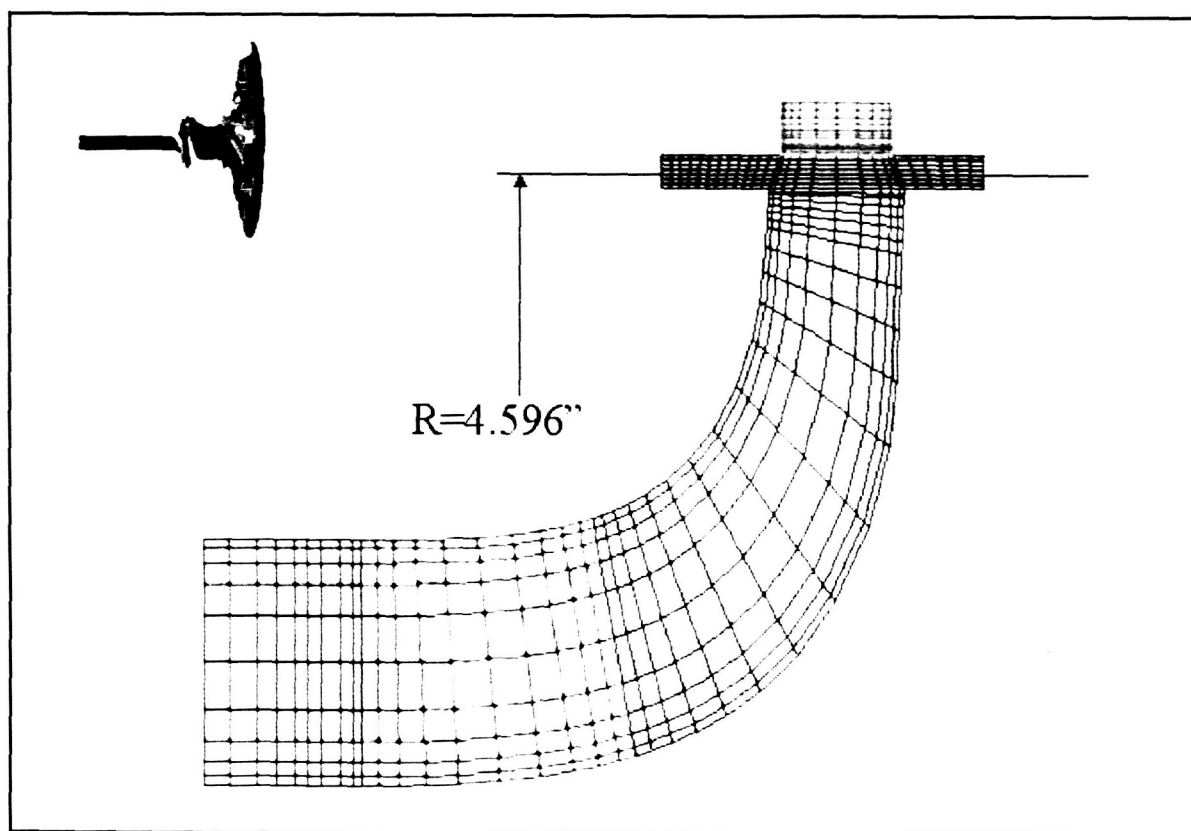
Figure 15. Location of numerical model plane for calculated velocities.
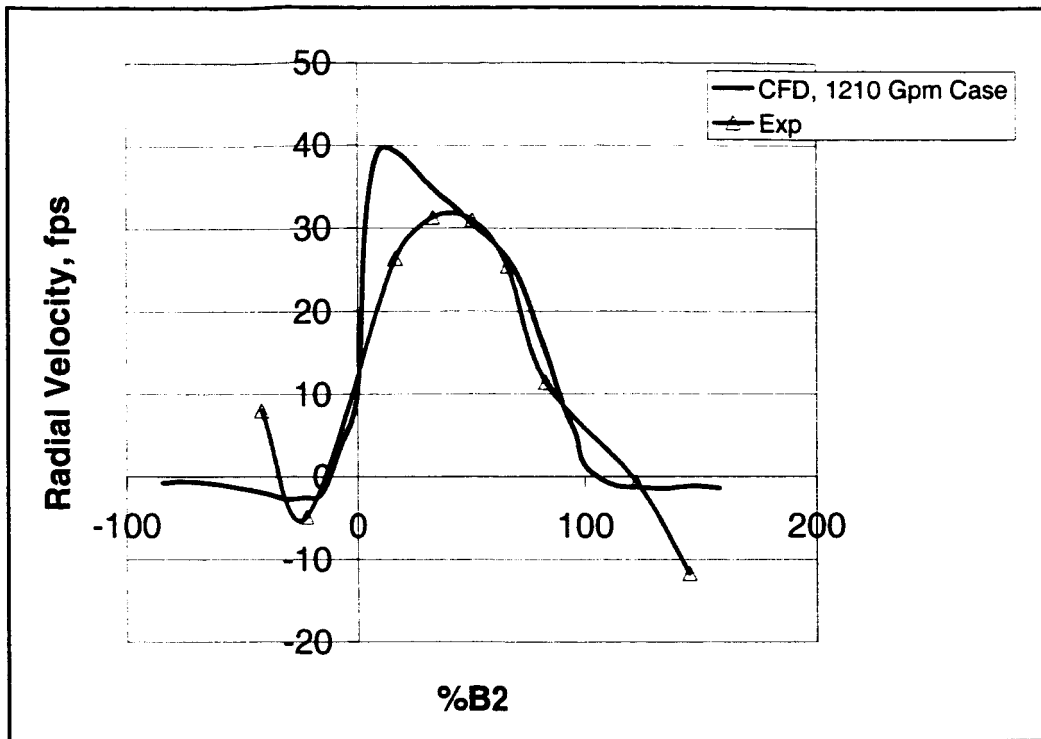
Figure 16. Comparison of computed radial velocity with experimental data for design flow case.
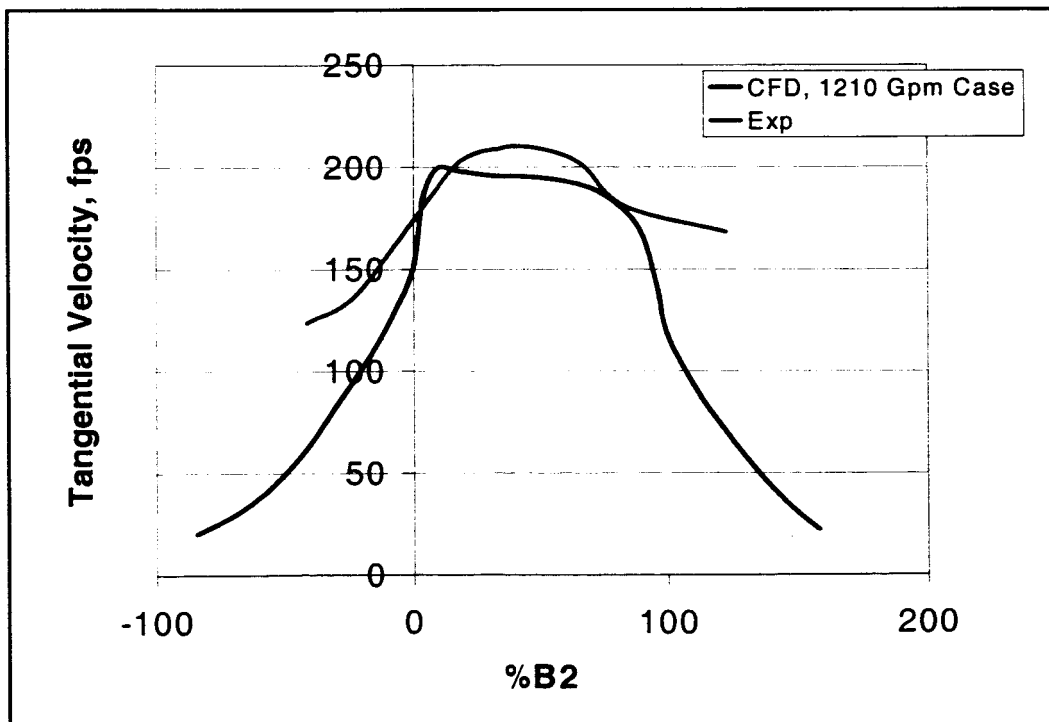
Figure 17. Comparison of computed absolute tangential velocity with experimental data for design flow case.
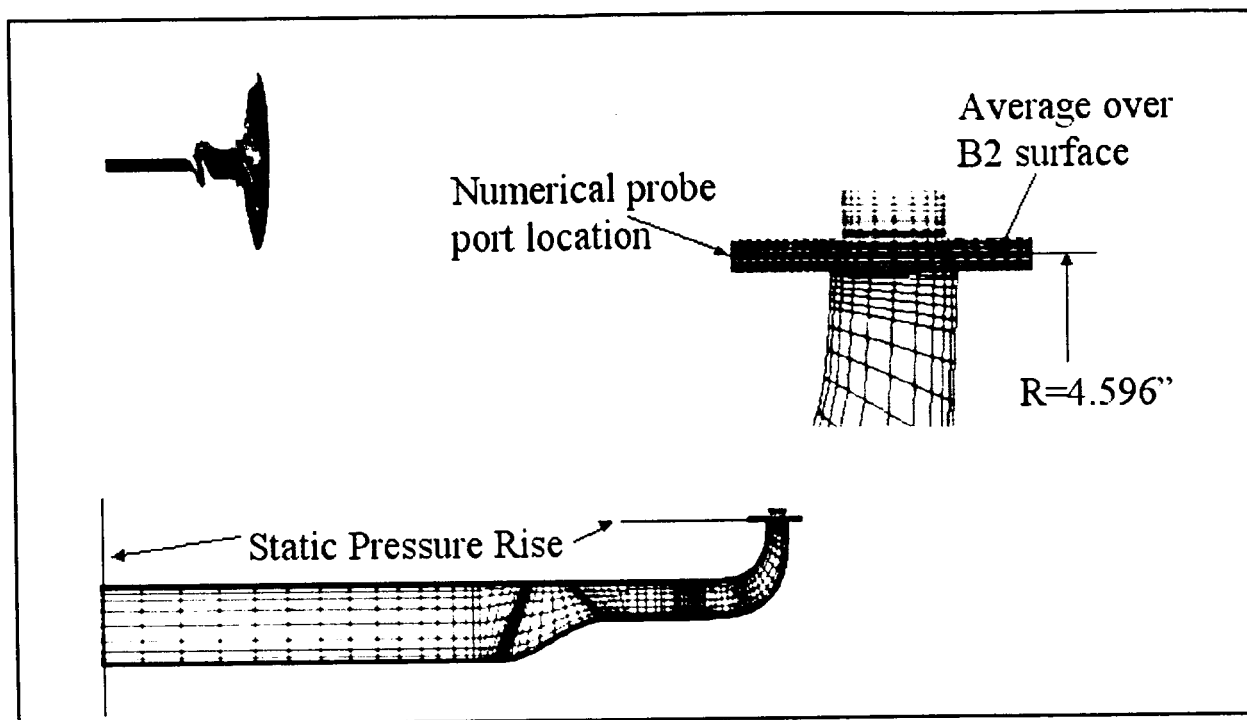
Figure 18. Location of static pressure rise planes for numerical model (numerical model inlet pressure= 50psi).
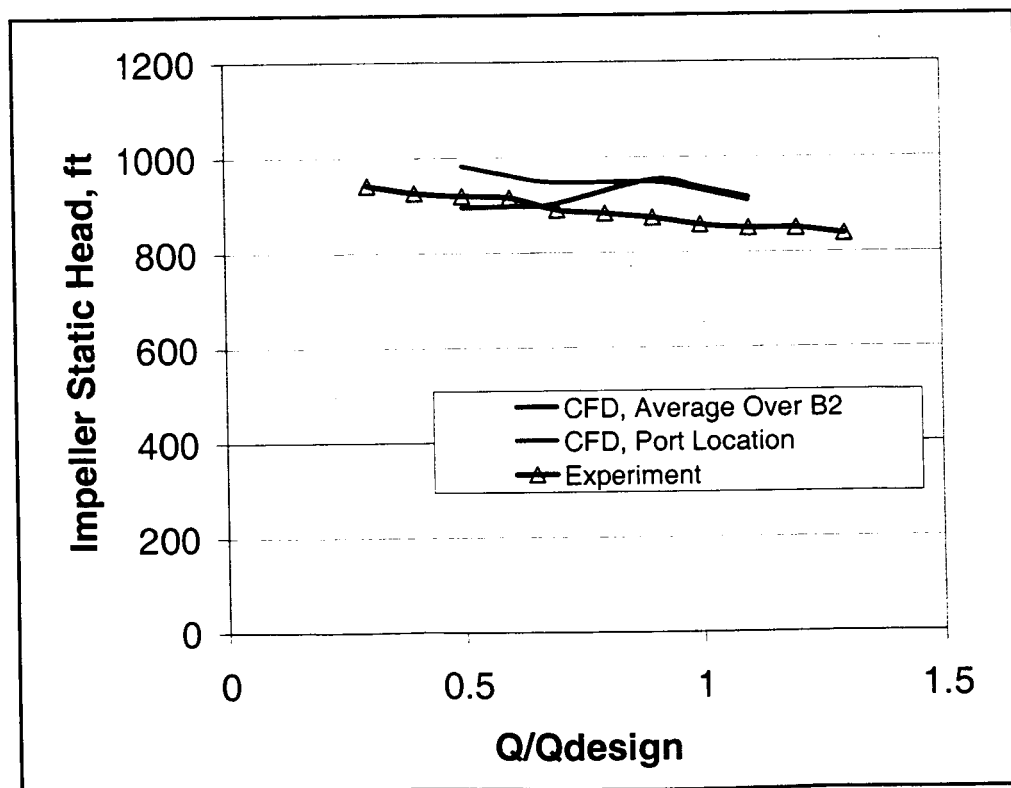
Figure 19. Comparison of calculated impeller static pressure rise with experimental data.
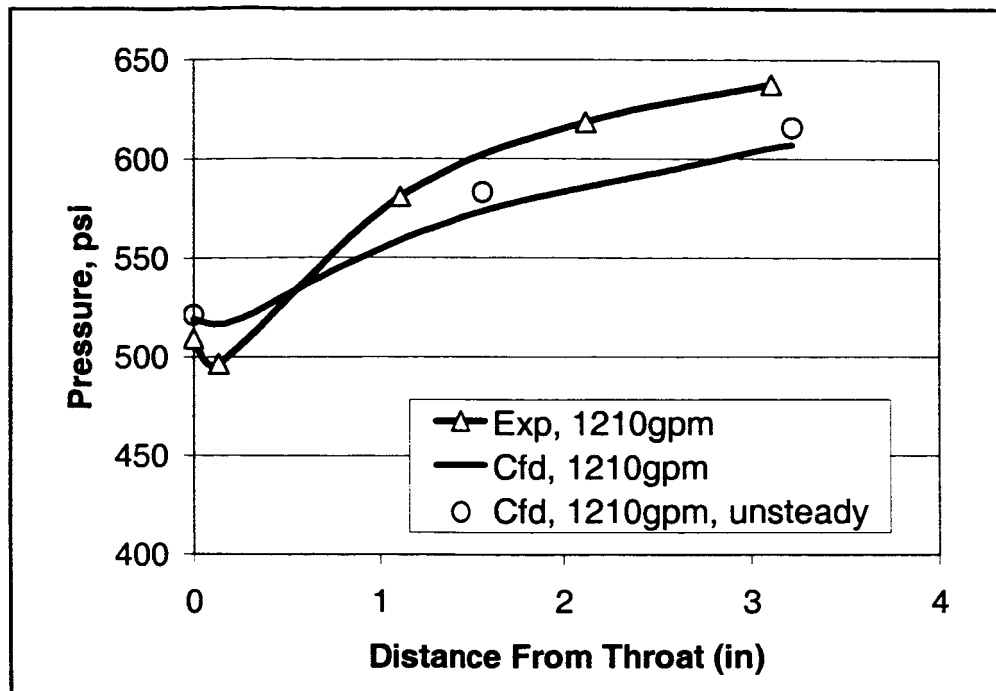
Figure 20. Comparison of calculated diffuser shroud static pressure with experimental data for the design flow case.
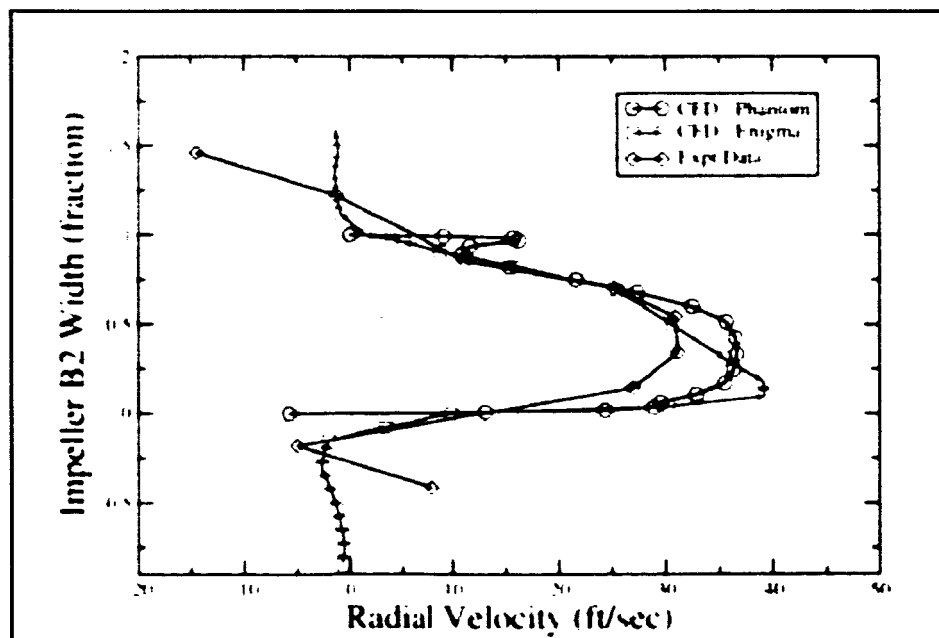
Figure 21. Coarse mesh (Enigma) and fine mesh (Phantom) comparisons for the impeller discharge radial velocity.
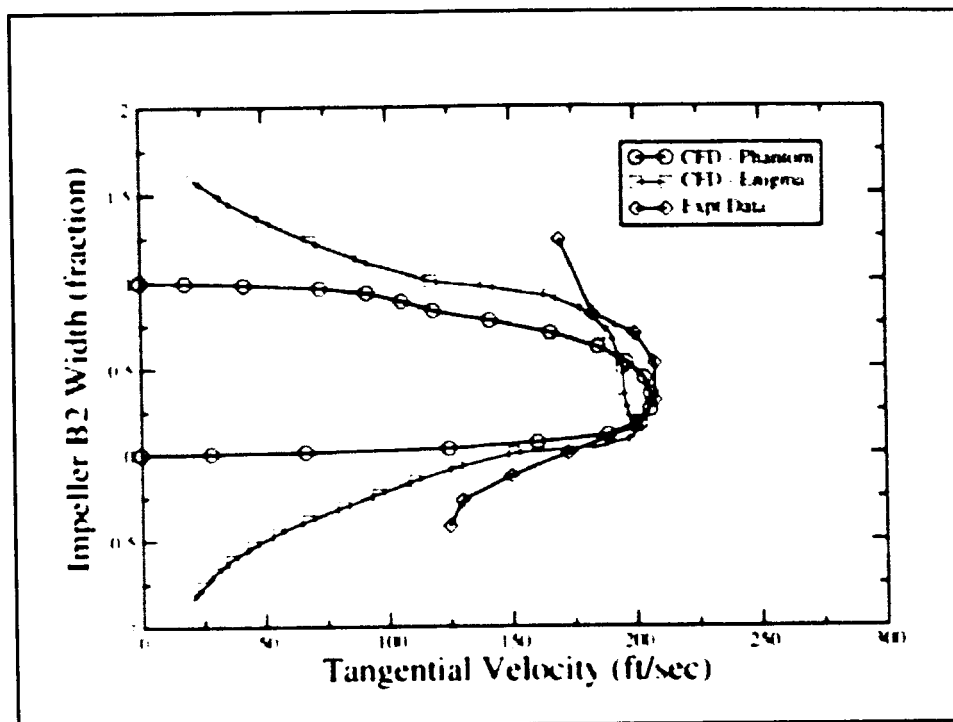
Figure 22. Coarse mesh (Enigma) and fine mesh (Phantom) comparisons for the impeller discharge tangential velocity.
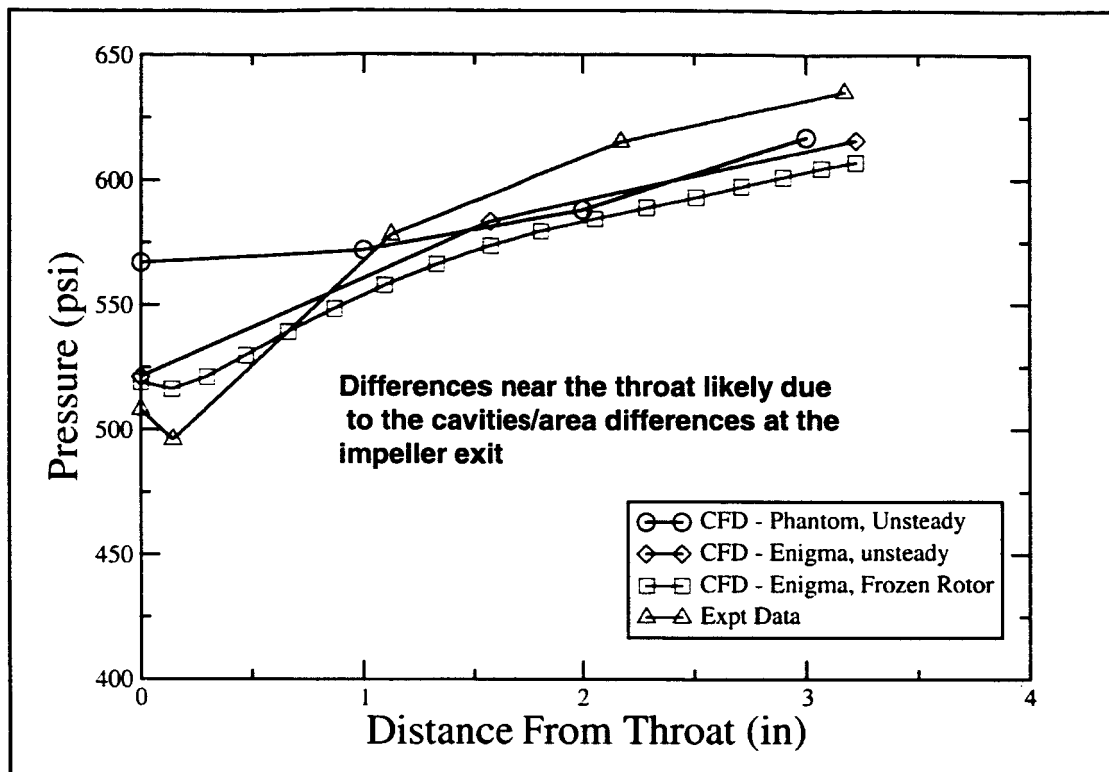
Figure 23. Coarse mesh (Enigma) and fine mesh (Phantom) comparisons for diffuser channel shroud pressure rise (inserted commented per Dr. Dan Dorney)
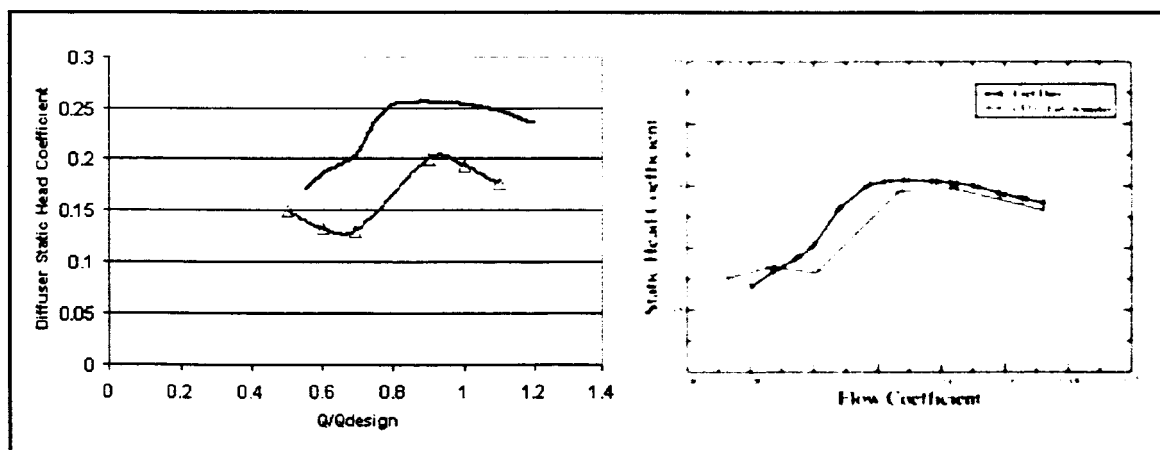
Figure 24. Coarse mesh (Enigma) and fine mesh (Phantom) comparisons for diffuser head rise.
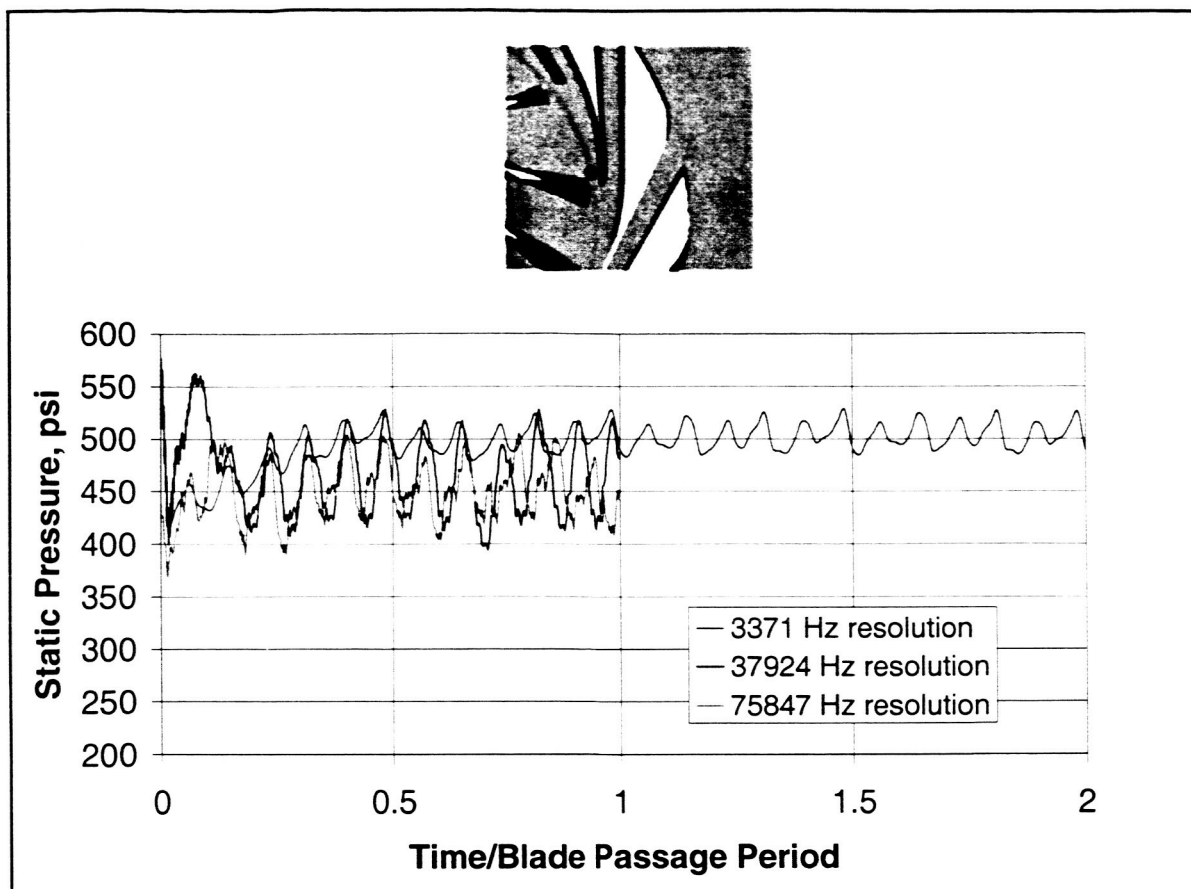
Figure 25. Effect of time resolution of static pressure trace for 1210 gpm consortium pump stage case; results reported for a point mid-way between hub and shroud at a radius=4.685" between impeller and diffuser (see the insert above).
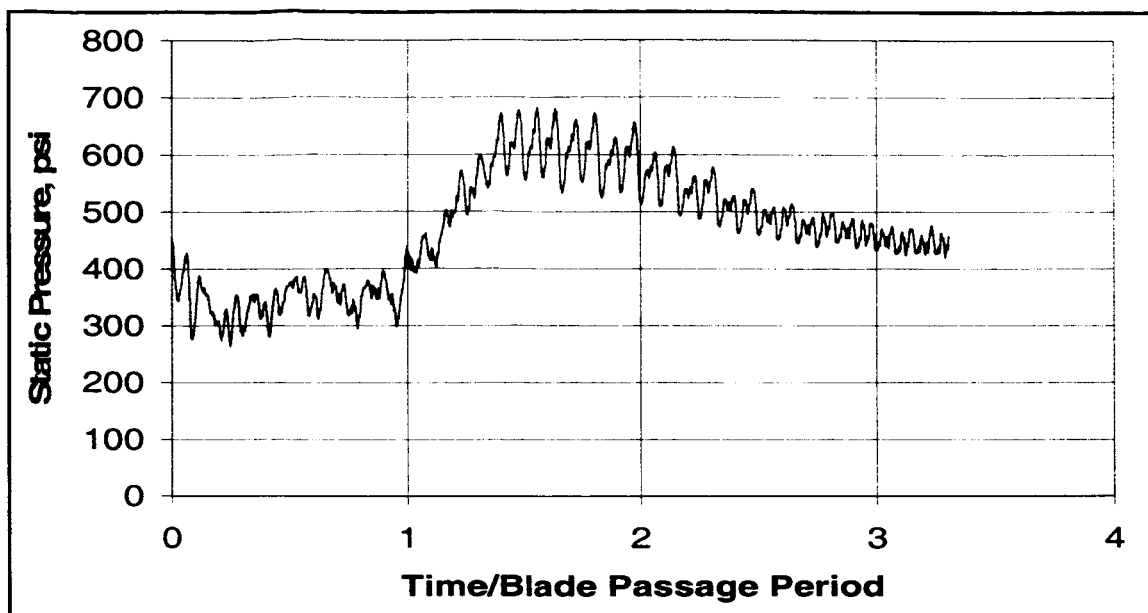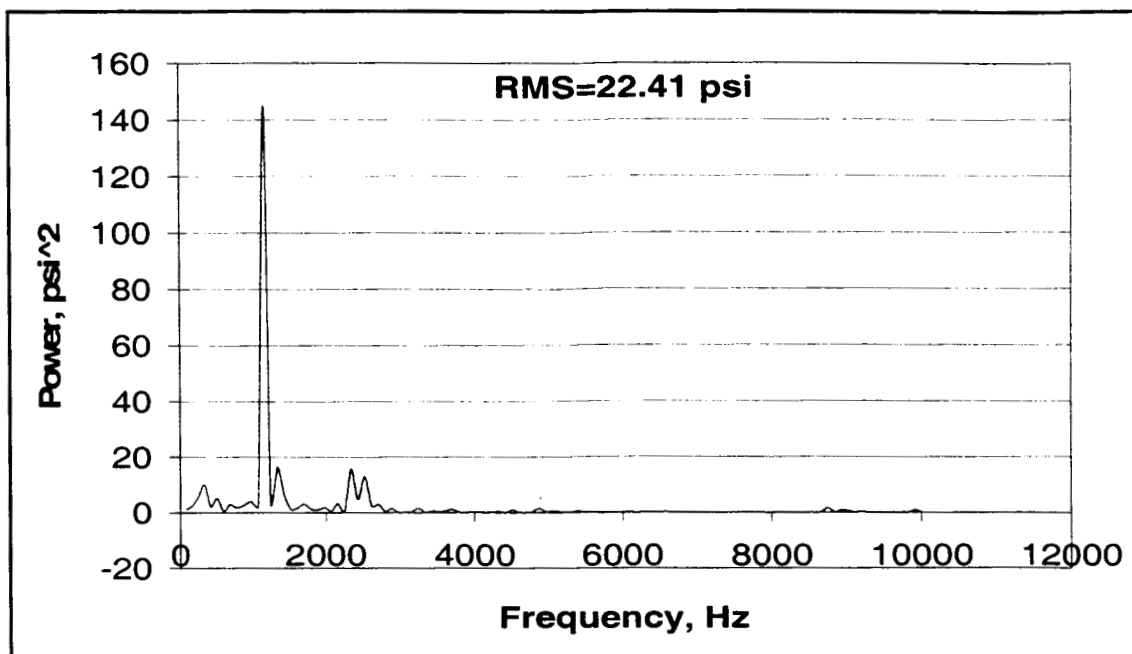
Figure 26. The computed pressure time-history trace for the 605 gpm flow case (75,847 Hz resolution); results reported for a point mid-way between hub and shroud at a radius=4.685" between impeller and diffuser.
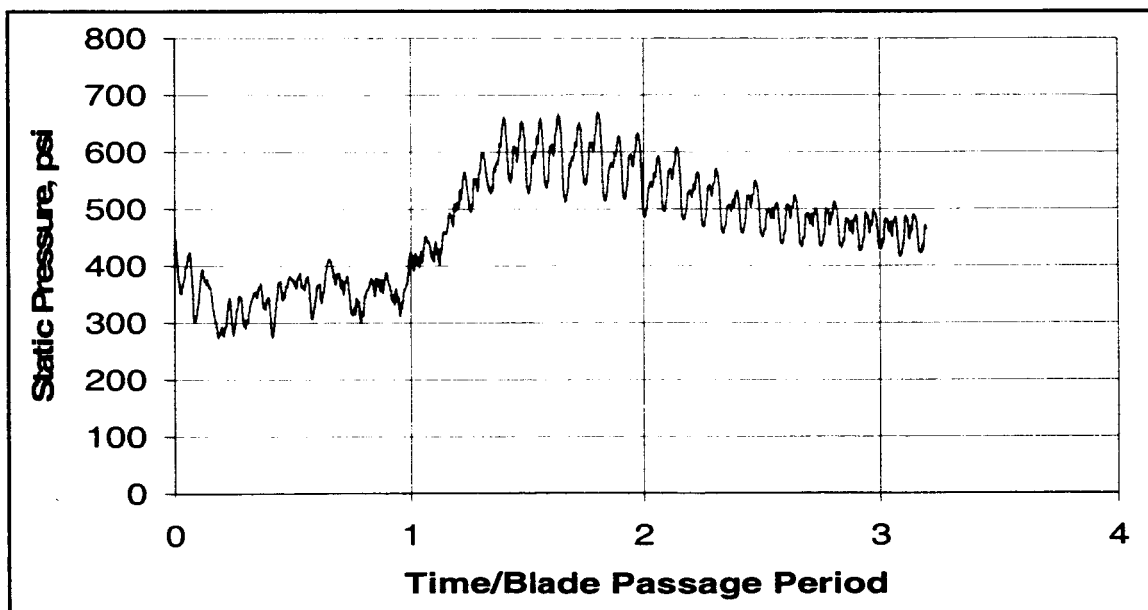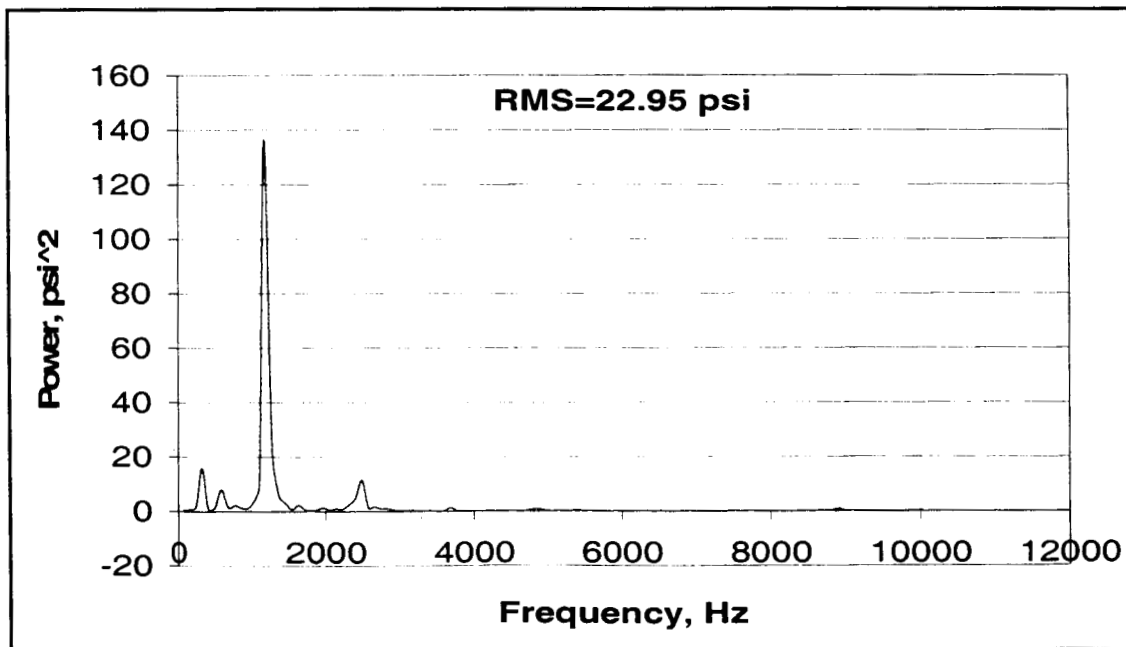

Figure 27. The computed pressure time-history trace for the 726 gpm flow case (75,847 Hz resolution); results reported for a point mid-way between hub and shroud at a radius=4.685" between impeller and diffuser.
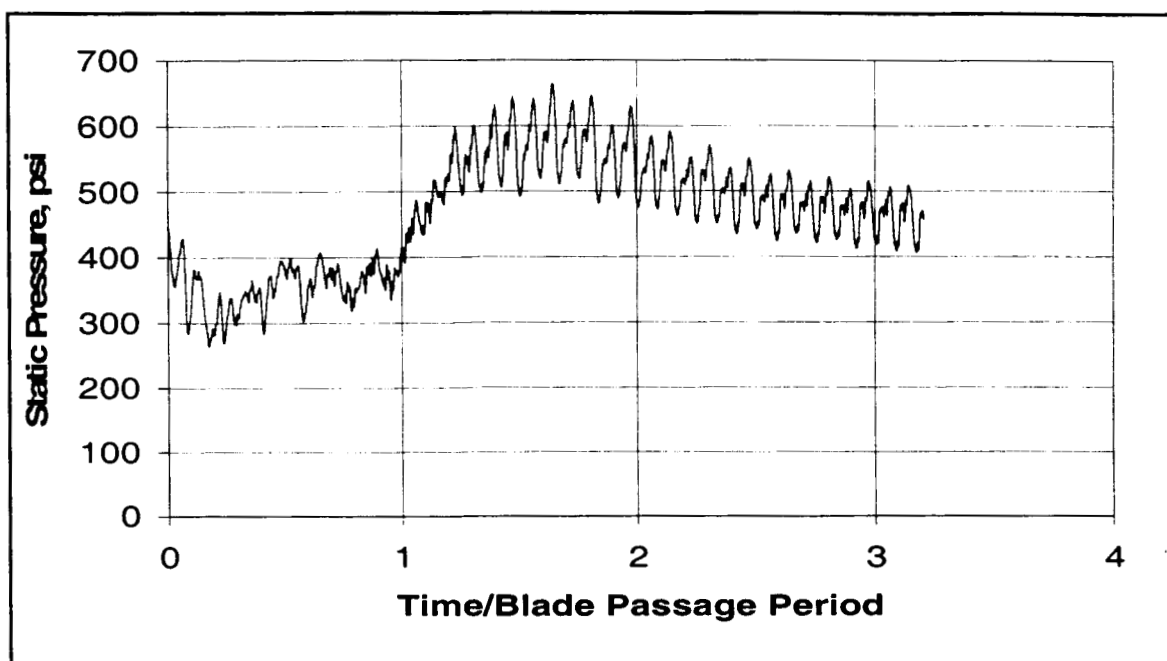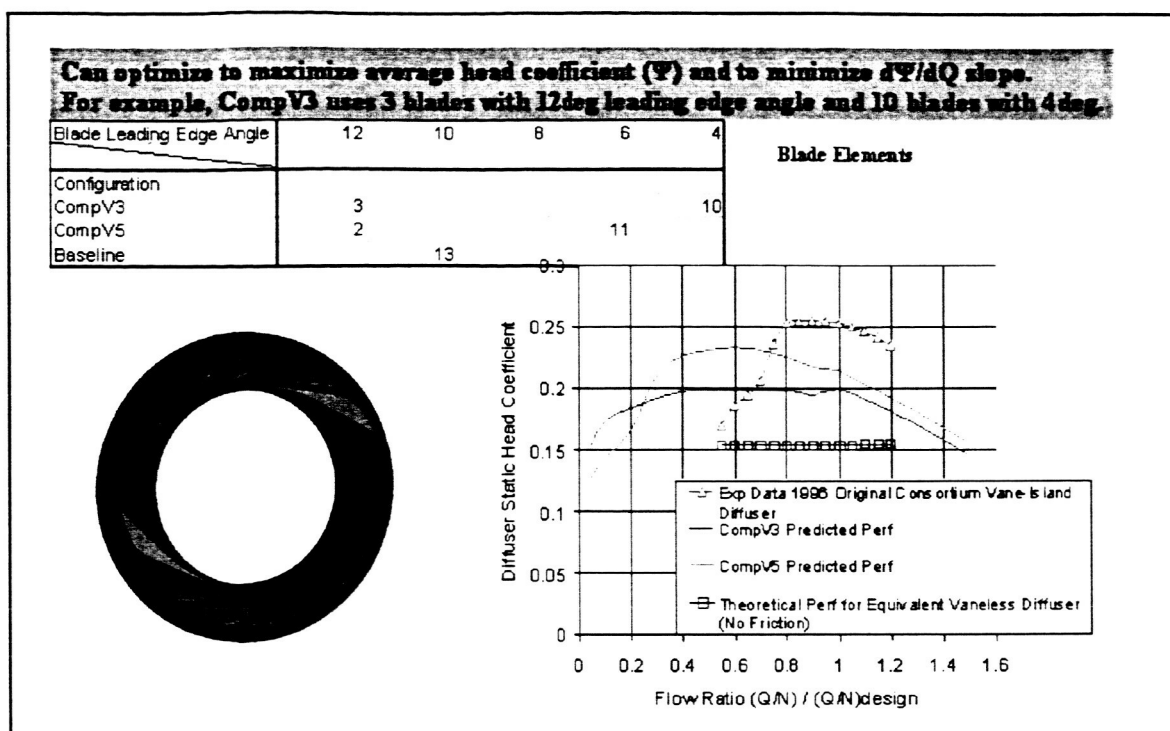
Figure 28. The computed pressure time-history trace for the 839 gpm flow case (75,847 Hz resolution); results reported for a point mid-way between hub and shroud at a radius=4.685" between impeller and diffuser.
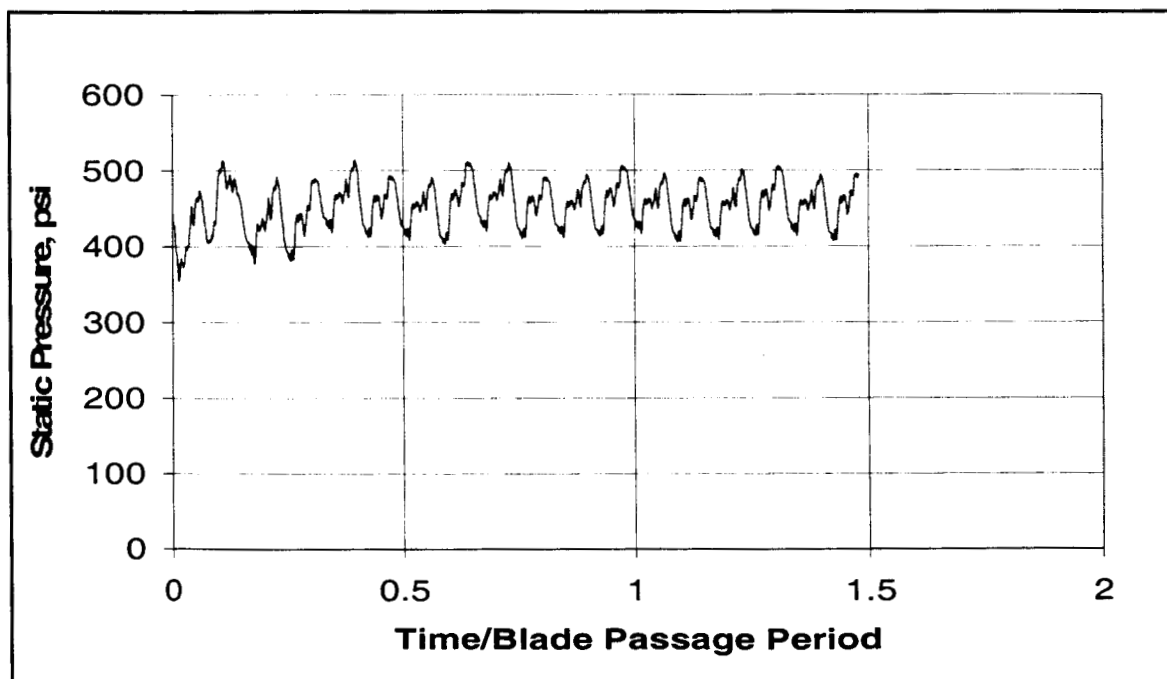
Figure 29. The computed pressure time-history trace for the 1089 gpm flow case (75,847 Hz resolution); results reported for a point mid-way between hub and shroud at a radius=4.685" between impeller and diffuser.
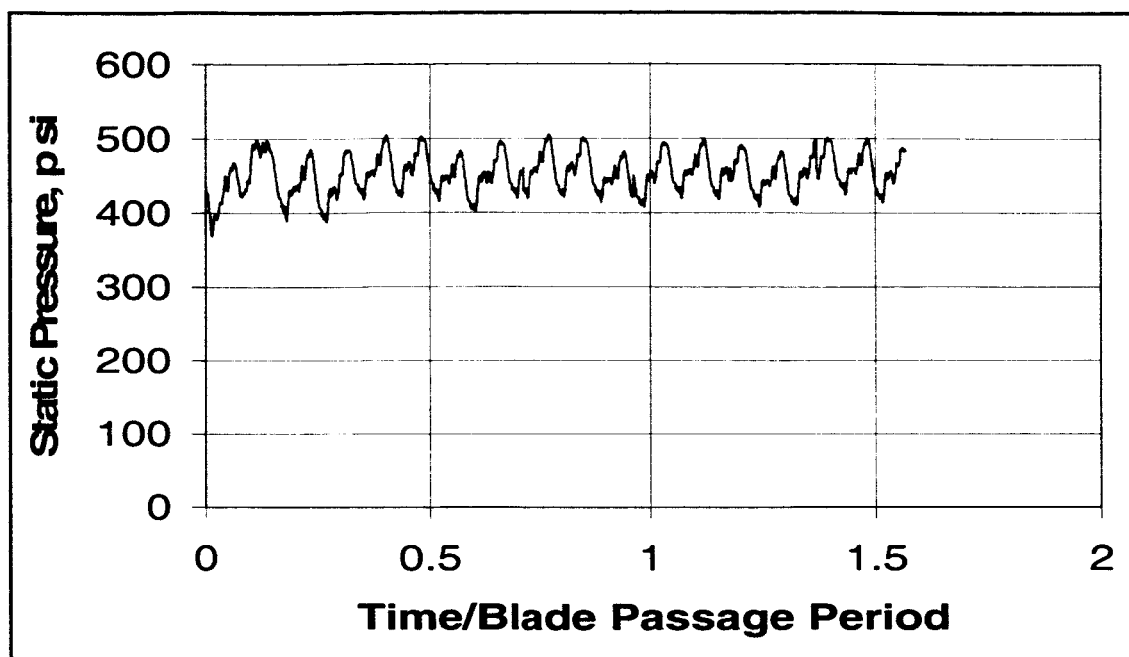
Figure 30. The computed pressure time-history trace for the 1210 gpm flow case (75,847 Hz resolution); results reported for a point mid-way between hub and shroud at a radius=4.685" between impeller and diffuser.
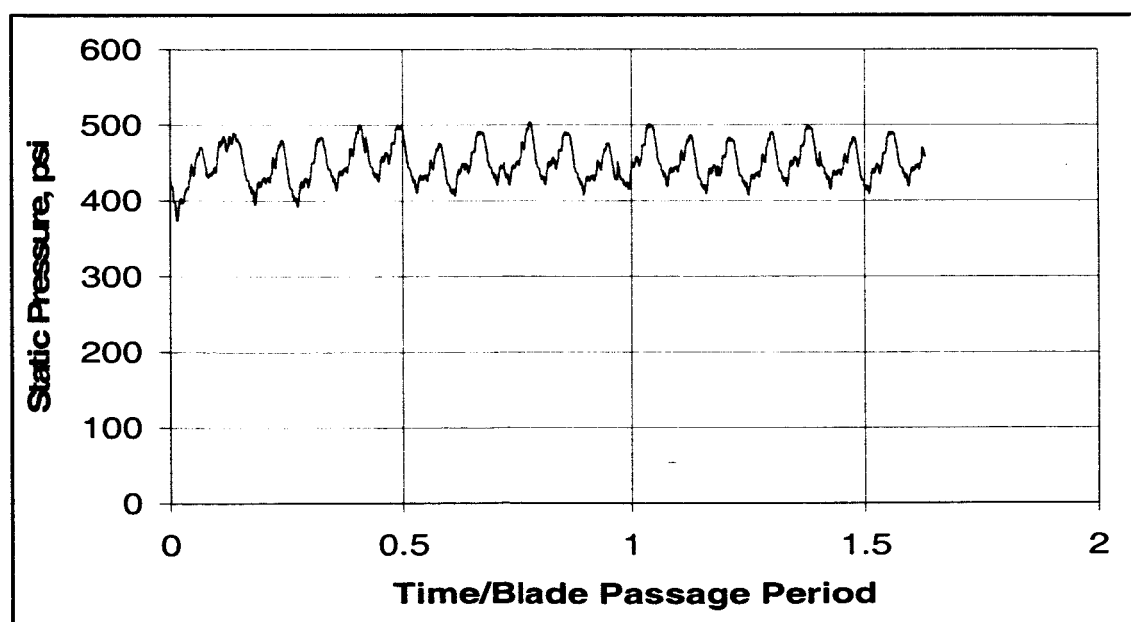
Figure 31. The computed pressure time-history trace for the 1331 gpm flow case (75,847 Hz resolution); results reported for a point mid-way between hub and shroud at a radius=4.685" between impeller and diffuser.
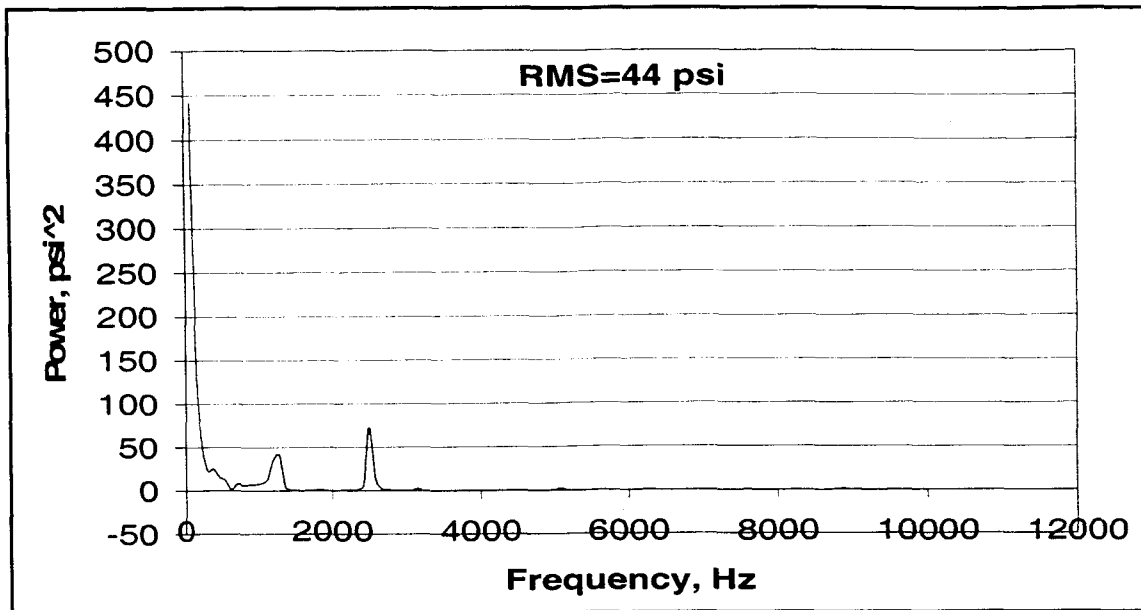
Figure 32. The computed pressure power spectrum for the 605 gpm flow deep stall case (75,847 Hz resolution); results reported for a point mid-way between hub and shroud at a radius=4.685" between impeller and diffuser.
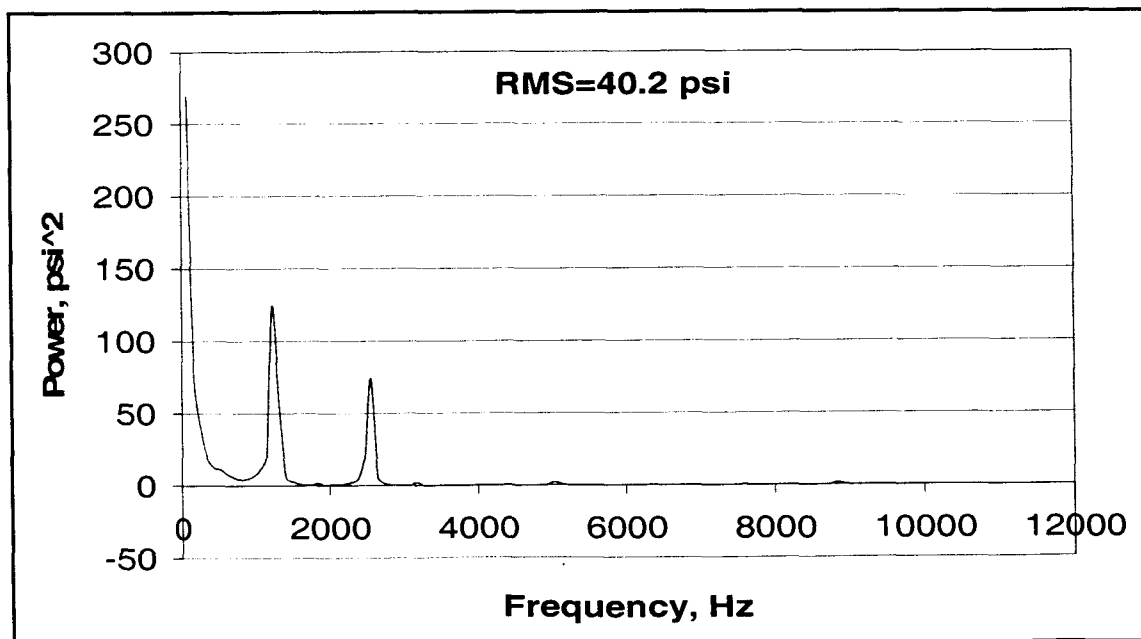
Figure 33. The computed pressure power spectrum for the 726 gpm flow deep stall case (75,847 Hz resolution); results reported for a point mid-way between hub and shroud at a radius=4.685" between impeller and diffuser.
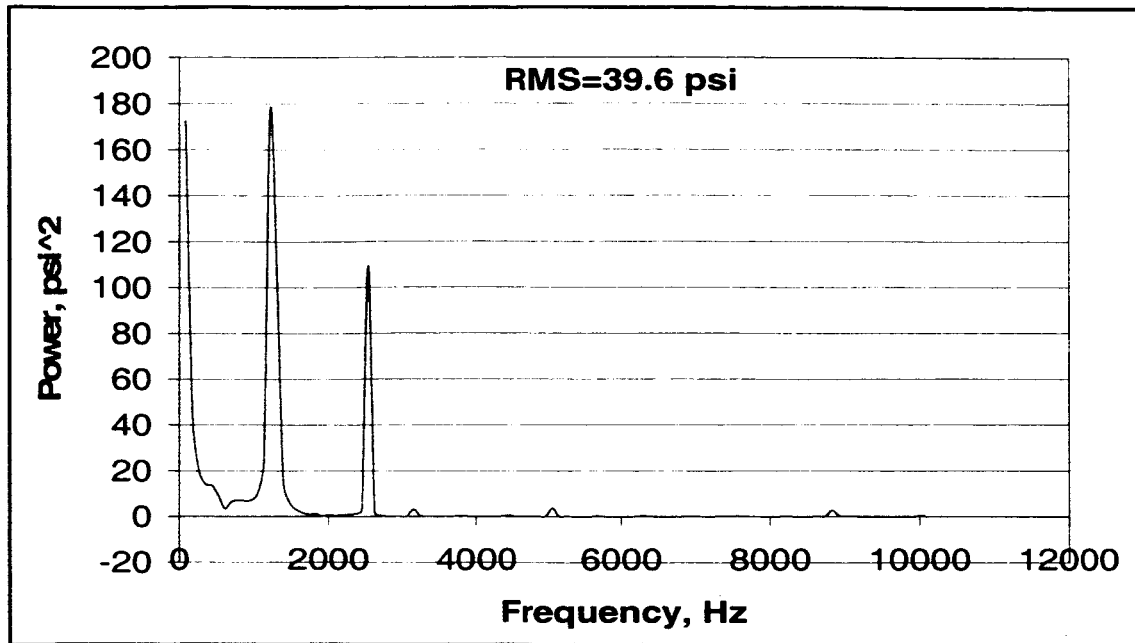
Figure 34. The computed pressure power spectrum for the 839 gpm flow deep stall case (75,847 Hz resolution); results reported for a point mid-way between hub and shroud at a radius=4.685" between impeller and diffuser.
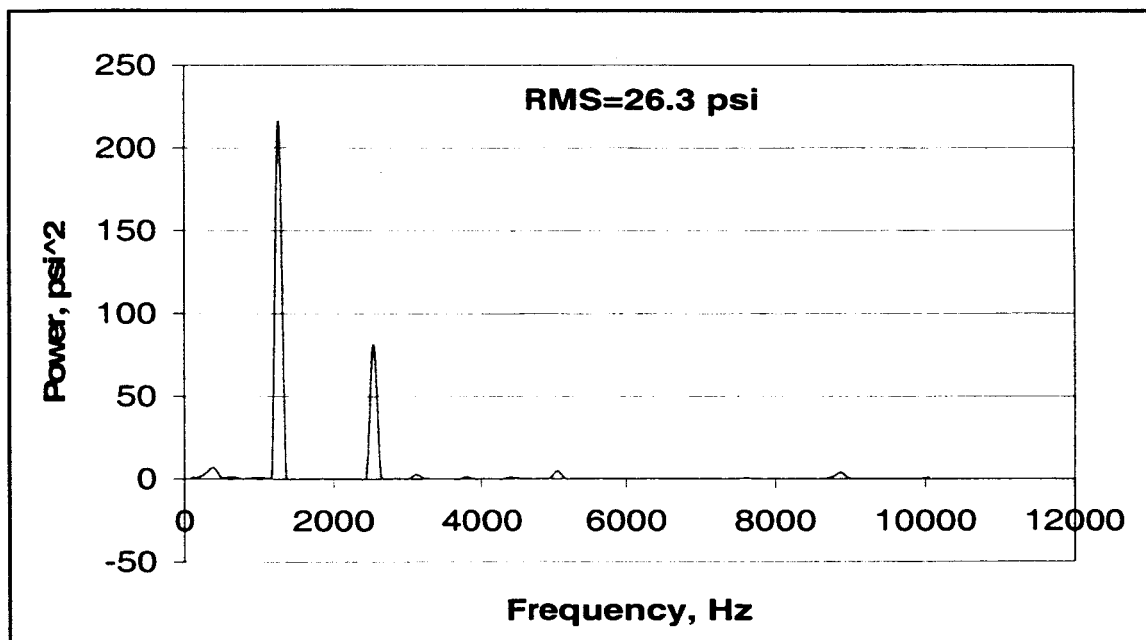
Figure 35. The computed pressure power spectrum for the 1089 gpm flow case (75,847 Hz resolution); results reported for a point mid-way between hub and shroud at a radius=4.685" between impeller and diffuser.

126

RMS=22.41 psi

Power, psi^2 / Frequency, Hz

Figure 36. The computed pressure power spectrum for the 1210 gpm flow case (75,847 Hz resolution); results reported for a point mid-way between hub and shroud at a radius=4.685" between impeller and diffuser.
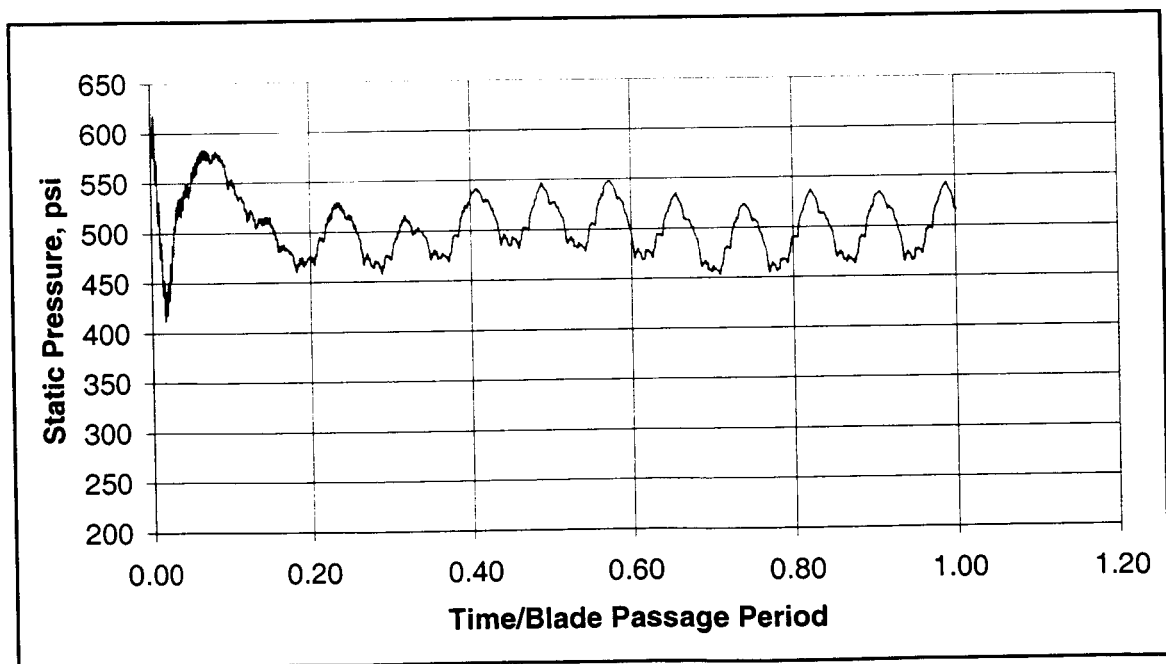
RMS=22.95 psi

Power, psi^2 / Frequency, Hz

Figure 37. The computed pressure power spectrum for the 1331 gpm flow case (75,847 Hz resolution); results reported for a point mid-way between hub and shroud at a radius=4.685" between impeller and diffuser.

| Blade Leading Edge Angle	12	10	8	6	4	Blade Elements
Configuration						
CompV3	3				10	
CompV5	2			11		
Baseline		13				

Figure 38. Example of a composite vane design for wide-flow-range.
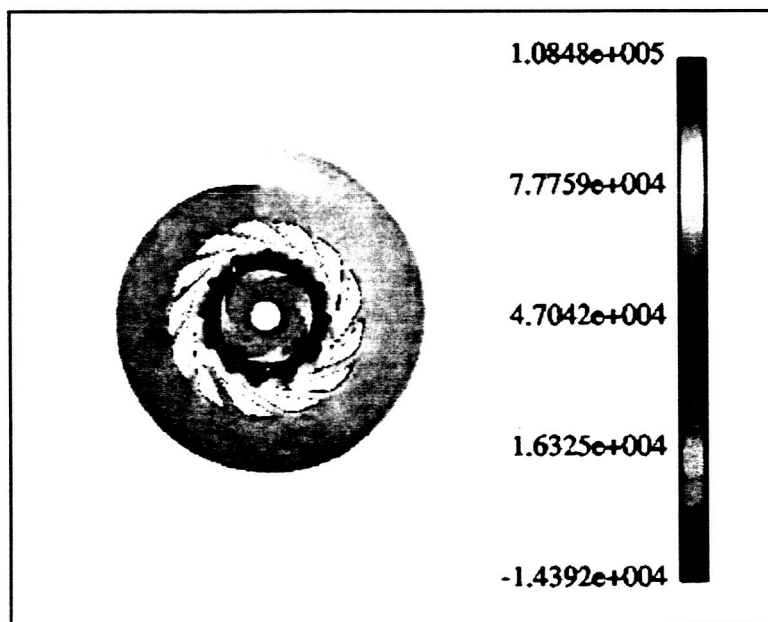
Figure 39. Composite vane design CompV10: computed frozen rotor pressure (psf) distribution for 0.7 flow ratio.
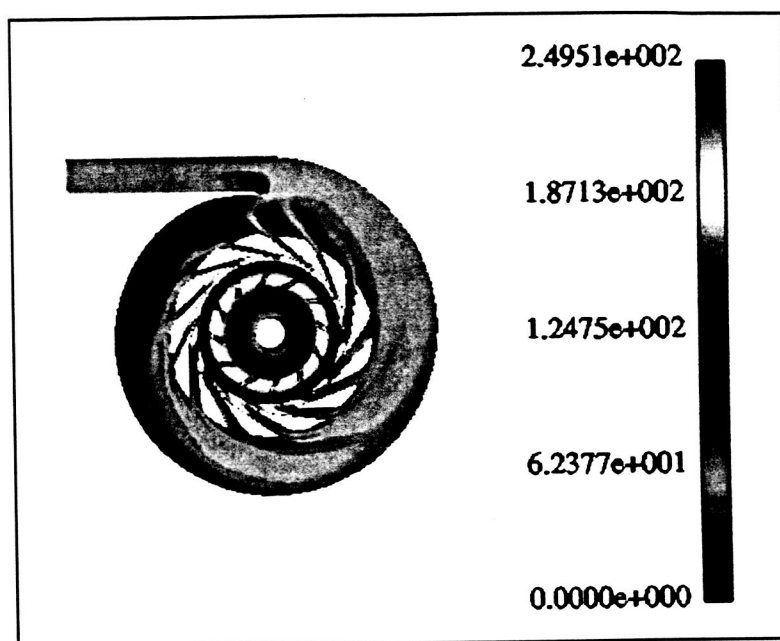
Figure 40. Composite vane design CompV10: computed frozen-rotor velocity magnitude (fps) distribution for 0.7 flow ratio.
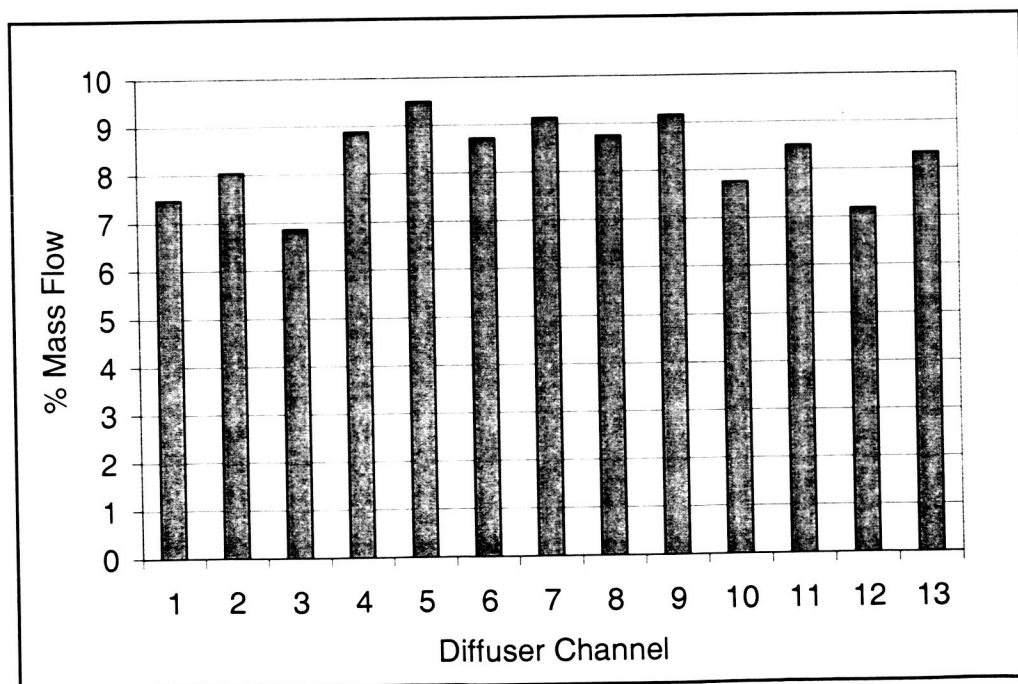
Figure 41. Computed frozen-rotor mass flow distribution for consortium vane-island diffuser at design flow.
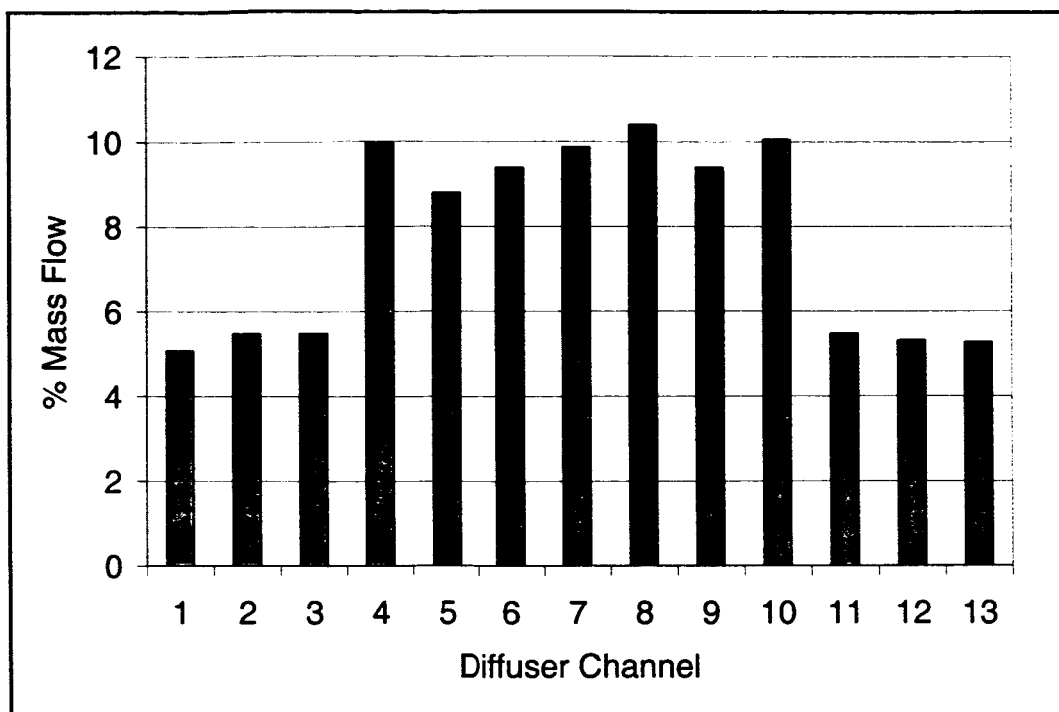
Figure 42. Computed frozen-rotor mass flow distribution for CompV10 diffuser at design flow.
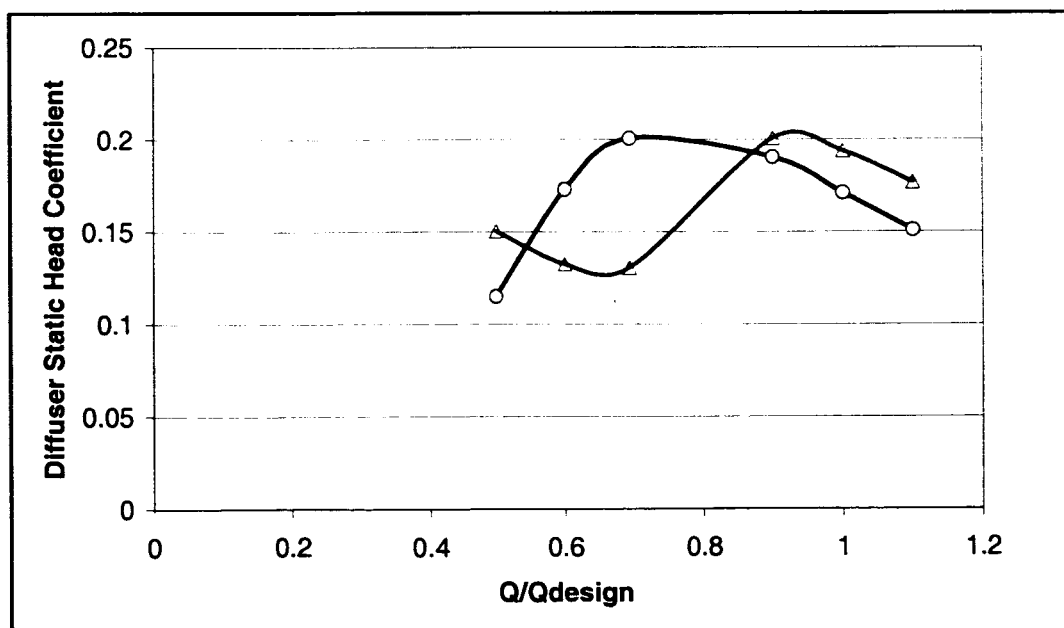
Figure 43. Frozen-rotor calculation for the CompV10 coarse grid model indicates improved operating range (triangles are for the consortium diffuser and circles are for the CompV10 diffuser).
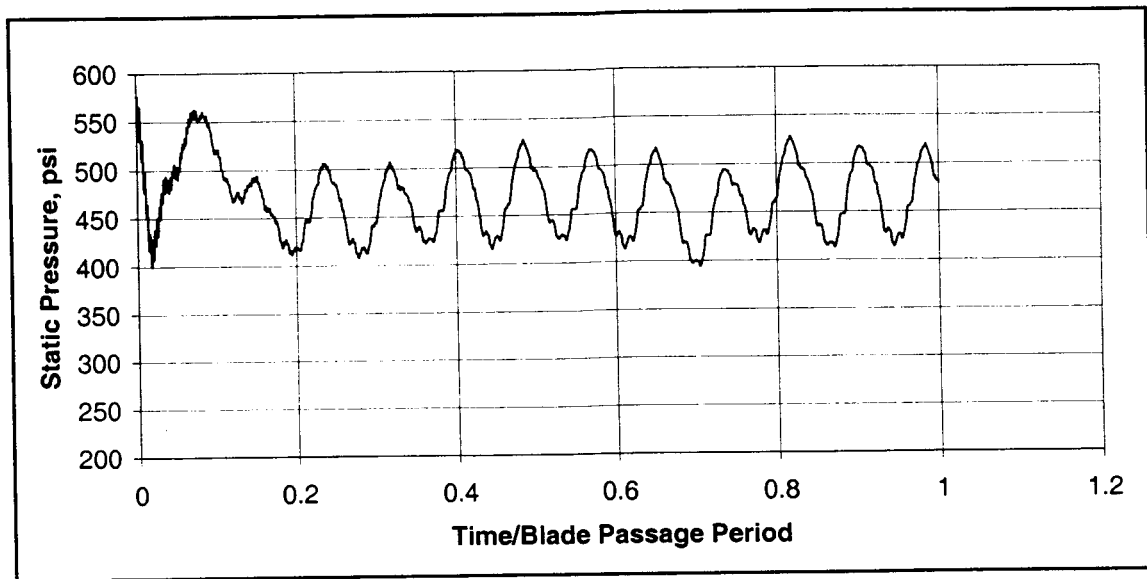
Figure 44. Static pressure time-history for consortium vane-island diffuser at 1210 gpm (37,924 Hz resolution); results reported for a point mid-way between hub and shroud at a radius=4.685" between impeller and diffuser.

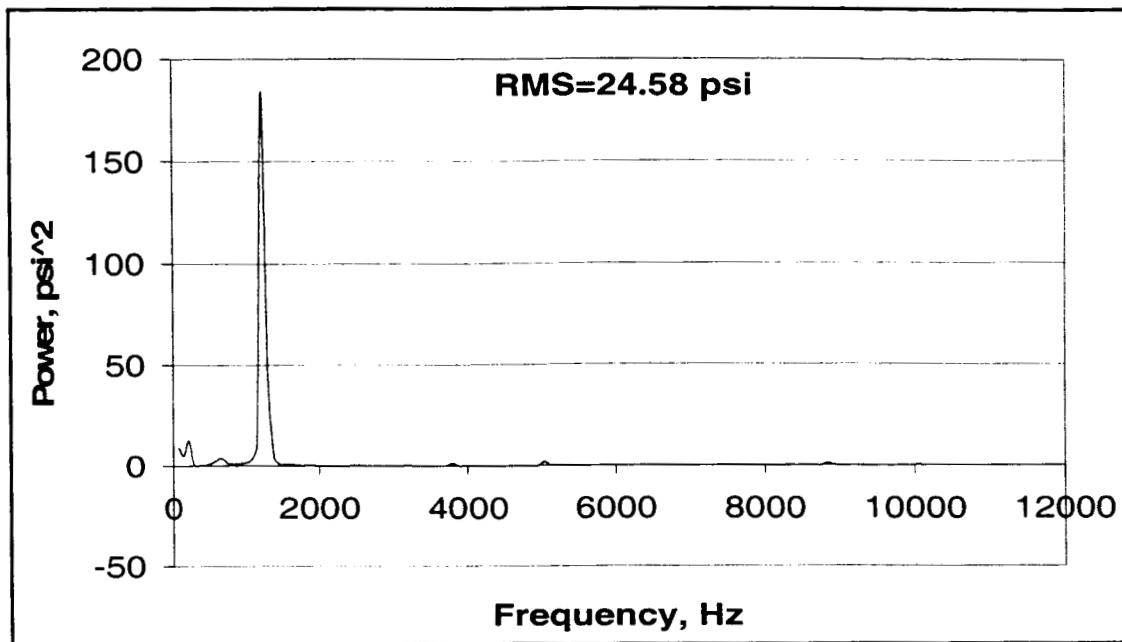Figure 45. Static pressure time-history for CompV10 diffuser at 1210 gpm (37,924 Hz resolution); results reported for a point mid-way between hub and shroud at a radius=4.685" between impeller and diffuser.

131
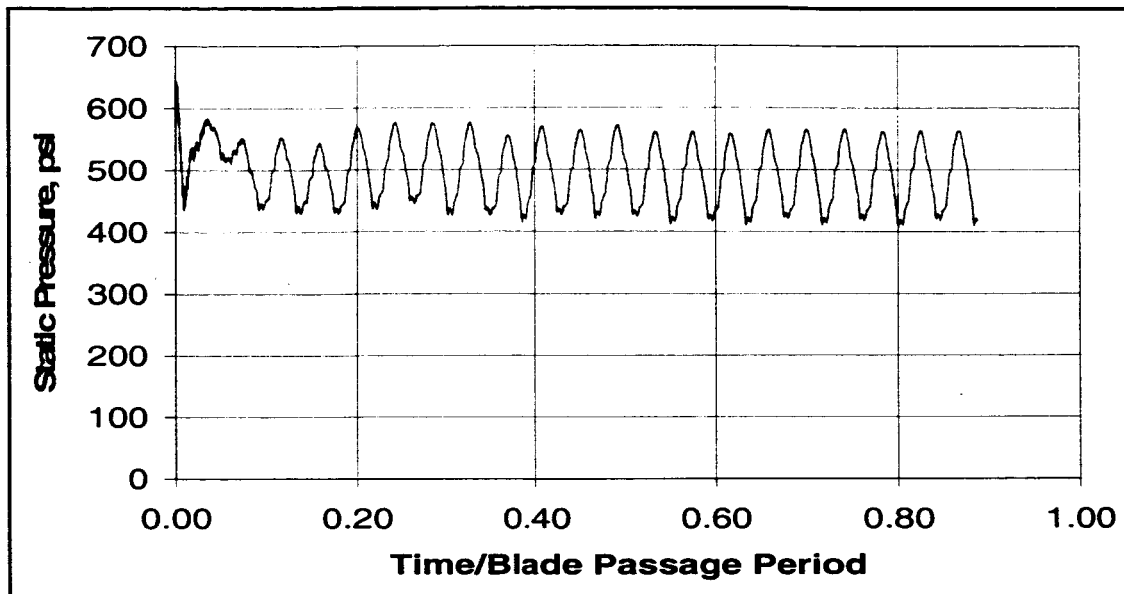
Figure 46. Static pressure time-history for CompV10 diffuser at 839 gpm (37,924 Hz resolution); results reported for a point mid-way between hub and shroud at a radius=4.685" between impeller and diffuser.
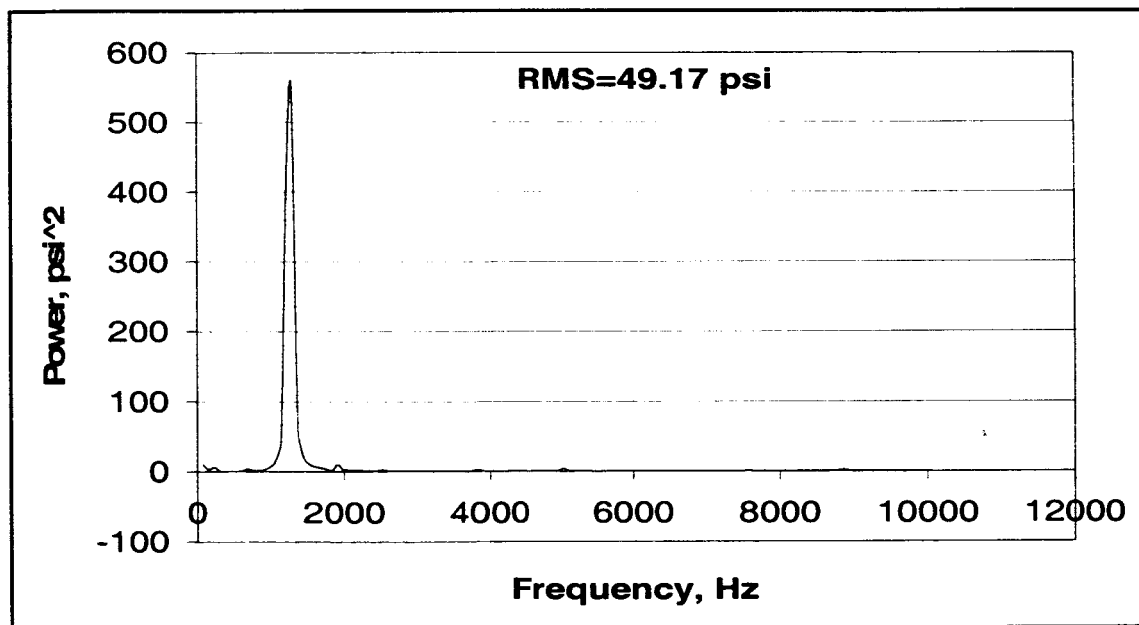
Figure 47. The computed pressure power spectrum for the 839 gpm CompV10 flow case (37,924 Hz resolution); results reported for a point mid-way between hub and shroud at a radius=4.685" between impeller and diffuser.

Figure 48. The computed pressure power spectrum for the 1210 gpm CompV10 flow case (37,924 Hz resolution); results reported for a point mid-way between hub and shroud at a radius=4.685" between impeller and diffuser.

133

Figure 49. Thin vane advanced diffuser concept required modification to B3 of impeller model.
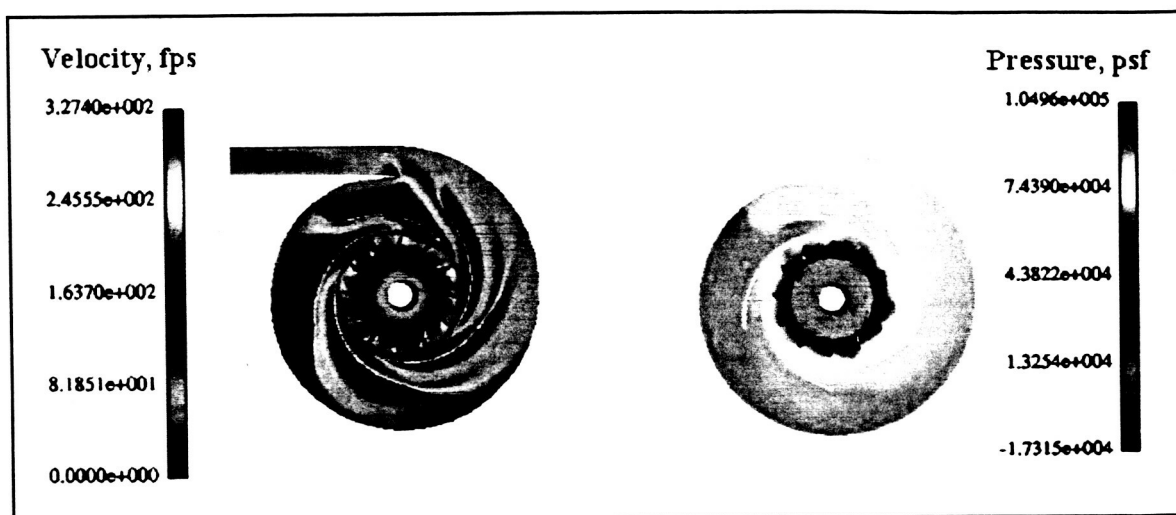
Figure 50. Computed velocity magnitude and static pressure for thin-vane constant thickness diffuser at 1210 gpm.
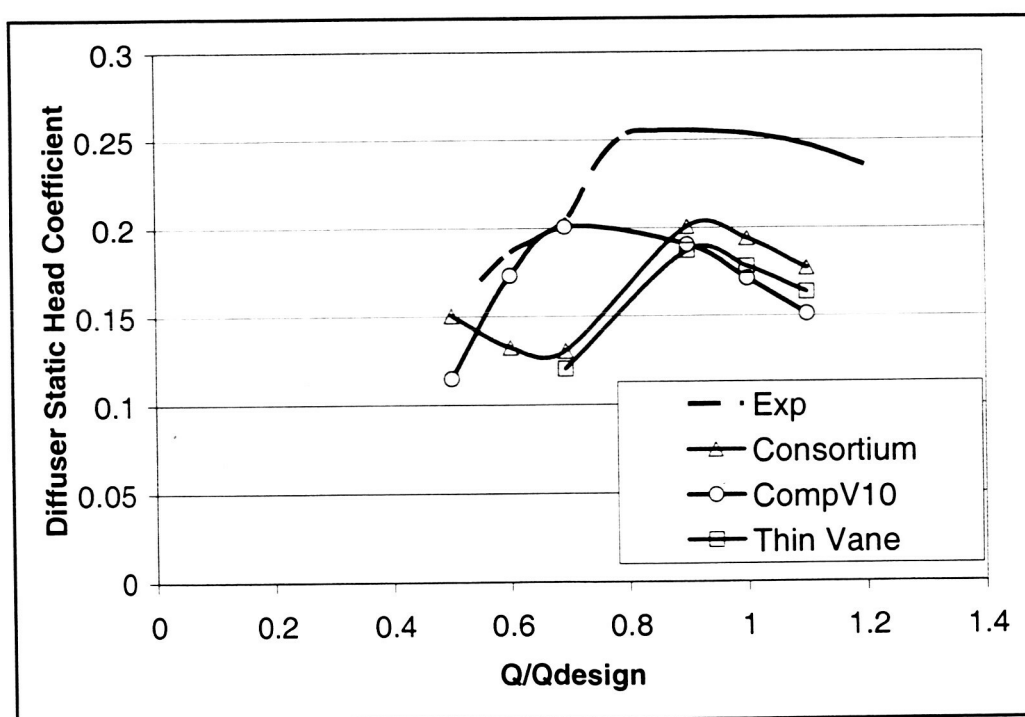

Figure 51. Predicted performance for thin-vane constant thickness diffuser.

TASKS 4B and 5 APPENDIX

ADVANCED DEEP THROTTLING PUMP DIFFUSER CONCEPT DEVELOPMENT

Paper Presented at
JANNAF Conference, Colorado Springs CO, Dec 2003

JANNAF Conference, Colorado Springs CO, Dec 2003

ADVANCED DEEP THROTTLING PUMP DIFFUSER CONCEPT DEVELOPMENT

Adiel Guinzburg, Morgan Williams
The Boeing Company
Canoga Park, CA

adiel.guinzburg@boeing.com
morgan.williams@boeing.com

ABSTRACT

The objective of the turbopump risk reduction program is to enhance and demonstrate critical technologies. While the concept of throttling typically applies to the excursion of the operation and the power level of a rocket engine, this paper is concerned with operation of turbopumps over a wide range of flow conditions. The design of diffusers suitable for wide flow range operation will be discussed. Two wide-flow-range pump diffuser concepts are presented: a constant thickness thin vane diffuser, and a composite vane-island diffuser with multiple throat areas.

INTRODUCTION

The objectives of the Deep Throttling Turbopump program are to increase the throttling range of turbopumps from 30% to 120% of the design value, while maintaining high performance levels. While the concept of throttling typically applies to the excursion of the operation and the power level of a rocket engine, this paper is concerned with the operation of turbopumps over a wide range of flow conditions.

It should be noted that achievement of a large flow range is not dependent on the diffuser alone but also depends on all of the components upstream of the diffuser. The focus of the current effort is on the diffuser, which converts the kinetic energy of the impeller discharge fluid into static pressure. As the stage head coefficient increases,

the diffuser makes a larger contribution. A generic centrifugal pump test configuration is illustrated in Figure 1.
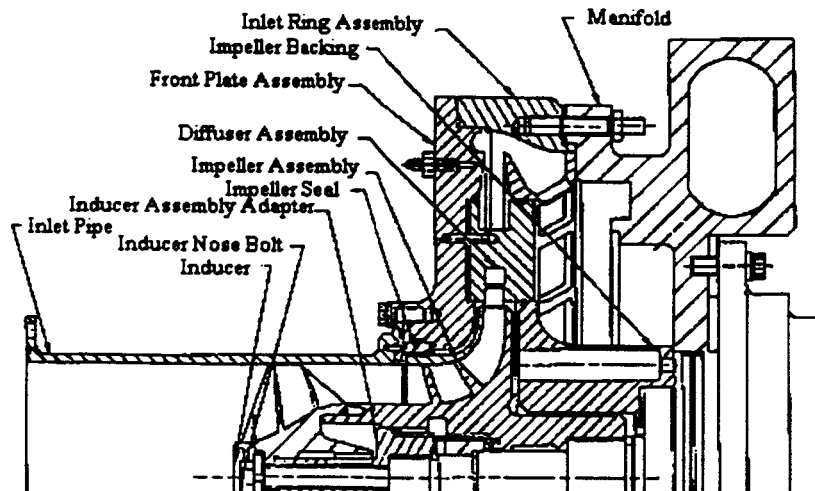

Figure 1. Layout of consortium high-head pump stage.

The pump diffuser is typically designed to optimize the static pressure recovery for a specific operating point, which is determined by the impeller speed and volumetric flow rate. This can be achieved by using a vaneless or vaned diffuser. Compared to the vaned diffuser, the vaneless diffuser requires a larger diameter to accomplish the same amount of diffusion as a vaned diffuser. Since the diffuser weight varies as the cube of its size, the vaned diffuser has a distinct advantage in terms of pressure recovery per pound of weight. A vaned diffuser also provides structural integrity to the pump housing. Hence, the remainder of the paper will focus on vaned diffusers.

For any pump configuration, fluid dynamic stability requires that the head-capacity curve have a negative slope throughout the flow range of interest. To achieve wide-flow range performance, it is required that the diffuser exhibit adequate stall margin and is free of dynamic instabilities such as rotating stall.

Passive methods for controlling stall and increasing the range of stable flow have been proposed by several researchers. For example, Kurokawa et al.[1] and Saha et al.[2] proposed utilizing J grooves aligned with leading edge radial pressure gradients to suppress rotating stall. Active control methods for controlling stall and increasing stable flow range have been proposed by Epstein et al.[3], D'Andrea et al.[4] and Ogut et al.[5] However, active control methods require complicated mechanisms and power input that decreases overall pump efficiency and robustness. Either type of wide-flow range method requires a trade between peak performance and wide-flow range.

In the current paper, two passive wide-flow range vaned diffuser concepts are developed. One is a perturbation of an existing vane island diffuser and the other is a constant thickness thin vane design.

The pump design configuration and diffuser stall is discussed first, followed by the theory behind the two new concepts. Computational fluid dynamics (CFD) will be used as the diffuser design tool. The CFD work is in progress and will be reported in a separate paper[6].

PUMP DESIGN POINT

The pump under consideration is the single stage consortium high head centrifugal pump[7] because water-test data is available for this pump. The pump is designed to raise the inlet pressure by 1180 feet and deliver 1210 GPM of water at 6322 RPM. It should be noted that all blade and flow angles referred to in the remainder of the paper are with respect to a tangential datum.

CONSORTIUM VANE-ISLAND DIFFUSER

The following description of the baseline diffuser is from Ferguson et al.[7] The baseline diffuser (Figure 2) is a vane-island diffuser with 13 vanes formulated to achieve a velocity reduction ratio of 2.2. In the rectangular diffuser throat region, diffusion occurs only in the radial and tangential direction. Downstream of the throat, flow diffuses in the axial direction as well. Downstream of the passage discharge, the axial depth was constant. The baseline diffuser was designed to utilize three-component diffusion in order to achieve an outlet diameter-to-throat area ratio which was within design experience (Reneau et al.[8]). A constant flow area region at the diffuser discharge was used specifically to provide boundary conditions for the purpose of CFD code validation. Table 1 shows the diffuser geometric parameters. The measured diffuser performance is shown in Figure 3.

The head coefficient drops by about 0.05 when the flow goes from 80% to 60% of the design flow. The head coefficient ($\square = \square H/U^2_{tip}/g$) is based on the static pressure rise and the impeller tip velocity, $U_{tip}=249.5$ ft/s. Clearly this diffuser is not suitable for wide-flow range.

Figure 2. Consortium vane-island diffuser with 13 vanes.

Table 1. Consortium vane-island diffuser geometry.

Geometric Parameter	Value
Impeller Tip Diameter	9.045 inches
Impeller B2 Width	0.57 inches
Number of Diffuser Vanes	13
Leading Edge Blade Thickness	0.08
Leading Edge Blade Angle	10 degrees
Diffuser Inner Diameter, D3	9.38 inches
Diffuser Outer Diameter, D4	14.7 inches
Diffuser D3 Depth, B3	0.408
Diffuser D4 Depth, B4	0.6
Diffuser Channel Throat, W1	0.41
Diffuser Channel Length, N	3
Diffuser Channel Throat Area	$0.168\ in^2$
Diffuser Area Ratio	2.47

The vaned diffuser is sensitive to flow incidence angle and leading edge stall is believed to be the cause of loss of diffuser performance and rapid head fall-off at low flow.[9] On a related note, the shape of the baseline diffuser head-capacity curve is very similar to that measured by Kurokawa et al.[1] The dynamic measurements of Kurokawa indicated that the stall exhibited rotating stall characteristics.

The objective of the two new diffuser concepts is to increase the range of the pump, which would result in a slightly steeper curve than that depicted by the baseline head-capacity curve shown in Figure 3.
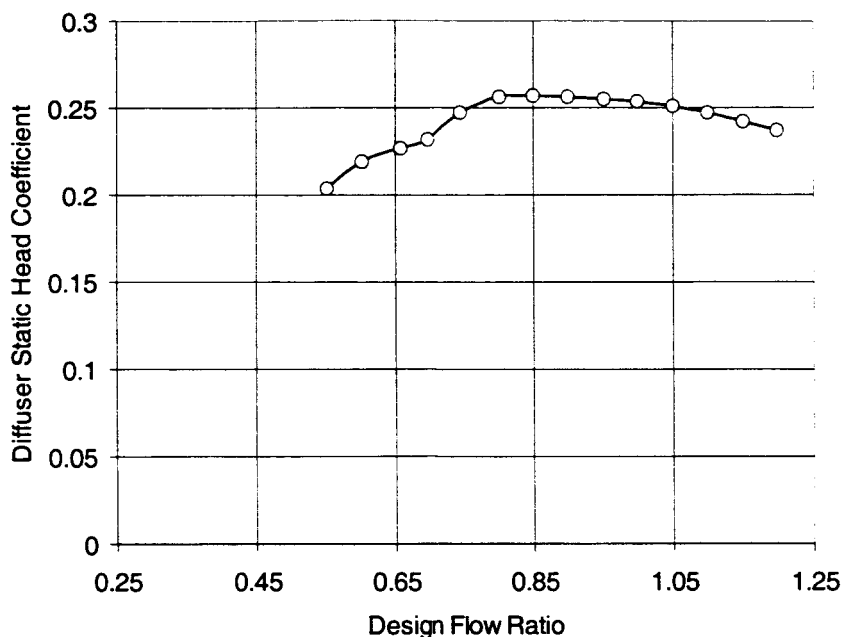

Figure 3. Measured performance for the consortium vane-island diffuser with 13 vanes.

COMPOSITE VANE DIFFUSER

The traditional diffuser design methodology optimizes the diffuser performance at a single flow point – each flow channel has the same blade shape and channel throat area. In principle, the composite vane diffuser achieves wide-flow range by using a summation of channels that are optimized for different flow points. The concept is developed as a perturbation of the baseline vane-island diffuser, i.e., the same number of blades and overall dimensions are retained.

COMPOSITE DIFFUSER THEORY

The typical bladed diffuser has one blade shape repeated N times and is optimized for a single incidence angle. The composite vane diffuser uses a combination of vanes with different leading edge angles.

Figure 4 shows schematically how the traditional vane-island diffuser can be interpreted as a blade row with a given incidence angle and performance. In the case of the consortium vane-island diffuser, the vane blade leading edge angle is 10 degrees and the design flow incidence angle is approximately 1.44 degrees. The measured static head coefficient is 0.25.

Unwrapped to psuedo r-theta plane

Average Inlet Rotational Flow Component

ϕ_{design}

Average Inlet Flow

Inlet flow angle=ϕ_{in}

Traditional Vane-Island or Bladed Diffuser: All blades are designed for one flow

Vane or blade element

Performance @ ϕ_{design}= perf$_0$
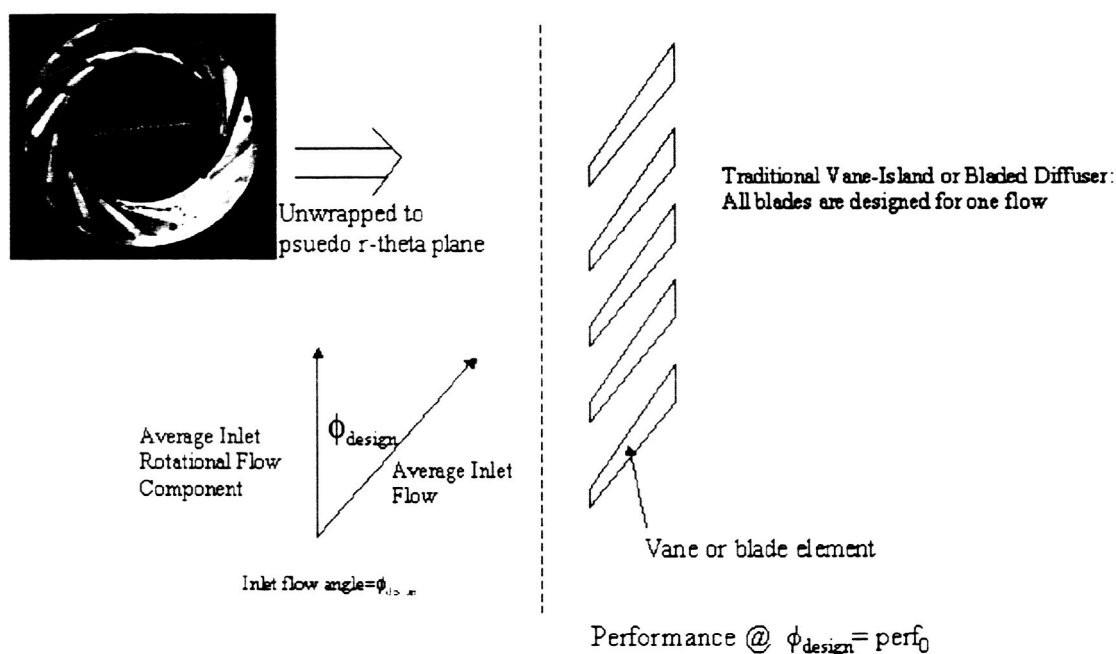
Figure 4. Traditional vaned diffuser constructed with N blades all the same.

Figure 5 shows schematically how the composite vane diffuser achieves wide-flow-range. The performance of the composite vane diffuser is the summation of the performance of each set of individual blade basis elements. Each basis element has a different leading edge blade angle and therefore responds differently to inlet flow.
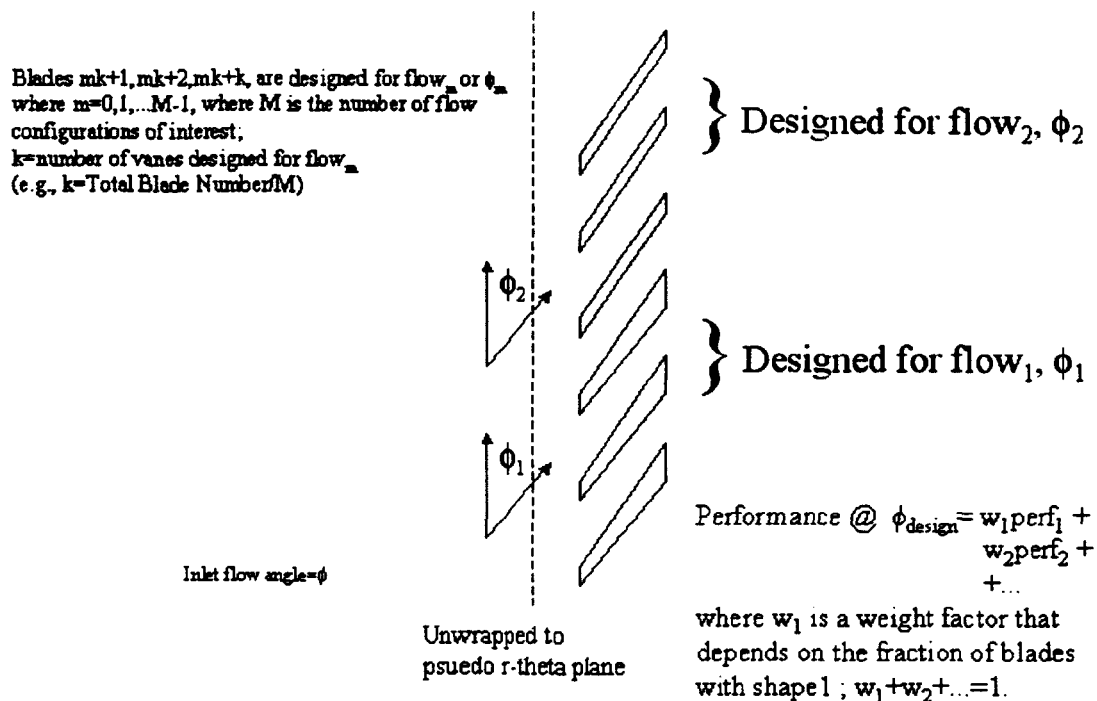
143

Blades mk+1,mk+2,mk+k, are designed for flow_ or φ_
where m=0,1,...M-1, where M is the number of flow
configurations of interest;
k=number of vanes designed for flow_
(e.g., k=Total Blade Number/M)

} Designed for flow$_2$, ϕ_2

} Designed for flow$_1$, ϕ_1

ϕ_2

ϕ_1

Inlet flow angle=φ

Unwrapped to
psuedo r-theta plane

Performance @ ϕ_{design}= w$_1$perf$_1$ +
w$_2$perf$_2$ +
+...

where w$_1$ is a weight factor that
depends on the fraction of blades
with shape 1 ; w$_1$+w$_2$+...=1.

Figure 5. Composite vaned diffuser constructed with different blades geometries.

If $\square_i$ is the performance of a diffuser channel with basis element at a given flow $\square$, then the performance of the composite vane diffuser can be written as:

$$\square\square\square_i\square_i\square\square_\square\square_\square\tilde{\square}$$.!

where $\square_i$ is a weighting factor that depends on the fraction of total blades with basis element and $\square\square_i$=1. To achieve wide flow range, the weighting factors are chosen so that the variation of performance with flow is minimized. The design of the composite vane diffuser will be discussed in the next section.

COMPOSITE DIFFUSER DESIGN AND TRADE STUDY

The importance of the blade leading edge in governing the stall behavior is discussed in Meng and Jackson.[9] The leading edge blade angle and incidence angle will be used to guide the design of each basis element of the composite vane. Existing test data for the consortium vane-island diffuser will be used to construct incidence-versus performance curves for each basis element.

144

Figure 6 shows a leading edge blade angle trade study. The study indicates that the composite vane should use small blade angles to offset the stall observed in the consortium vane-island diffuser data. The composite diffuser basis element is constructed by perturbing the consortium vane-island blade angle. The impact on throat area is shown in Figure 7.

An estimate of the performance of each basis element is needed to optimize the composite diffuser. This estimate is obtained from the existing diffuser head-capacity curve. The curve is first converted to a head-incidence angle curve and then back to a series of head-capacity curves for an array of blade angles. This is shown in Figure 8.
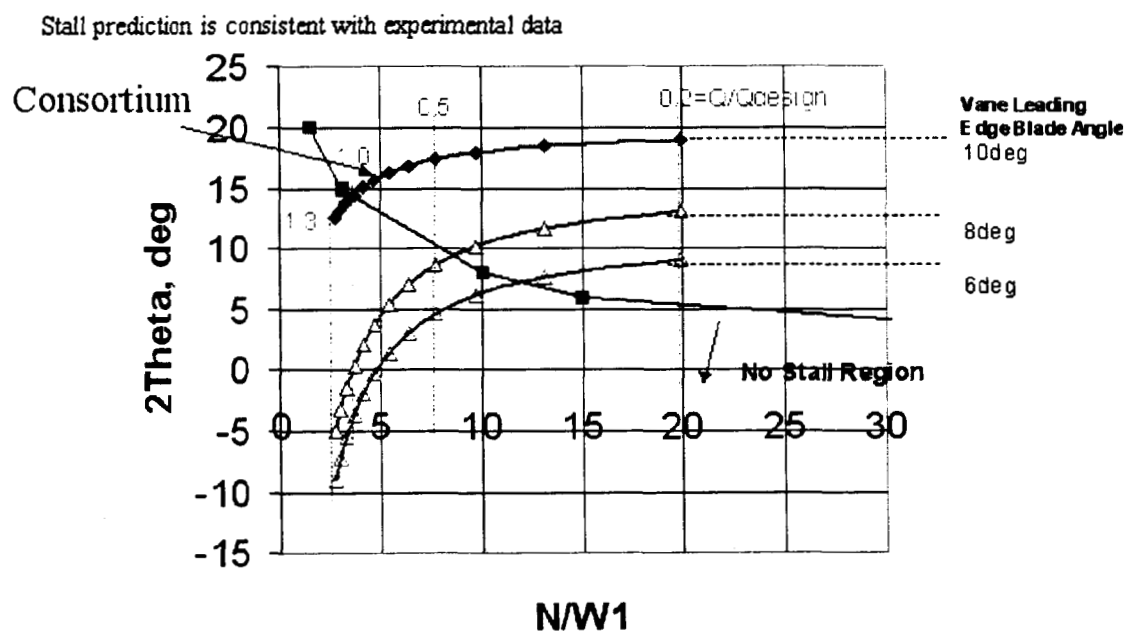
Figure 6. Leading edge blade angle trade-study.
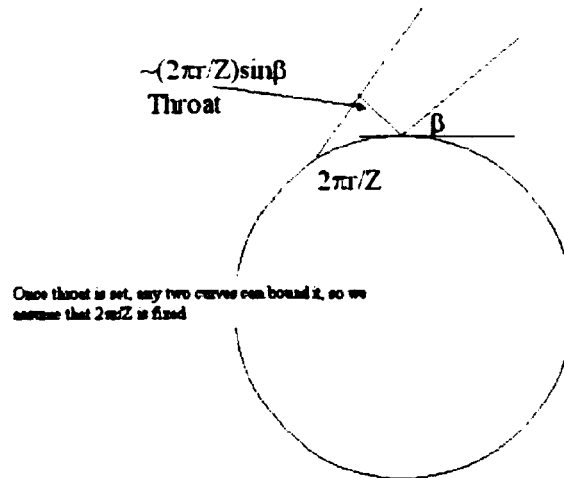
Figure 7. Relationship between diffuser throat and blade angle.
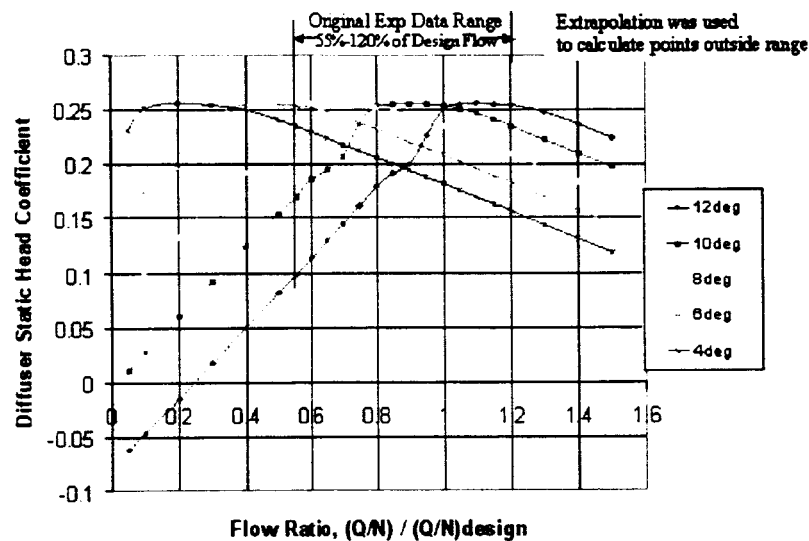
Figure 8. Performance estimate for composite diffuser basis elements.

Equation 1 can now be used to optimize the performance of the composite diffuser. The penalty function can be the head coefficient or the slope of the head-capacity curve or some combination of both. The Solver tool in Microsoft Excel calculates the numerical values of the weights of each basis element to achieve optimal performance. The Solver tool uses a generalized reduced gradient non-linear optimization technique.

146

A trade study and optimization sequence was performed and Figure 9 shows the performance of two different composite vane diffusers optimized to achieve different combinations of maximum average head and minimum head-capacity slope in the range of 30-120% of design flow.
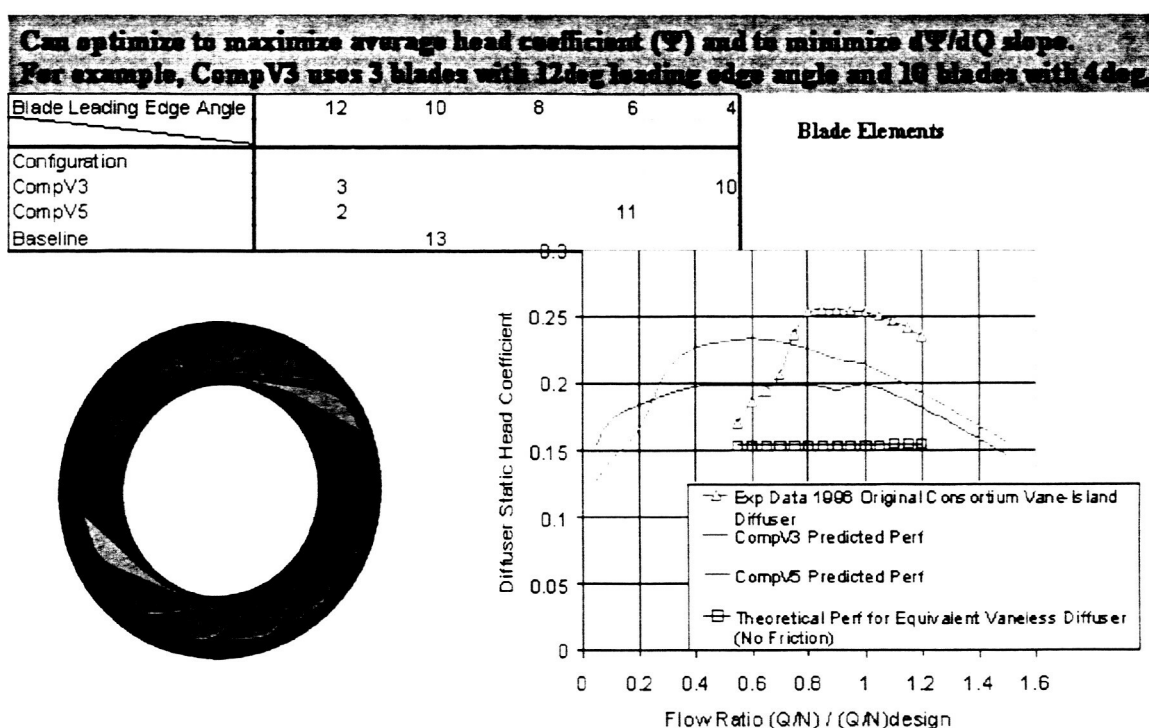

Can optimize to maximize average head coefficient (Ψ) and to minimize dΨ/dQ slope. For example, CompV3 uses 3 blades with 12deg leading edge angle and 10 blades with 4deg.

Blade Leading Edge Angle	12	10	8	6	4	Blade Elements
Configuration						
CompV3	3				10	
CompV5	2		11			
Baseline		13				

Figure 9. Predicted optimized composite vane diffuser performance for 2 different criteria (CompV5 is illustrated on the left).

For example, the CompV5 diffuser for wide-flow range utilizes eleven blades with a leading edge blade angle of 6 degrees and two blades with a leading edge blade angle of 12 degrees.

Figure 9 also shows the CAD model for the CompV5 diffuser. Two blend elements are utilized to transition between the channels with different throat sizes.

Three-dimensional flow computations are planned to confirm the wide flow range performance for the composite diffuser design. Of special concern is the possibility that

the composite vane diffuser may create more dynamic flow activity compared to the traditional vane-island diffuser design.

THIN VANE DIFFUSER CONCEPT

One of the design aspects of this wide flow range diffuser is fewer low-angle diffuser blades that wrap around a lot. In addition, the thin vane diffuser concept achieves wide-flow range by using a judicious radial placement of the diffuser in terms of the Gap A and B discussed below.

The vaned diffuser must accommodate pressure pulsations from the impeller by judicious choice of certain geometric attributes. These are the Gap B, which is the clearance between the impeller blades and the diffuser blades as well as the Gap A, which is the clearance between the impeller shrouds and diffuser shrouds.[10]

Physical reasons for maintaining these gaps are as follows. Gap-A helps to stabilize at low flow by keeping reverse flow from the impeller out from the diffuser. The objective of increasing the range of the pump is therefore achieved and results in a steeper head capacity curve. A small Gap-A on the order of 1% of the impeller radius keeps separated flow from the diffuser from getting into the impeller zones. In addition, maintaining a shroud overlap of about four times the Gap-A ensures that cross-flow interaction does not occur. Thus a good head-capacity curve is maintained.[10]

A large Gap-B helps to avoid axial thrust instabilities by pre-diffusing the impeller discharge flow before it impacts the diffuser vanes. Typically MaKay[10] recommends approximately 6% since a lot of interaction in the form of jets and wakes arise in high-energy pumps. He has also observed less than 4% to be dangerous in high-energy

pumps. Slurry pumps are designed with up to a Gap B of up to 40% of the impeller tip radius to prevent the high-energy impeller fluid flow from wearing out diffuser blades.

To account for boundary-layer blockage effects, twice the boundary layer displacement thickness for zero pressure gradients over the six inches of length (Ls) on the suction side and the sidewalls is applied to the sizing of the diffuser throat area. This gives 22 thousandths of an inch for the proposed thin vane diffuser, which results in a conservative estimate of 9% blockage.

The penalty for an aspect ratio of 1.2 is weighed against the need to have more vanes, which necessitates having a higher blade angle. However, the premise of the design is that a lower blade angle will yield greater wide flow range. Examination of the commonly referred to chart for lines of appreciable stall,[8] it can be seen that increasing the area ratio brings us closer to the demarcation line. The Kline chart[8] also shows that a somewhat larger area ratio is possible if n/w1 is very large. However, this creates a diffuser with a larger discharge diameter. Also, the question arises of the stability of the partly separated flow in the longer wakes. A2/A1 of 1.8 is commonly found in large flow range high-energy multistage diffuser pumps.[12] Such pumps routinely operate over a wide flow range. Instabilities occur above this line, therefore it is preferable to have a smaller ratio for operation off the peak design point. A lower included angle means a more robustness and less sensitivity to incidence angle changes. Since flow range comes from stable flow, the smaller area ratio is preferred. It should be noted that whether A2/A1 of the actual diffuser channel is 1.8 or 2.2 has little influence on overall pressure recovery from the impeller exit to the diffuser exit. This is due to the fact that a large portion of the reduction in (=diffusion of) the absolute velocity head of the fluid

leaving the impeller has already occurred (quite efficiently) by the time this fluid reaches the entry throat of this channel.

Figure 10 shows the layout of the constant thickness thin-vane diffuser design. Three-dimensional flow computations are planned to confirm the wide flow range performance for the constant thickness thin vane diffuser design.
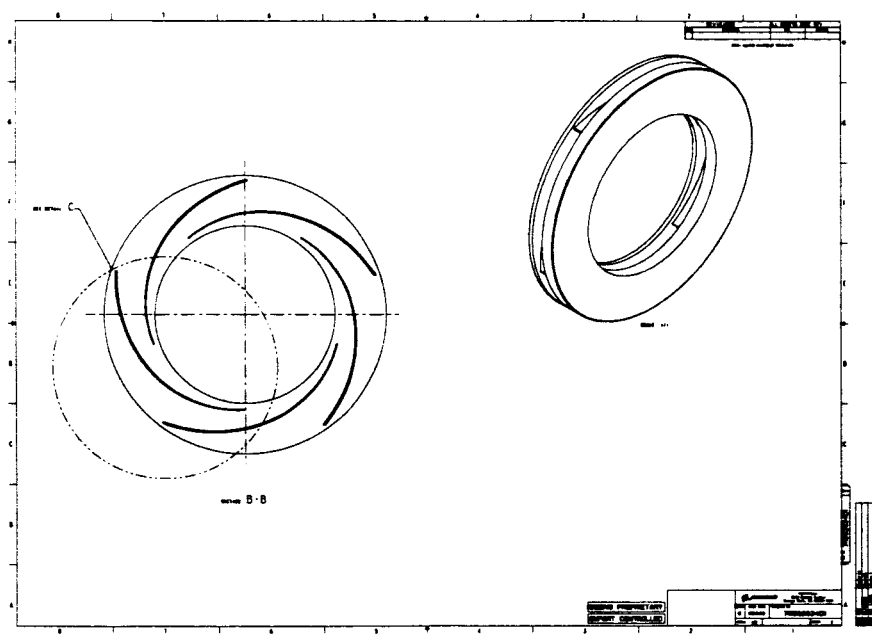

Figure 10. Layout of the constant thickness thin-vane diffuser design.

CONCLUSIONS

The objective of this study was to increase the range of the operation of a pump. The baseline pump was described and presented. In a previous study, it was optimized for a particular design condition. Because of the availability of water test data, this pump was used to provide the upstream components to the new diffuser concepts. Two wide-flow range diffuser concepts have been designed to enhance the operating range. The theory behind these designs has also been presented. Future CFD computations are

planned to confirm the performance of the designs. These computations are in progress and will be reported in a separate paper.

ACKNOWLEDGEMENTS

REFERENCES

1. Kurokawa, J., Saha, S. L., Matsui, J., and Kitahoa, T., "Passive Control of Rotating Stall in a Parallel-Wall Vaneless Diffuser By Radial Grooves," ASME J. Fluids Eng., 122, Mar. 2000, pp. 90-97.

2. Saha, S. L, Kurokawa, J., Matsui, J., Imamura, H. "Passive Control of Rotating Stall in a Parallel-Wall Vaned Diffuser by J-Grooves," ASME J of Fluids Eng., Sep. 2001, Vol. 123, pp. 507-512.

3. Epstein, A. H., Ffowcs Williams, J. E., and Greitzer, E. M., 1986, "Active Suppression of Aerodynamic Instabilities in Turbomachines," J. Prop. & Power, 5, No.2, pp. 204-211.

4. D'Andrea, R., Behnken, R. L., and Murray, M. R., 1997 "Rotating Stall Control of an Axial Flow Compressor Using Pulsed Air Injection," ASME J. Turbomachinery, 119, pp. 742-752

5. Ogut, A., and Garcia, Diego, "Simulation of Flow in Turbopump vaneless and Vaned Diffuser with Fluid Injection," Proceedings of the 7th International Symposium on

Transport Phenomena and Dynamics of Rotating Machinery, Feb., 22-26, 1998, Honolulu, Hawaii, pp. 1470-1481.

6. Williams, M. "Numerical Calculation of Pump Diffuser Flow", paper in preparation, 2003.

7. Ferguson, T. V., Guinzburg, A., McGylnn, R. D., and Brozowski, L. A., "Laser Velocimeter Measurements of the Flow within a Vane-Island Diffuser," Paper FEDSM99-6985, Proceedings of 3rd ASME/JSME Joint Fluids Engineering Conference, July 18-23, 1999, San Francisco, California.

8. Reneau, L. R., Johnston, J. P., and Kline, S. J., 1967, "Performance and Design of Straight, Two-Dimensional Diffusers," ASME J of Basic Eng., pp.141-150.

9. Meng, S. Y. and Jackson, E. D., "The Continuous Diffusion Crossover System Design," Presented at the Symposium on Return Passages of Multi-Stage Turbomachinery, Fluid Machinery Spring Conf, Houston, Texas, June 1983.

10. Makay, Elmer, James A. Barrett., "Changes in Hydraulic Component Geometries Greatly Increased Plant Availability and Reduced Maintenance Cost: Case Histories," Proceeding of First International Pump Symposium.

11. Guelich, J., D. Florjancic and S. E. Pace. "Influence of Flow Between Impeller and Casing on Part-load Performance of Centrifugal Pumps," FED Vol. 81. Pumping machinery 1989, 3rd Joint ASCE/ASME Mechanics Conference, University of CA, San Diego, July 9-12, 1989.

12. Karassik,I.J., Messina, J. P., Cooper, P., Heald, C. C., Pump Handbook

REPORT DOCUMENTATION PAGE

1. REPORT DATE *(DD-MM-YYYY)*	2. REPORT TYPE	3. DATES COVERED *(From - To)*
27-02-2004	Final	Jan 2003 - Feb 2004

4. TITLE AND SUBTITLE

NRA8-21 Cycle 2
RBCC Turbopump Risk Reduction
Final Report

5a. CONTRACT NUMBER

NAS8-01040

5b. GRANT NUMBER

5c. PROGRAM ELEMENT NUMBER

6. AUTHOR(S)

Thomas V. Ferguson, Morgan Williams and Bogdan Marcu

5d. PROJECT NUMBER

5e. TASK NUMBER

5f. WORK UNIT NUMBER

7. PERFORMING ORGANIZATION NAME(S) AND ADDRESS(ES)

The Boeing Co.
Rocketdyne Propulsion & Power
6633 Canoga Ave. PO Box 7922
Canoga Park CA 91309-7922

8. PERFORMING ORGANIZATION REPORT NUMBER

RD04-133

9. SPONSORING/MONITORING AGENCY NAME(S) AND ADDRESS(ES)

NASA - MSFC
Marshall Space Flight Center, AL 35812

10. SPONSORING/MONITOR'S ACRONYM(S)

11. SPONSORING/MONITORING REPORT NUMBER

12. DISTRIBUTION/AVAILABILITY STATEMENT

13. SUPPLEMENTARY NOTES

14. ABSTRACT

This project was composed of three sub-tasks. The objective of the first task was to use the CFD code INS3D to generate both on- and off-design predictions for the consortium optimized impeller flowfield. The results of the flow simulations are given in the first section. The objective of the second task was to construct a turbomachinery testing database comprised of measurements made on several different impellers, an inducer and a diffuser. The data was in the form of static pressure measurements as well as laser velocimeter measurements of velocities and flow angles within the stated components. Several databases with this information were created for these components. The third subtask objective was two-fold: first, to validate the Enigma CFD code for pump diffuser analysis, and secondly, to perform steady and unsteady analyses on some wide flow range diffuser concepts using Enigma. The code was validated using the consortium optimized impeller database and then applied to two different concepts for wide flow diffusers.

15. SUBJECT TERMS

turbopump; CFD; testing; database; Enigma; Phantom; INS3D; laser velocimeter; pressure; impeller; inducer; vane-island diffuser

16. SECURITY CLASSIFICATION OF:			17. LIMITATION OF ABSTRACT	18. NUMBER OF PAGES	19b. NAME OF RESPONSIBLE PERSON
a. REPORT	b. ABSTRACT	c. THIS PAGE			Thomas V. Ferguson
u	u	u	uu	152	**19b. TELEPHONE NUMBER** *(Include area code)* (818) 586-0354